An Assessment of the SRTM Topographic Products

E. Rodríguez*, C.S. Morris, J.E. Belz, E.C. Chapin,
J.M. Martin, W. Daffer, S. Hensley

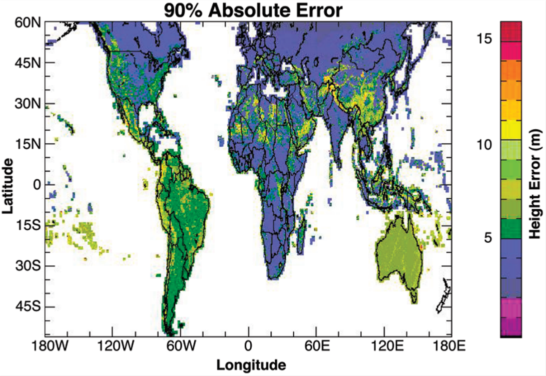

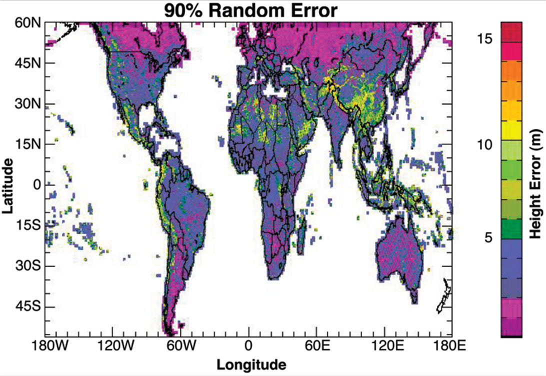

Jet Propulsion Laboratory D-31639

*ernesto.rodriguez@jpl.nasa.gov

Contents

List of Figures

List of Tables

Summary

The NASA/NIMA (now NGA) Shuttle Radar Topography Mission (SRTM) collected interferometric radar data which has been used by JPL to generate a near-global topography data product for latitudes smaller than 60°. As part of the SRTM mission, an extensive global ground campaign was conducted by NIMA/NGA and NASA to collect ground-truth which would allow for the global validation of this unique data set. This report presents a detailed description of how the results in this table were obtained. It also presents detailed characterization of the different components of the error, their magnitudes, and spatial structure.

The performance requirements for the SRTM data products are:

1. The linear vertical absolute height error shall be less than 16 m for 90% of the data.
2. The linear vertical relative height error shall be less than 10 m for 90% of the data.
3. The circular absolute geolocation error shall be less than 20 m for 90% of the data.
4. The circular relative geolocation error shall be less than 15 m for 90% of the data.

The table shown below summarizes the SRTM performance observed by comparing against the available ground-truth. All quantities represent 90% errors in meters. It is clear from this table that SRTM met and exceeded its performance requirements.

	Africa	Australia	Eurasia	Islands	N. America	S. America
Absolute Geolocation Error	11.9	7.2	8.8	9.0	12.6	9.0
Absolute Height Error	5.6	6.0	6.2	8.0	9.0	6.2
Relative Height Error	9.8	4.7	8.7	6.2	7.0	5.5
Long Wavelength Height Error	3.1	6.0	2.6	3.7	4.0	4.9

We have found that the SRTM error could be divided into very long wavelength (continental scale or larger) errors and short wavelength random errors. To show the relative magnitude of the two contributions, the table also lists the magnitude of the long wavelength error (which contributes to the absolute vertical accuracy).

The ground truth data collected were not appropriate for validating *relative* geolocation errors. It is expected that the main sources of geolocation errors are also long wavelength, so that the *relative* geolocation error will in general be smaller than the *absolute* geolocation error, since common errors will cancel. The absolute geolocation performance is better than that required for the relative geolocation, which provides indirect evidence that the relative geolocation requirement was also met.

Chapter 1

Overview

The Shuttle Radar Topography Mission (SRTM) [1] was a collaboration between the National Aeronautics and Space Administration (NASA) and the National Imagery and Mapping Agency (NIMA). [NIMA changed its name in November 2003 to the National Geospatial-Intelligence Agency (NGA).] SRTM collected interferometric radar data which has been used by the Jet Propulsion Laboratory (JPL) to generate a near-global topography data product for latitudes smaller than 60°. As part of the SRTM mission, an extensive ground campaign was conducted by NIMA and NASA to collect ground-truth which would allow for the global validation of this unique data set.

The purpose of this report is to document the analysis that was undertaken to verify the SRTM performance and to show how the mission requirements were met and exceeded. Table 1.3 presents a summary of the SRTM performance for each mapped continent. This performance exceeded the required performance by almost a factor of 2. Other assessments of the SRTM performance have examined the spatial resolution of SRTM [2], or compared its performance against lidar for vegetated regions [3]. Unlike those studies, we will endeavor to characterize all components of the SRTM errors on a global basis.

In this chapter, we review the SRTM measurement requirements, review the ground-truth data used for the instrument verification, and summarize the characteristics of the residual errors. The remaining chapters of this report present the details showing how summary numbers were derived. Chapter 2 shows in detail all comparisons made to verify that SRTM was meeting the most fundamental requirement on height accuracy. Chapter 3 studies in greater detail the different spatial components in the residual SRTM errors, and looks in some detail at the long wavelength errors. Chapter 4 concentrates on the high-frequency error components and validates the Terrain Height Error Data (THED) product put out by SRTM. This chapter also presents the random and absolute errors included as part of the SRTM height data headers. Chapter 5 details the methodology used to calibrate the system timing and geolocation and verifies the geolocation accuracy using radar identifiable kinematic GPS transects. Finally, Chapter 6 presents a detailed comparison of the SRTM DEM against a high resolution and accuracy DEM obtained by the GeoSAR interferometer, allowing a cross-comparison of interferometric data sets.

1.1 SRTM Performance Requirements

The performance requirements for the SRTM data products are:

1. The linear vertical absolute height error shall be less than 16 m for 90% of the data.
2. The linear vertical relative height error shall be less than 10 m for 90% of the data.
3. The circular absolute geolocation error shall be less than 20 m for 90% of the data.
4. The circular relative geolocation error shall be less than 15 m for 90% of the data.

1.2 Verification Data Sets

The global verification of the SRTM product presents a unique challenge since the instrument accuracy was expected to be better than the accuracy of most topographic data sets which were globally available. In order to solve this problem, an extensive ground-truth data set was collected, with the understanding that the quality of the globally available ground truth might not be sufficient for a complete verification of the SRTM data.

1.2.1 Kinematic GPS Transects

The most extensive ground-truth effort was made in collecting a globally distributed set of ground control points (GCPs) using kinematic Global Positioning System (KGPS) transects. The distribution of the data is shown in detail in Section 3.1. A typical KGPS transect spanned a substantial part of a continent, thus allowing for the characterization of errors at all length scales.

The KGPS data were collected by driving vehicles carrying Global Positioning System (GPS) receivers along roads throughout the mapped areas, thereby producing a set of data representing a non-uniform sampling of the latitude, longitude and height along the surface feature. Most of the data were collected by NIMA or cooperating agencies within the country in question. Data in Argentina and Paraguay were collected by JPL personnel. Much of the GPS data were processed by NIMA personel using the JPL GIPSY software (http://gipsy.jpl.nasa.gov). The remaining datasets were processed under a NIMA contract by JPL and TRW, using the same GIPSY software under the supervision of Dr. Frank Webb. The total data collection yielded nearly 9.4 million samples covering six continents with a general accuracy of ~ 50 cm (1σ).

Regions with significant discrepancy between ground-truth and the SRTM heights (near overpasses and bridges, for instance–see Figure 1.1, or in very forested regions) were eliminated during a visual Q/A process. GPS data with a standard deviation of more than 1 meter within a 30 m pixel, or more than 5 meters over a 3 by 3 pixel box (90 m × 90 m) were removed. Furthermore, data within 3 pixels of a void posting were removed, since these areas were usually associated with SRTM unwrapping anomalies.

Multiple GPS samples within a single SRTM 30 m data pixel were averaged so that each SRTM pixel was equally weighted. Additional cuts for the image analysis (see Section 5.2) yielded over 2 million ground truth points. The distribution of kinematic GPS GCPs and image ground-truth points for each continent is shown in Table 1.1.

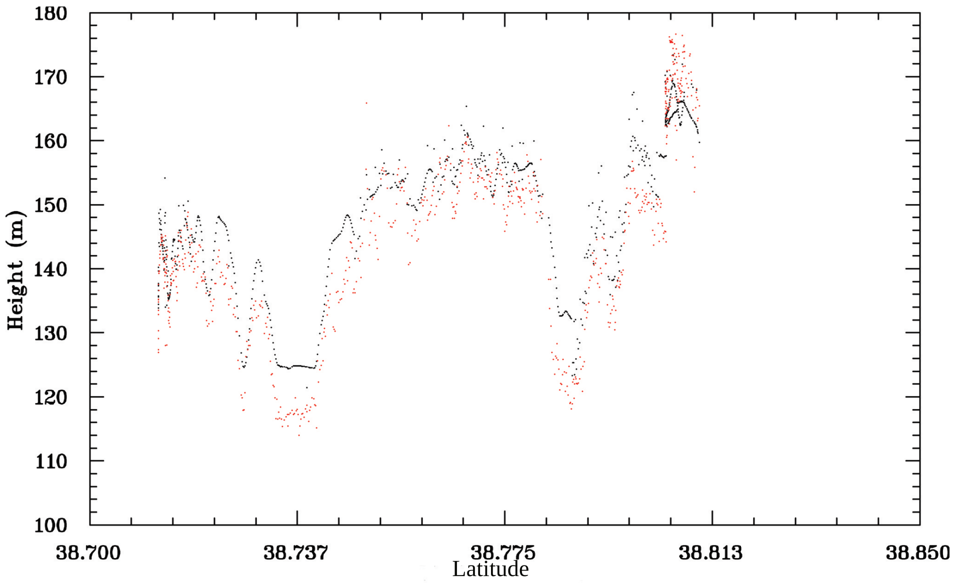

Figure 1.1: Scatter plot of kinematic GPS height measurements (black) and interpolated SRTM height values (red) near St. Louis, MO, versus longitude. Data from several bridges crossing the Mississippi River are clearly evident, and were removed from the set of ground truth points.

"Continent"	No. of Kinematic GPS Tracks	No. of Cells With Data	No. of GPS Samples ×1000	No. of Truth Points ×1000
N. America	6	178	1750	402
S. America	5	196	1005	328
Africa	4	143	2439	395
Eurasia	11	192	2622	445
Australia	4	140	1145	381
New Zealand	2	31	393	64

Table 1.1: Ground Truth Data Summary

1.2.2 DTED Level 2 Cells

As part of its Digital Terrain Elevation Data (DTED) Level 2 generation, NIMA produced a set of 42 one-degree cells whose accuracy was expected to be similar to, or better than the SRTM data, while its spatial resolution was similar to SRTM. The geographical distribution of DTED 2 cells is presented in Table 1.2. The exact locations of the DTED data are given in Section 2.2.

Continent	Number
Africa	5
Australia	0
Eurasia	26
Islands	0
N. America	6
S. America	5

Table 1.2: Summary of the geographic distribution of DTED 2 patches.

1.2.3 Height Patches

In addition to the high-quality DTED 2 cells, NIMA generated a set of 142 height“chips”.[141 patches were used in our analyses.] The process used to generate these chips (or patches) was similar to the one used to generate DTED 2 data, but the final data sets did not go through the same rigorous quality assessment and editing. The distribution of these patches was selected to be as random as possible, while concentrating on regions of some, but not extreme, relief.

1.2.4 Ocean GCPs

The ocean surface topography, which is a combination of the geoid, the ocean circulation, and tidal changes is very well known. In the deep ocean, altimeters have determined the ocean surface to centimetric levels and tidal and geoid models (e.g., EGM96) are accurate to similar accuracy. In coastal regions, both tidal and geoid models are less precise; nevertheless, the error in the topography is much smaller than 50 cm, which is more than sufficient to gauge the SRTM accuracy and provide GCPs for calibration purposes. For the SRTM mission, the EGM96, the TOPEX mean sea surface, together with a tidal model tuned for coastal accuracy [4], were used to generate ocean ground-truth surfaces. These GCPs are used for calibration, mosaic formation, and assessment of the residual errors. GCPs were generated with a separation of 10 km for all the SRTM ocean data, which extended for at least 90 km from the coast.

1.2.5 GeoSAR DEM Data

An X-band interferometer DEM generated by the GeoSAR instrument was obtained by mosaicking 6 GeoSAR data takes over Santa Barbara County, California. The DEM derived from each pass of GeoSAR data has a specified 1 sigma relative height accuracy of 1 m and an absolute height accuracy of 2.5 m averaged over the 10 km swath with 5 m postings. Since the DEM used for the comparison is a synthesis of multiple passes, the DEM is significantly more accurate than this in the areas covered by more than 1 data take. In addition, the statistical uncertainties have been reduced by averaging the GeoSAR data when the posting was increased from 5 m to 30 m for comparison with the SRTM data.

1.2.6 Other Ground Control Points

In addition to previous data sets, NIMA provided approximately 70,000 GCPs which had been obtained using various techniques over the years. Over 10,000 GCPs were obtained from the JPL automated GPS processing database were also added to the GCP database. Finally, over 6,000 GCPs were derived from the GPS transcets (section 1.2.1). The total number of GCPs available was 86,774.

This GCP dataset was used by the Ground Data Processing System as a quality assurance check during operational processing. In addition, a small subset of these GCPs, with a minimum of 0.1 degrees of latitude/longitude separation between GCPs, were used by the mosaic subsystem.

However, use of this GCP database for verification was problematic. The distribution of GCPs was non-random with the majority of GCPs densely packed in a small number of geographic areas. And while the majority of GCPs were in reasonable agreement with SRTM and other DEM sources, there was a small, but significant percentage of GCPs that were obviously in error by many tens of meters - over 100 meters in some cases. Unfortunately, there was no useful error assessment on individual GCPs. Given this lack of reliability and the vast quantity of other verification datasets, the analysis presented below does not dwell in great detail on the differences between this data set and the SRTM data set. It is sufficient to note that the inclusion of this relatively small data set does not significantly change the statistical results, while significantly increasing the number of outlier comparisons.

Figure 1.4 shows an example of ground control points from all the sources listed above for Eurasia.

1.3 SRTM Error Sources

The error characteristics for Interferometric SAR's are well understood and have been summarized in the open literature in [5] [6]. Rosen et al. [6] also review interferometric SAR up to the year 2000, and the reader is referred there for greater detail on the technique. In Appendix A, we give a detailed description of all the error sources which were present for the SRTM mission.

1.3.1 Errors After Static and Dynamic Calibration

Interferometric errors can be divided into static and time-varying errors. Static errors are those which can be regarded as having been constant over the data collection. Since these errors are constant, they can be calibrated by means of natural or man-made targets with know position and height. Time varying errors are due to motion of the interferometric mast and changes in the beam steering. These errors can be partially compensated by dynamic calibration and mosaicking.

We list below the main contributors to the static and dynamic errors, the calibration method used to estimate them, and the magnitude of the residual error after calibration.

Baseline Roll Errors: An error in knowledge of the baseline roll angle will induce a cross-track slope error in the estimated topography whose magnitude is equal to the roll error. The SRTM instrument used a sophisticated metrology system (AODA) coupled with post-flight filtering and estimation of the baseline position. The main components of the baseline motion are due to the natural modes of oscillation of the mast. These motions can be modeled and removed so that they do not constitute a dominant error source. In addition, the baseline position is affected by the Shuttle's attitude maneuvers. The time scale for residual roll errors is long, resulting in spatial errors with wavelength on the order of thousands of kilometers. They constitute the primary source for long-wavelength residual errors. Figure 1.2 shows a representative example of this residual long-wavelength error estimated by subtracting the sea surface topography, which is know to centimetric accuracy from the SRTM estimated topography. The peak values of this residual error are $\sim \pm 10$ m.

Phase Errors: These errors are due to two sources: thermal or differential speckle noise and systematic phase changes due to antenna pattern mismatches or long term drift of the instrument electronics. The noise contamination result in height errors which are random and which exhibit short spatial correlation lengths. These errors cannot be compensated during ground processing.

The antenna patterns for each of the channels do not have identical far-field phase characteristics. If uncompensated, this phase mismatch causes results in a net systematic phase error (called the phase screen) which is a function of the look angle. Due to the stability of the antenna far-field phase, this phase screen can be estimated by binning the height errors over the ocean as a function of look angle and applying the mean phase bias as a function of angle as a phase correction to the interferogram.

To estimate this phase screen, SRTM collected data prior and after each continental crossing, as well as for a small number of basin-wide ocean data takes. Estimates of the phase screen were obtained as a function of time and for each of the four SRTM elevation beams and all beam positions. The phase screen correction was not observed to change significantly over the mission lifetime: the estimated changes in the height error correction were estimated to be below 10 cm.

Finally, a slow drift of the differential phase was observed over the lifetime of the mission (see Figure 1.3), probably due to slow changes in instrument temperature. The residual phase errors induce cross-track tilts which are practically indistinguishable from the residual roll errors discussed above.

Beam Differential Errors: Systematic phase differences between the SRTM beams induce height differences at the beam overlaps. These difference can be time-varying since the beam steering angles are changed according to the topography to preserve the swath. This dynamic effect is corrected during ground processing by using the beam overlap height differences to estimate beam phase offsets. Since the instrument was designed so that all beams overlapped continuously, a time varying along-track phase calibration could be estimated and applied to the data. This ensured that all beams had a consistent phase error. The residual error due to this phase mismatch was negligible (below 10 cm) after along-track calibration.

Timing and Position Errors: These are induced by uncompensated delays in the system or errors in the estimated baseline position and result in geolocation errors. These errors are calibrated by using targets whose position was known and which could be identified in the radar image or topography, such as corner reflectors or kinematic GPS transects. The calibration procedure is as discussed in in great detail in Section 5.1. The residual geolocation errors are discussed in Section 5.2.

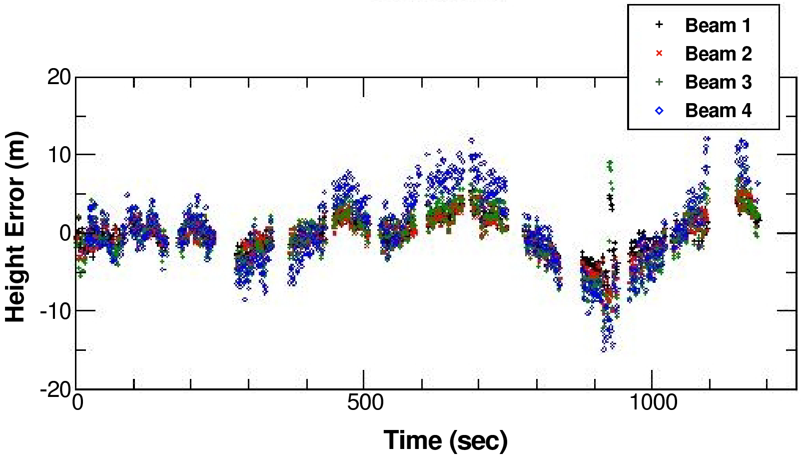

Figure 1.2: Post-calibration height error residuals for a long ocean data take. The values shown are cross-track averages for each of the four SRTM beams. The time scale shown corresponds to a spatial scale of approximately 9000 km

1.3.2 Reduction of Static and Dynamic Errors

The residual errors described in Section 1.3.1 can be compensated in three ways:

Along-Track Calibration: Estimate the beam to beam height discontinuities, as described above.

Dynamic Calibration: Use the know ocean topography (including tidal effects) to estimate static phase screens and time changing residual phase and roll errors and to generate ocean ground control points.

Mosaic: Use the calibration data, together with other GCPs (including a subset of the kinematic GPS GCPs), and pass-to-pass tie-points, to perform a continent scale weighted least squares adjustment to reduce residual height errors. The mosaic correction estimates system phase (or, equivalently, roll) errors, and corrects the data in height and position given the estimated phase errors. The adjustment implies that residual errors will have some correlation over long scales. Due to the lack of an extensive GCP data base in continent interiors, the errors are best constrained at the oceans and less constrained in the interiors.

As an example of the mosaic/calibration error reduction, Figure 1.4 shows the errors after static calibration, but prior to least-squares adjustments. The dominant errors are swath to swath differences, as is evident from the obvious swath patterns in the data. Figure 1.5 shows the residual errors after adjustments. This figure shows that most swath discontinuities have disappeared, and

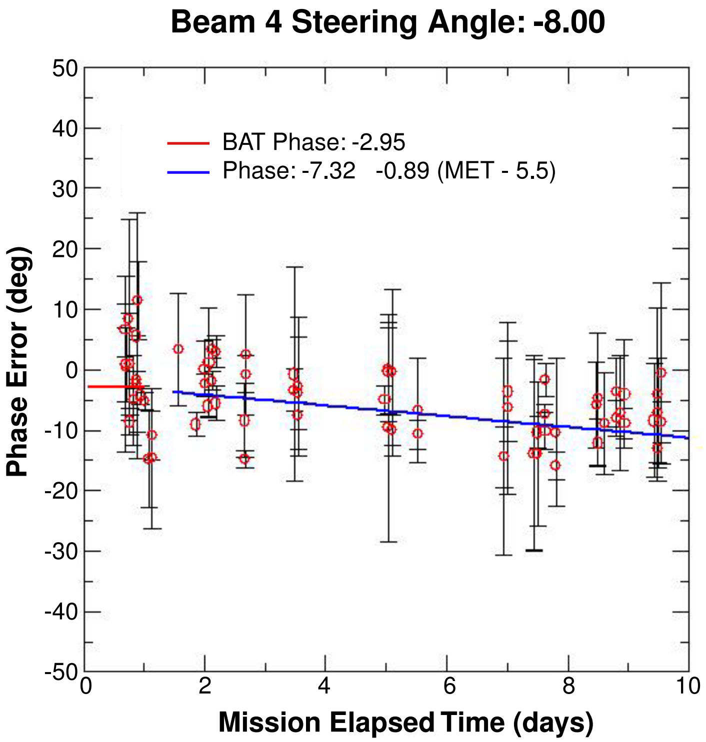

Figure 1.3: Long term drift of the SRTM phase for beam 4, estimated using ocean crossings over the lifetime of the mission. Other beams show similar trends. The induced height errors are on the order of 5 m–10 m.

the overall error variance has been reduced. Small residual long wavelength errors remain, as can be seen in Mongolia and Afghanistan.

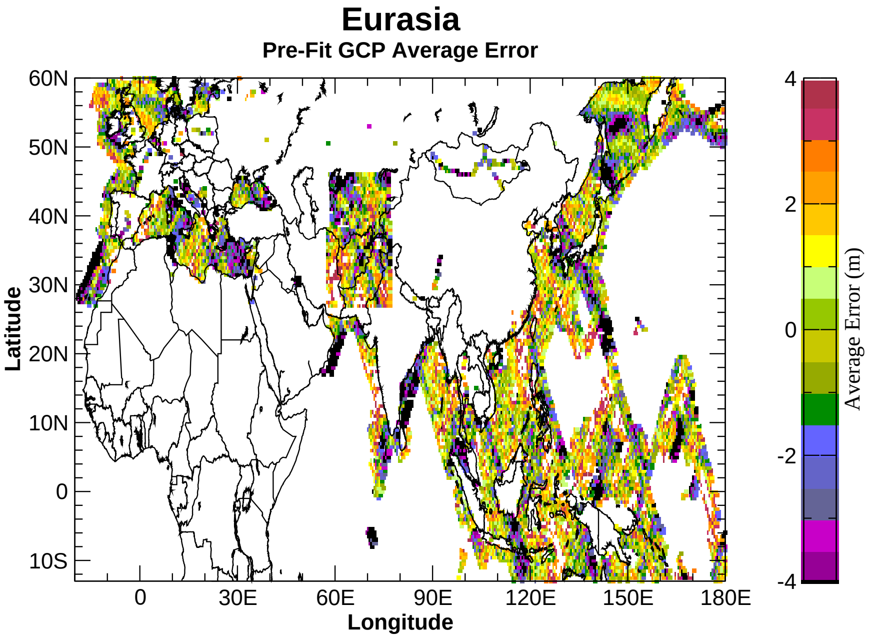

Figure 1.4: Height errors for ocean and land GCPs, prior to along-track and dynamic calibration and mosaic least-squares adjustments.

1.4 Summary of SRTM Residual Error Characteristics

The detailed nature of the SRTM residual errors is presented in the subsequent chapters. In the remainder of this chapter we summarize the spatial characteristics and magnitude of the errors and present a mathematical model for the SRTM errors which has been used as an aid in populating the systematic error fields in the SRTM product headers.

It is useful to introduce the “structure function” as a tool for examining the spatial dependence of the data. This function is defined as

$$D(\Delta) = \left\langle (\delta h(x) - \delta h(x + \Delta))^2 \right\rangle \tag{1.1}$$

where $\delta h(x)$ is the height error as a function of position, Δ is the spatial separation, and angular brackets denote ensemble averaging.

For homogeneous statistical processes, it can be shown that the structure function can be related to the height error correlation function by

$$C(\Delta) = 1 - \frac{D(\Delta)}{2\sigma^2} \tag{1.2}$$

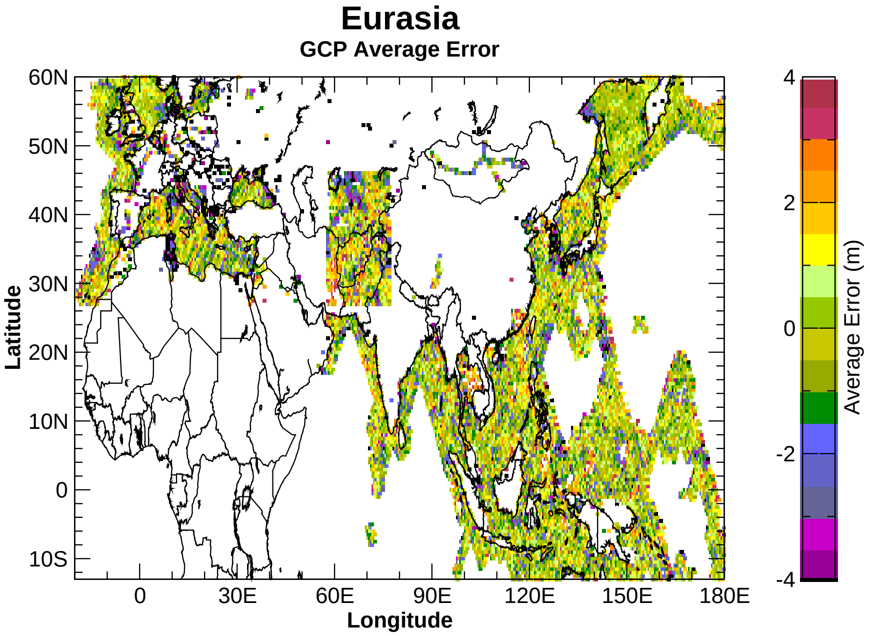

Figure 1.5: Height errors for ocean and land GCPs, after along-track and dynamic calibration and mosaic least-squares adjustments.

where σ is the standard deviation of the process (which is constant in space).

Given these preliminaries, the following list summarizes the results of the ground truth studies:

a- The SRTM error meets and exceeds the performance requirements given in Section 1.1. Conformance to the absolute height requirements is presented in Chapter 2. Relative error requirement conformance is presented in Chapter 4. Finally, Chapter 5 shows how the absolute planimetric requirement was met.

b- The correlation functions drops quickly for separations up to about 300m-400m. (Alternately, the structure function increases quickly from zero for these separations). This implies that the SRTM error has a component which decorrelates quickly. However, this component does not account for the entire error since the structure function continues to increase for larger separations. Section 3.3 presents a detailed discussion and results.

c- For larger separations, the structure function does always approach an asymptotic value, and its behavior varies with geographic location. This indicates that for large scales the process is not always homogeneous or stationary. Section 3.3 presents the behavior of the structure function for each continent.

d- After removing long wavelength biases, the residual error standard deviation can be shown to be nearly linearly dependent on the (uncorrected) Terrain Height Error Data (THED) error estimates. This indicates that the SRTM predicted height error is a good predictor of the random component of the error. Section 4.1 shows the details of this relationship.

e- After removing the height error high and medium frequency components, the residual height error is still significant and exhibits very long wavelength behavior. These errors are due to residual motion errors, and are further discussed in section 3.1.

f- The horizontal resolution of the SRTM data is about 45 m. The resolution is defined as the separation between two measurements such that the correlation between the errors drops to a value of 0.5. This is documented in Chapters 3 and 6.

1.5 SRTM Error Model

A height error model consistent with these observations can be written as

$$\delta h(x) = L(x) + \sigma(x) n(x) \tag{1.3}$$

where $L(x)$ represents the long wavelength error: a function neither homogeneous nor stationary; $\sigma(x)$ represents the spatially varying standard deviation of the high frequency error, which depends on the THED values; and $n(x)$ represents the high frequency error, a unit variance homogeneous stationary random process, statistically independent of $L(x)$, with the following statistical characteristics

$$\begin{aligned} \langle n(x) \rangle &= 0 && (1.4) \\ \langle n(x) n(x') \rangle &= C(|x - x'|) && (1.5) \end{aligned}$$

where $C(|x - x'|)$ represents a correlation function whose correlation length is less than approximately 100 m–400 m (see Section 3.3).

The preceding error model is physically justified as follows: The long wavelength error component corresponds to residual roll (AODA) errors. The envelope function, $\sigma(x)$ corresponds to either modulations of the surface brightness due to surface variability, or the presence of slopes due to topography. Finally, $n(x)$ represents the speckle noise, which decorrelates with a distance given by the width of the system impulse responses, after all spatial filtering has been included.

Notice that given these properties, the error variance is given by

$$\left\langle \delta h^2(x) \right\rangle = \left\langle \delta L^2(x) \right\rangle + \left\langle \delta \sigma^2(x) \right\rangle \tag{1.6}$$

This implies that if the total height variance is known over a continent, and the average height variance is known over a DTED cell, the long wavelength variance can be obtained by subtracting the two known quantities, provided the THED variance does not have much power for wavelengths outside the cell size.

Notice that this proposed error model function is consistent with the results presented in the previous section, but is by no means uniquely determined. It is introduced here for convenience in interpreting the results presented in the next sections.

The structure function for this error model can then be shown to be given by

$$\begin{aligned}\left\langle \left(\delta h(x) - \delta h(x')\right)^2 \right\rangle &= \left\langle \left(L(x) - L(x')\right)^2 \right\rangle + \left\langle \sigma^2(x) \right\rangle + \\ &\quad \left\langle \sigma^2(x') \right\rangle - 2 \left\langle \sigma(x)\sigma(x') \right\rangle C(|x - x'|) \end{aligned} \tag{1.7}$$

For scales much shorter than the scale of variability of the long wavelength errors or the spatially varying THED variance, the structure function can be approximated by

$$\left\langle \left(\delta h(x) - \delta h(x')\right)^2 \right\rangle = 2 \left\langle \sigma^2(\bar{x}) \right\rangle \left(1 - C(|x - x'|)\right) \tag{1.8}$$

i.e., by a function which increases from zero to two times the average variance over a distance roughly equivalent to the correlation length of the high frequency process. In the previous equation, $\bar{x} = (x + x')/2$. This is consistent with the observations presented in Section 3.3.

For scales much longer than the high frequency process correlation length, the structure function is given by

$$\left\langle \left(\delta h(x) - \delta h(x')\right)^2 \right\rangle = \left\langle \left(\delta L(x) - \delta L(x')\right)^2 \right\rangle + \left\langle \left(\sigma^2(x)\right)^2 \right\rangle + \left\langle \left(\sigma^2(x')\right)^2 \right\rangle \tag{1.9}$$

This is a positive function which fluctuates over long distances due to both the long wavelength fluctuations of the large scale error and the spatially varying variance of the short frequency error. This is consistent with the results presented in Section 3.3.

The difference between the error and the average error over an NxN pixel region will be given by

$$\sigma(x) \left(n(x) - \frac{1}{N^2} \sum_{x'} n(x') \right) \tag{1.10}$$

It is not difficult to convince oneself that the variance of this quantity will increase as the size of the averaging box increases, due to the correlation between the high-frequency error and the values used to form the average. In the limit of a very small box, all the errors are correlated, and the variance is zero. On the other hand, if all samples are independent, the box average will result in an accurate estimate of the random error. This result will be used in Chapter 4 to estimate the optimal averaging window size for estimating the random noise.

1.6 Performance Summary and SRTM Error Products

In order to estimate the continental scale absolute height error, we relied mainly on the kinematic GPS data set since, as will be described in the following chapters, there are significant uncertainties associated with the other (non-ocean) GCPs, or high quality data may not be available for the continent.

The SRTM continent-wide absolute height error is estimated by subtracting the interpolated DEM height from the GPS ground-truth. The interpolated datum is a cubic convolution, evaluated at the position of the GPS latitude and longitude. The continent-wide height error distribution (see Figure 1.6 for an example) is estimated, and the continent-wide 90% relative and absolute errors derived directly from it. Table 1.3 presents the estimated errors for each continent.

Since the continent-wide error contains both short and long-wavelength error components, we attempt to separate the random error by averaging the kinematic GPS errors over scales which are

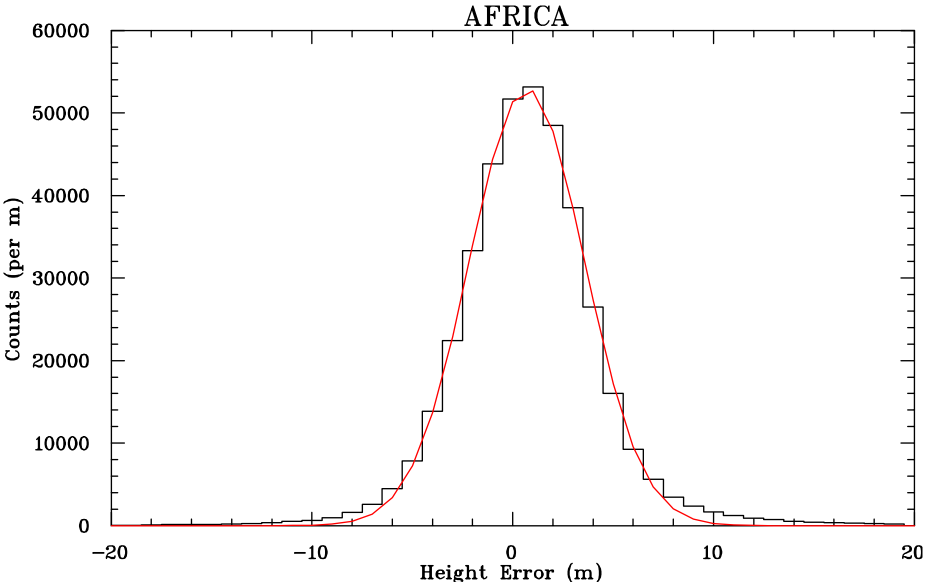

Figure 1.6: Histogram of the SRTM height error measured over the continent of Africa (black), with a Gaussian fit (red).

expected to be larger than the correlation distance of the random error, which is mainly dependent on topography or surface brightness. Although there is no clear-cut separation between residual long-wavelength error (e.g., Figure 1.2) and surface topography, we select the SRTM product cell (1° × 1°) as a convenient scale. The results for the 90% residual long-wavelength error for each continent are presented in Table 1.3.

The geolocation error was estimated using image and height matching of the kinematic GPS transects. The details are presented in Section 5.2, and the results summarized in Table 1.3.

	Africa	Australia	Eurasia	Islands	N. America	S. America
Absolute Geolocation Error	11.9	7.2	8.8	9.0	12.6	9.0
Absolute Height Error	5.6	6.0	6.2	8.0	9.0	6.2
Relative Height Error	9.8	4.7	8.7	6.2	7.0	5.5
Long Wavelength Height Error	3.1	6.0	2.6	3.7	4.0	4.9

Table 1.3: Summary of SRTM height performance. All quantities represent 90% errors in meters.

Since the random error is dependent on the topography and radar brightness, continent-wide averages are of limited usefulness. An estimate of the random error can be obtained from the interferometric correlation. This estimate is stored in the THED product, which is available for each height post. Section 4.1 presents the validation of the THED data product.

In addition to the THED and the continent-wide error estimate, it is desirable to estimate the combined error characteristics on a cell (1° × 1°) and subcell (1/8° × 1/8°) basis. To do so, we use the error model presented in Section 1.5, as described in the following subsections. This information is then stored in the SRTM height data headers.

1.6.1 Cell and Subcell Random Errors

Notice that averaging over $n(x)$ but not over the process determining the THED dependent standard deviation variation, the expected height variance at a point (neglecting, for the moment, the long wavelength error) is given by

$$\left\langle \delta h^2(x) \right\rangle_n = \sigma^2(x) \tag{1.11}$$

The average error variance over a box (cell or subcell) is then given by

$$\left\langle \left\langle \delta h^2(x) \right\rangle_n \right\rangle_B = \left\langle \sigma^2(x) \right\rangle_B \tag{1.12}$$

where $\langle\rangle_B$ indicates spatial averaging over the box (cell or subcell).

Assuming Gaussian statistics, and making the same approximation made in the NIMA SRTM Data Product Specification (DPS) document, the 90% random error over the cell or subcell is given by

$$\text{Random Error} = 1.64\sqrt{\langle \sigma^2(x) \rangle_B} \tag{1.13}$$

1.6.2 Cell and Subcell Absolute Errors

If the long wavelength error is defined as that error which has scales greater than the a nominal cell size (say 110 km, or 1 degree at the Equator), an estimate of the energy contained in the long wavelength error can be obtained from the ground truth by averaging the observed error over scales smaller than the nominal cell size, and computing the variance of the residual. We will write that quantity as $\left\langle \delta L^2(x) \right\rangle_C$, where the subscript C indicates continental averaging.

Given the assumption of independence between long wavelength and short wavelength processes, the expected absolute error variance over the box (cell or subcell) is given by

$$\left\langle \delta h^2(x) \right\rangle_{nBC} = \left\langle L^2(x) \right\rangle_C + \left\langle \sigma^2(x) \right\rangle_B \tag{1.14}$$

Assuming Gaussian statistics, and making the same approximation made in the NIMA SRTM DPS document, the 90% absolute error over the cell or subcell is given by

$$\text{Absolute Error} = 1.64\sqrt{\langle L^2(x) \rangle_C + \langle \sigma^2(x) \rangle_B} \tag{1.15}$$

Notice that given the absolute and random errors, it is possible to recover the continent long wavelength error, so that this field could be updated if new estimates of the long wavelength error became available with better ground truth.

1.6.3 Cell and Subcell Relative Errors

Under the assumption that the separation between two points is small enough so that long wavelength errors are identical for both points (as will be the case for the SRTM cells and subcells, by definition), the average (over the high frequency process, but not over the envelope) relative error variance can be written as

$$\left\langle (\delta h(x) - \delta h(x'))^2 \right\rangle \approx \sigma^2(x) + \sigma^2(x') - 2\sigma(x)\sigma(x')C(|x - x'|) \tag{1.16}$$

and, if the separation between x and x' is greater than the correlation length, as will be the case for most points inside a cell or subcell, we have that

$$\left\langle (\delta h(x) - \delta h(x'))^2 \right\rangle \approx \sigma^2(x) + \sigma^2(x') \tag{1.17}$$

i.e., the relative error variance is the sum of the variances of the high frequency process. (Notice that this approximation is equivalent to assuming that the correlation function is a delta function). The average value of the relative error variance over a cell or subcell box is then given by

$$\left\langle (\delta h(x) - \delta h(x'))^2 \right\rangle_B \approx \left\langle \sigma^2(x) + \sigma^2(x') \right\rangle_B = 2 \left\langle \sigma^2(x) \right\rangle_B \tag{1.18}$$

Making the same assumptions as for the absolute error, the 90% relative error over a cell or subcell is given by

$$\text{Relative Error} = 1.64\sqrt{2 \left\langle \sigma^2(x) \right\rangle_B} \tag{1.19}$$

Chapter 2

Absolute Height Error

In this chapter, we examine the difference between the SRTM height estimates and those from other sources. No attempt is made to corregister the data sets. The spatial distribution of the errors will be examined in the next chapter.

2.1 Kinematic GPS GCP Comparison

The most accurate measure of the height performance of SRTM over typical land surfaces is given by comparing with the kinematic GPS transects. Table 2.1 summarizes the performance, while Figures 2.1–2.6 show the histograms and cumulative distribution function for the height error and its magnitude.

Continent	Mean	Standard Deviation	90% Absolute Error
Africa	1.3	3.8	6.0
Australia	1.8	3.5	6.0
Eurasia	-0.7	3.7	6.6
North America	0.1	4.0	6.5
New Zealand	1.4	5.9	10.0
South America	1.7	4.1	7.5

Table 2.1: Summary of kinematic GPS GCP comparison with SRTM data. All quantities are in meters.

Examination of these results shows a very consistent behavior for the means, standard deviations and absolute errors. The main exception is New Zealand, which has a much larger standard deviation and 90% error, but also many fewer points. The discrepancy may be due to the rugged terrain encountered by the New Zealand transect. Note that the main draw-back of the kinematic GPS data is that, since it is limited to roads, it will selectively avoid very rugged terrain. Thus, the estimates presented in Table 2.1 may be optimistic for these regions.

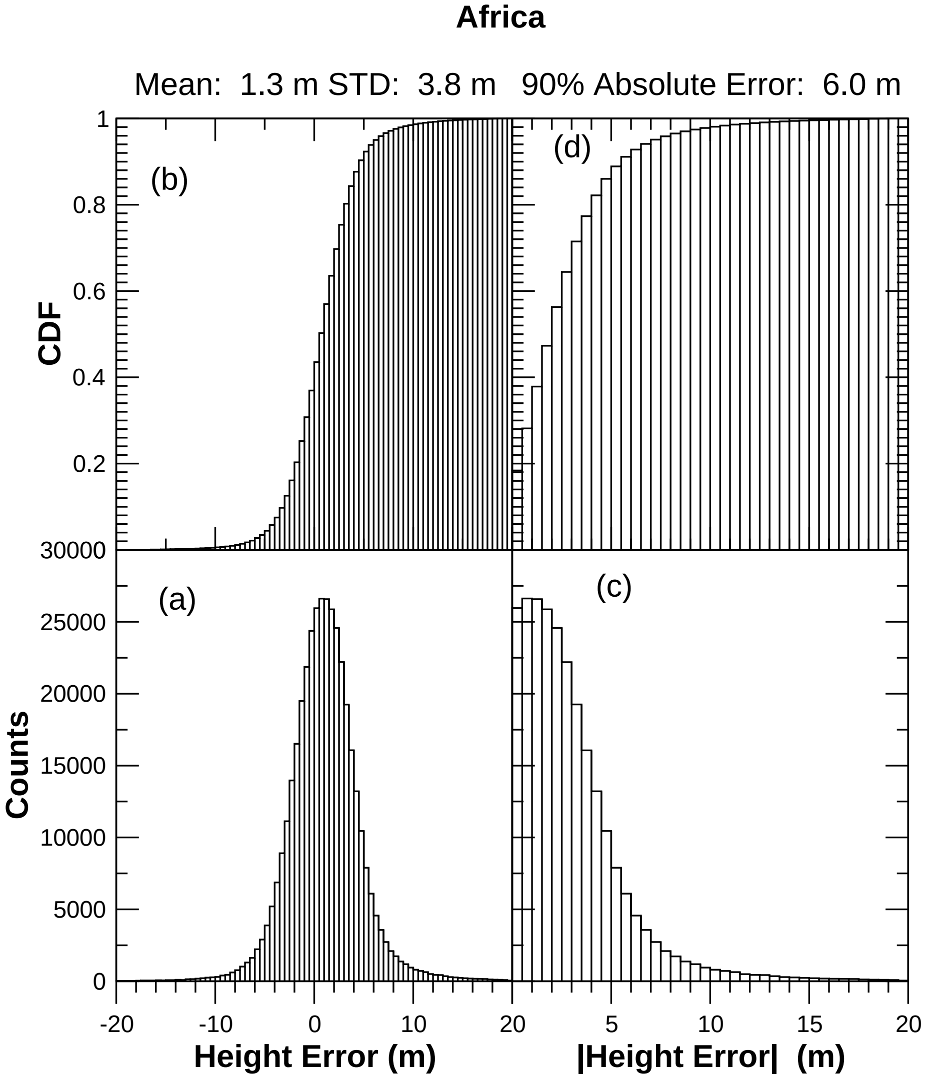

Figure 2.1: Africa kinematic GPS height comparison. Panel (a) shows the distribution of the signed error; panel (b) the corresponding cummulative distribution function; panel (c) is the distribution of the error magnitude; and panel (d) is the cummulative distribution of the error magnitude.

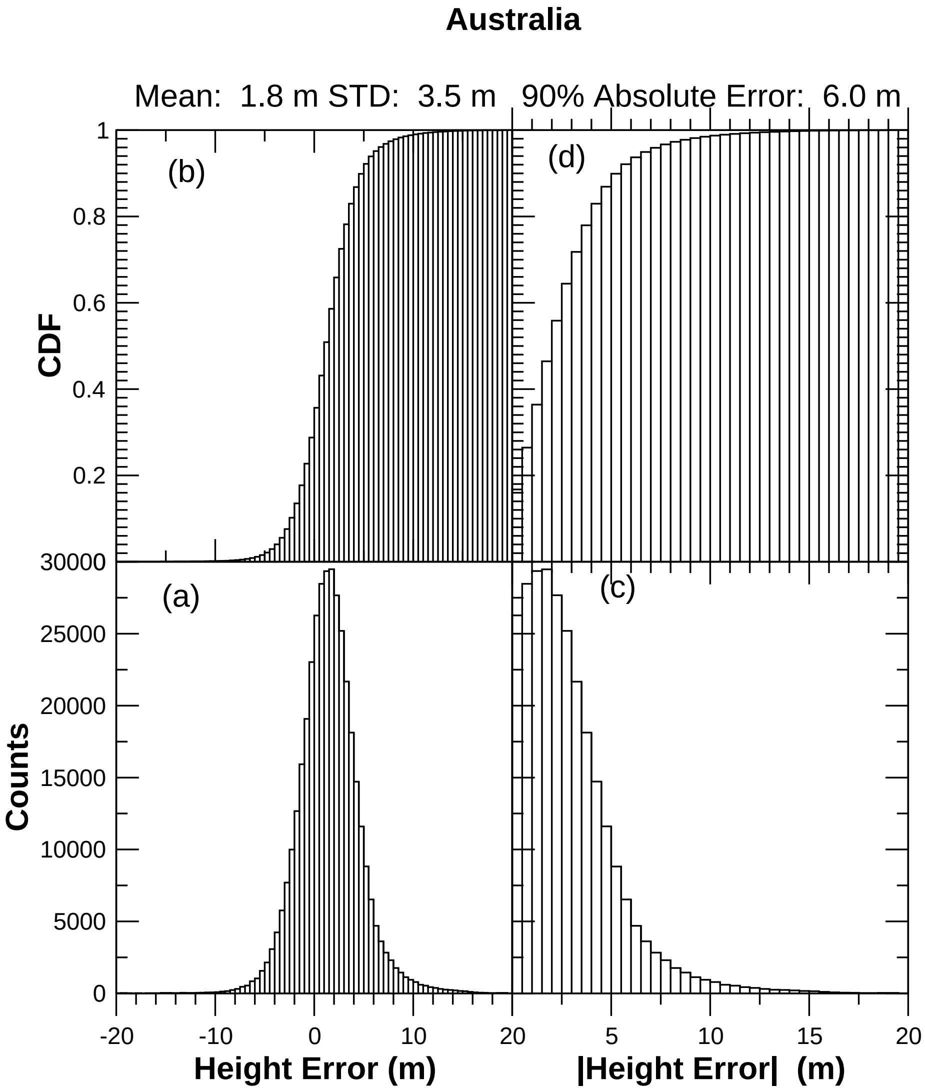

Figure 2.2: Australia kinematic GPS height comparison. Panel (a) shows the distribution of the signed error; panel (b) the corresponding cummulative distribution function; panel (c) is the distribution of the error magnitude; and panel (d) is the cummulative distribution of the error magnitude.

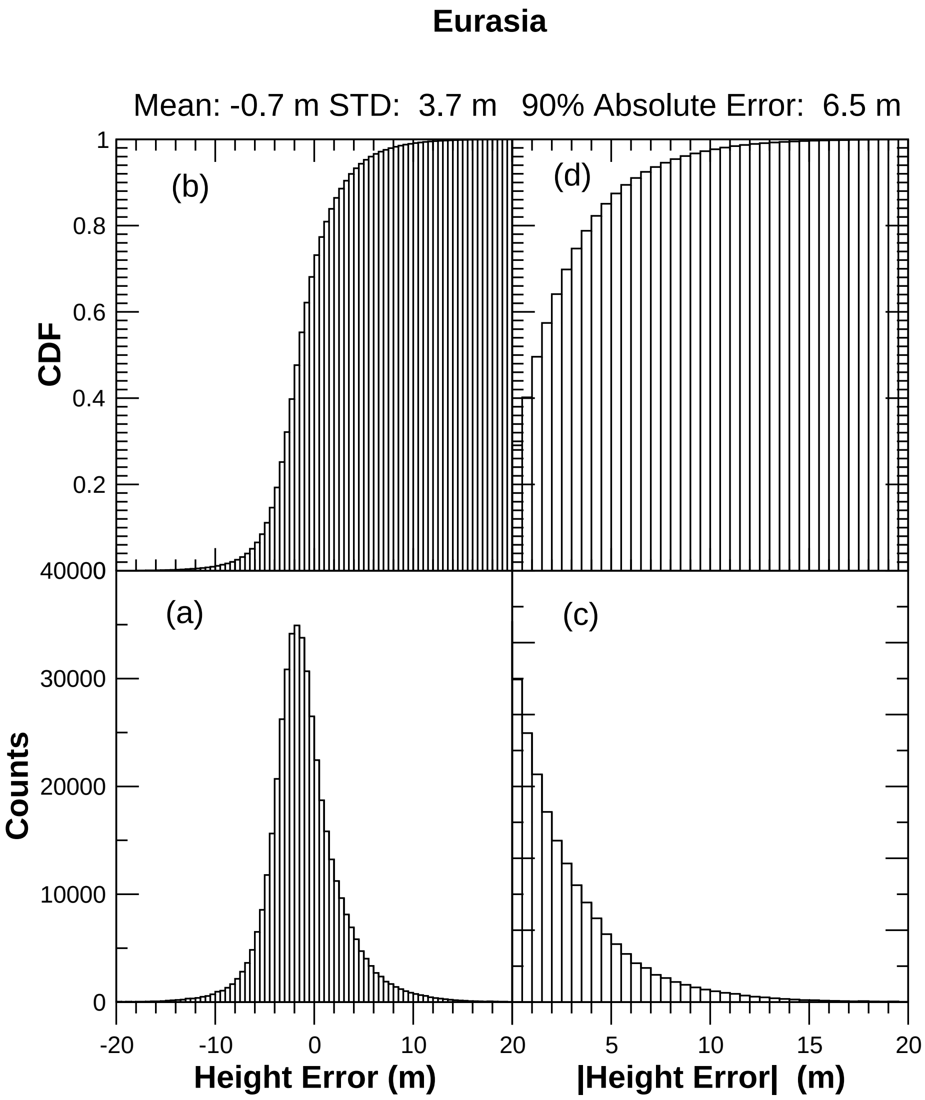

Figure 2.3: Eurasia kinematic GPS height comparison. Panel (a) shows the distribution of the signed error; panel (b) the corresponding cummulative distribution function; panel (c) is the distribution of the error magnitude; and panel (d) is the cummulative distribution of the error magnitude.

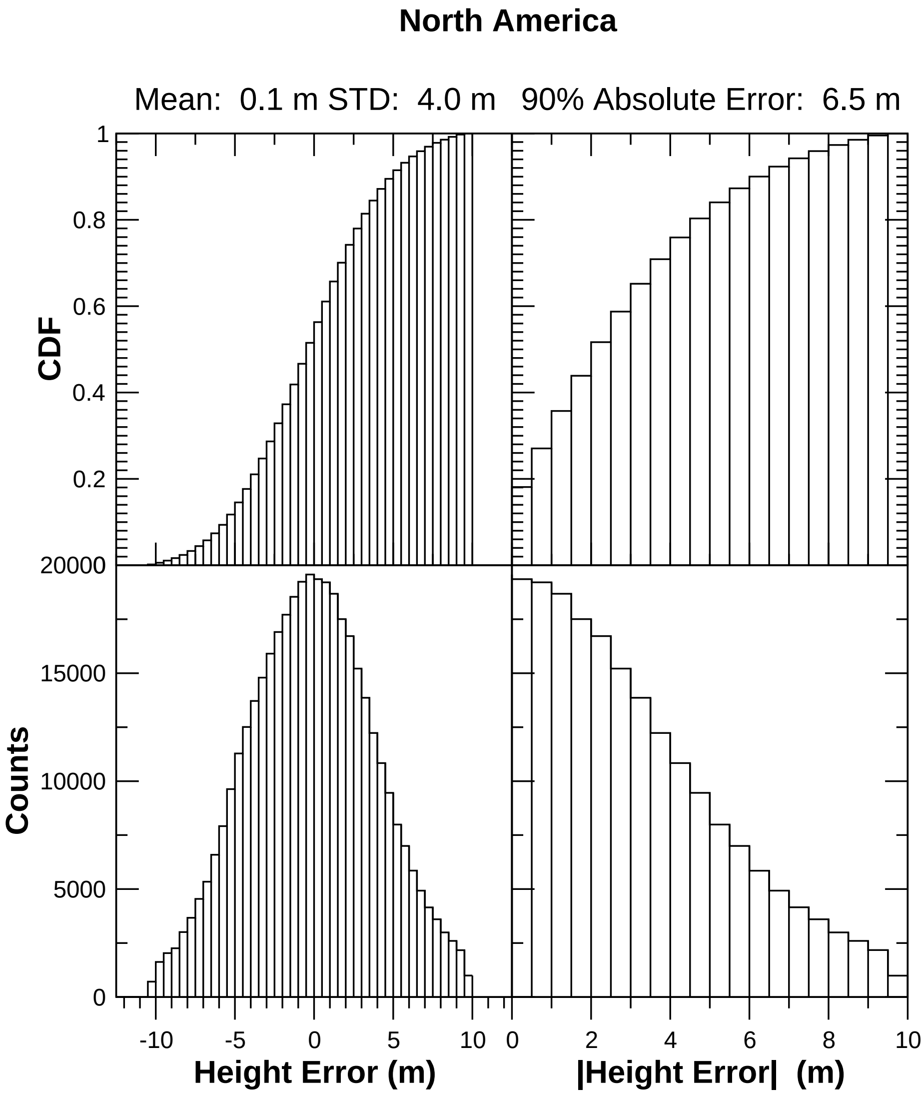

Figure 2.4: North America kinematic GPS height comparison. Panel (a) shows the distribution of the signed error; panel (b) the corresponding cummulative distribution function; panel (c) is the distribution of the error magnitude; and panel (d) is the cummulative distribution of the error magnitude.

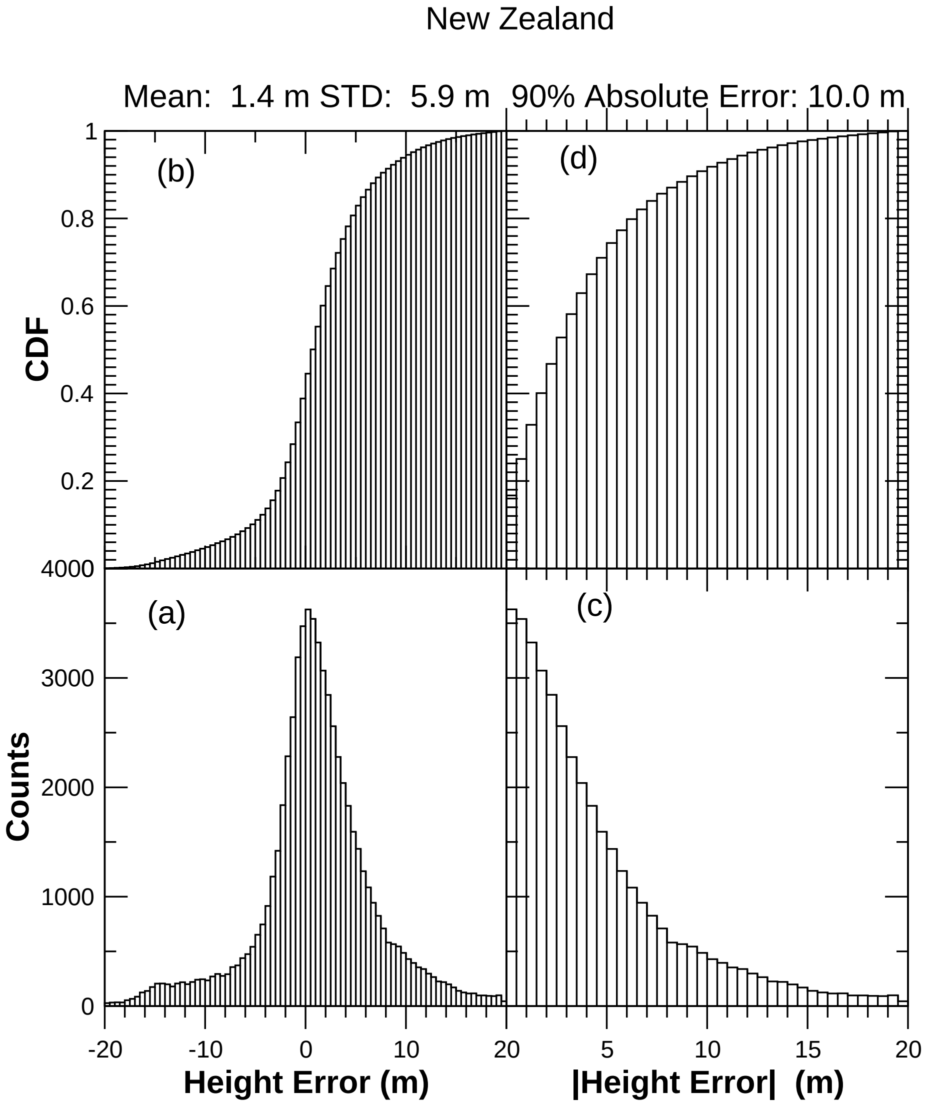

Figure 2.5: New Zealand kinematic GPS height comparison. Panel (a) shows the distribution of the signed error; panel (b) the corresponding cummulative distribution function; panel (c) is the distribution of the error magnitude; and panel (d) is the cummulative distribution of the error magnitude.

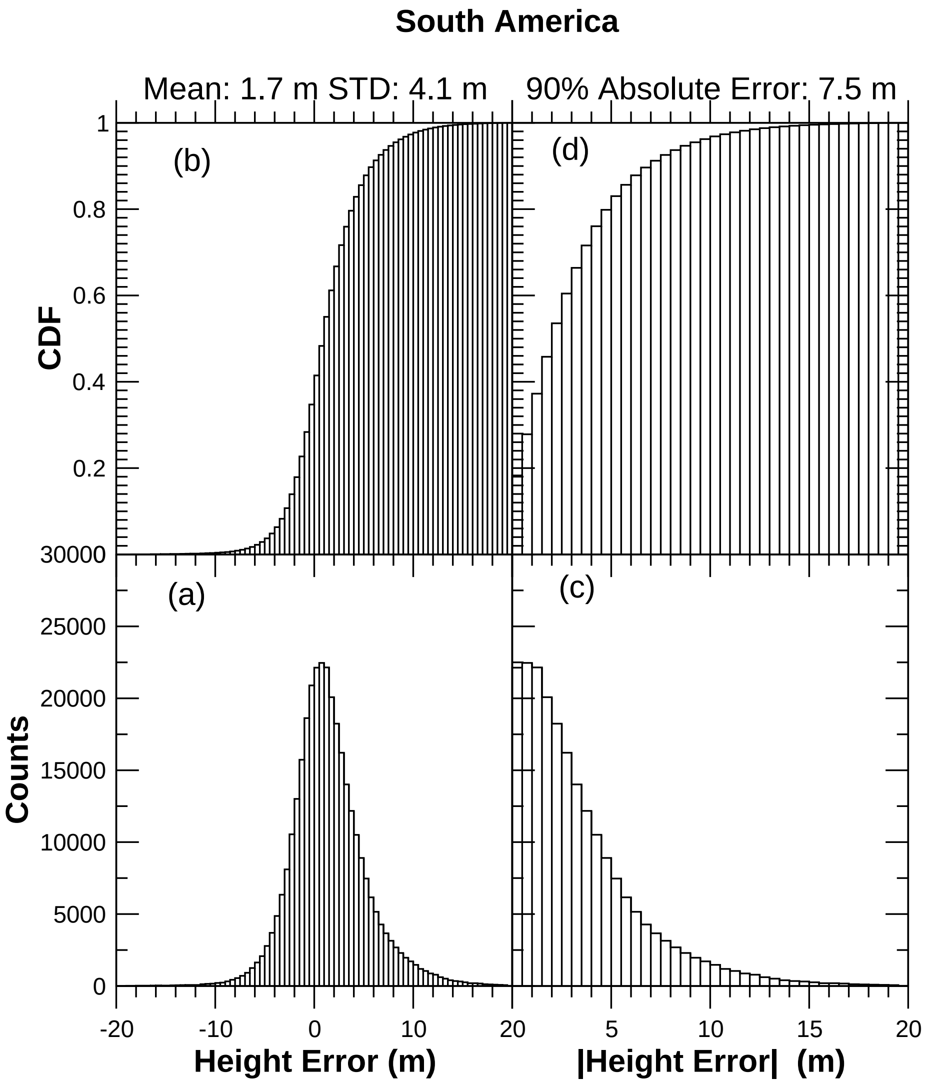

Figure 2.6: South America kinematic GPS height comparison. Panel (a) shows the distribution of the signed error; panel (b) the corresponding cummulative distribution function; panel (c) is the distribution of the error magnitude; and panel (d) is the cummulative distribution of the error magnitude.

2.2 DTED Level 2 Comparison

Table 2.2 summarizes the continental average results for the DTED 2 comparisons, while Figure 2.7 summarizes the global performance in a histogram. The results for all the continents are roughly consistent, with the exception of South America, which shows a significantly higher mean deviation.

In order to investigate the source of large 90% errors, we plot in Figure 2.8 the behavior of the 90% error against the median and standard deviation of the height difference. We also present in Tables 2.3–2.6 the detailed values for each cell. The largest differences are due to mean shifts between the two data sets. Since the SRTM data is continentally adjusted against the ocean, and because the kinematic GPS data did not show these large deviations, it is possible that the average errors may be present in the DTED 2 data, rather than the SRTM data.

On the other hand, Figure 2.8 shows that large errors can also occur due to large RMS differences. These may be due to degraded SRTM performance over regions of large slopes, such as Afghanistan (see next chapter).

Continent	Average	Median	90% Diff	STD	RMS
Africa	2.44	2.30	8.80	4.68	5.53
Eurasia	-0.07	-0.09	8.07	4.50	5.36
N.America	1.38	1.40	7.67	4.01	4.88
S.America	11.36	11.20	16.88	4.60	12.77

Table 2.2: Statistics for the height difference between SRTM and DTED level 2. All quantities are in meters.

Cell	Average	Median	90% Diff	STD	RMS
n09e007	2.85	2.77	6.55	2.96	4.11
n21e031	2.73	2.20	7.92	4.52	5.28
n21e039	4.97	4.48	11.82	5.45	7.38
n21e040	-0.07	0.34	12.17	7.10	7.10
n22e048	1.72	1.70	5.54	3.36	3.77
Average	2.44	2.30	8.80	4.68	5.53

Table 2.3: Statistics for the height difference between SRTM and DTED level-2 data for Africa. All quantities are in meters. The cell name has the format n(latitude)e(longitude) denoting the south-west corner of the SRTM height cell

Cell	Average	Median	90% Diff	STD	RMS
n29e066	-3.17	-2.92	8.85	4.82	5.76
n25e119	1.94	1.64	6.93	4.07	4.50
n30e061	4.64	4.73	6.93	1.98	5.04
n30e064	0.02	0.01	5.24	3.26	3.26
n30e065	-1.70	-1.67	5.84	3.42	3.82
n30e066	-2.18	-2.06	6.72	3.71	4.30
n31e064	-1.20	-0.98	5.15	2.93	3.16
n31e065	-0.36	-0.33	5.68	4.20	4.22
n31e066	-4.71	-4.48	8.99	3.88	6.10
n32e062	3.23	3.38	6.12	3.04	4.43
n32e064	1.21	1.40	9.02	6.23	6.35
n32e065	-0.38	-0.52	9.20	6.51	6.52
n33e069	-1.31	-1.23	7.50	4.83	5.01
n34e062	1.72	1.91	5.71	3.36	3.77
n34e069	-2.31	-2.13	11.48	7.06	7.42
n34e070	1.72	2.00	8.92	5.89	6.13
n35e062	6.00	6.18	10.38	3.62	7.01
n36e065	-2.64	-2.67	6.47	3.04	4.02
n36e066	-4.15	-3.90	8.24	3.51	5.44
n36e067	-2.91	-2.68	9.77	5.82	6.51
n36e068	-4.17	-3.93	9.02	5.13	6.61
n37e066	-1.11	-1.04	3.67	2.10	2.37
n37e068	-0.18	-0.10	5.40	3.64	3.65
n44e017	1.97	0.66	14.08	8.51	8.73
n44e020	1.83	1.30	7.32	4.41	4.77
n46e014	6.40	5.06	17.20	8.09	10.32
Average	-0.07	-0.09	8.07	4.50	5.36

Table 2.4: Statistics for the height difference between SRTM and DTED level-2 data for Eurasia. All quantities are in meters. The cell name has the format n(latitude)e(longitude) denoting the south-west corner of the SRTM height cell

Cell	Average	Median	90% Diff	STD	RMS
n21w079	1.15	1.07	4.99	2.88	3.10
n35w080	-1.50	-0.78	10.98	6.42	6.59
n31w098	6.30	6.22	9.83	2.65	6.84
n42w100	0.73	0.69	7.88	4.79	4.85
n48w103	-0.53	-0.75	5.79	3.58	3.62
n34w117	2.11	1.95	6.58	3.72	4.27
Average	1.38	1.40	7.67	4.01	4.88

Table 2.5: Statistics for the height difference between SRTM and DTED level-2 data for North America. All quantities are in meters. The cell name has the format n(latitude)e(longitude) denoting the south-west corner of the SRTM height cell

Cell	Average	Median	90% Diff	STD	RMS
w066s19	22.79	22.48	29.71	6.51	23.71
w068s19	14.22	13.88	17.58	1.26	14.27
w065s20	5.45	4.99	14.98	7.97	9.65
w067s20	4.96	4.96	9.30	3.82	6.26
w068s20	9.36	9.67	12.84	3.43	9.97
Average	11.36	11.20	16.88	4.60	12.77

Table 2.6: Statistics for the height difference between SRTM and DTED level-2 data for South America. All quantities are in meters. The cell name has the format n(latitude)e(longitude) denoting the south-west corner of the SRTM height cell

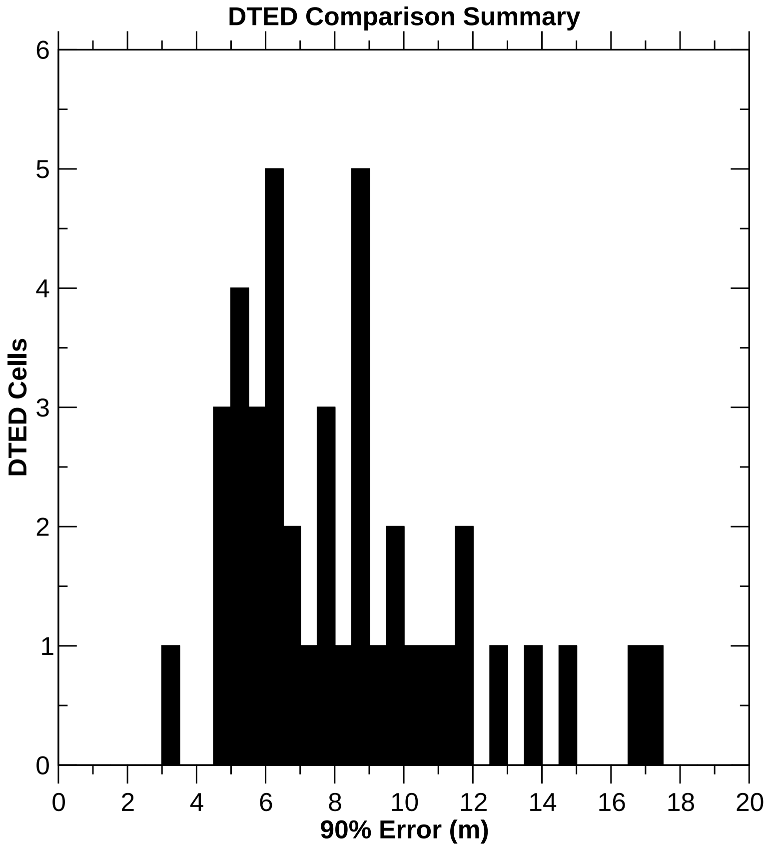

Figure 2.7: Histogram of the 90% error values for the comparison of the SRTM height data against the DTED Level-2 data.

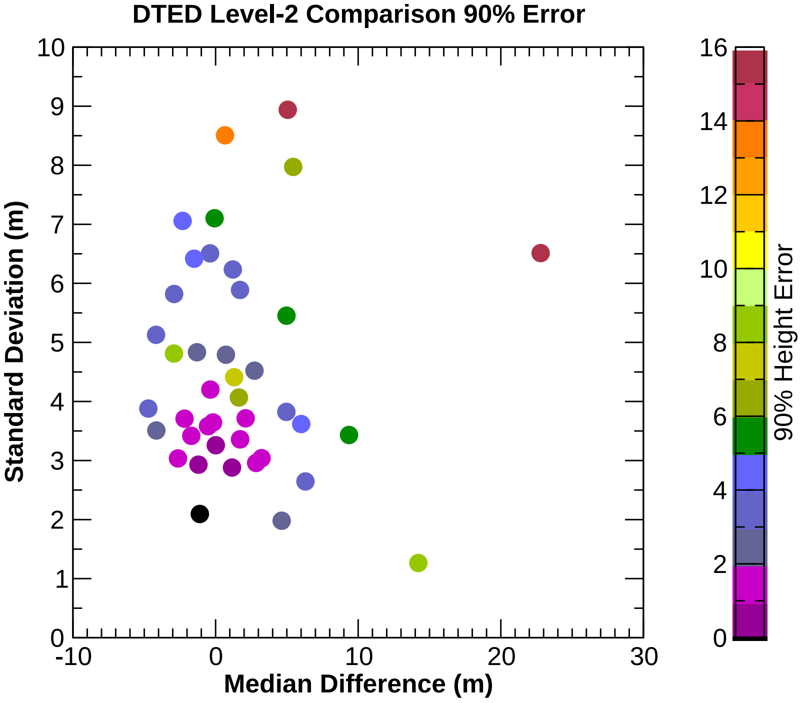

Figure 2.8: 90% Height errors plotted against height difference median and standard deviations for the SRTM to DTED Level-2 comparisons. Note the largest differences are due to a mean shift between the two data sets.

2.3 Height Patch Comparison

Table 2.7 and Figure 2.9 summarize the patch comparison results. The results show no consistent mean shift, but the 90% error is larger than for either the kinematic GPS or the DTED 2 comparisons.

In order to examine more closely the additional source in error, Figure 2.10 presents the behavior of the 90% error as a function of the median difference and the standard deviation. The detailed results are presented in Tables 2.9–2.12. What these results show is that a large part of the differences can be attributed to mean shifts between the two data sets. These shifts tend to average out over a continent, indicating that the variability may be due to errors in the mean height for selected patches.

Continent	Min	Max	Average	Median	90% Diff	STD	RMS
Africa	-39.79	42.13	4.13	3.31	10.15	4.26	7.63
Australia	-25.28	21.73	2.10	2.25	7.67	3.44	5.04
Eurasia	-40.17	36.44	-1.79	-1.36	12.48	5.99	8.28
N.America	-40.01	38.79	-0.61	-0.54	9.99	4.86	6.74

Table 2.7: Statistics for the height difference between SRTM and height patches. All quantities are in meters.

Patch	Lat	Lon	Min.	Max.	Average	Median	90% Diff	STD	RMS
ex2p4	-23.5	133.0	-27.91	7.67	-2.30	-1.95	5.37	2.43	3.34
ex2p7	-35.5	149.0	-20.27	26.17	5.27	5.21	9.90	3.79	6.50
ex6p02	-23.0	118.7	-27.66	31.36	3.33	3.50	7.75	4.10	5.28
Average			-25.28	21.73	2.10	2.25	7.67	3.44	5.04

Table 2.8: Statistics for the height difference between SRTM and height patch data for Australia. All height quantities are in meters. Latitude and longitude are approximated to the nearest tenth of a degree.

Patch	Lat	Lon	Min.	Max.	Average	Median	90% Diff	STD	RMS
ss10a1	28.6	33.6	-73.75	79.43	14.90	15.00	27.29	11.33	18.72
ss10b1	28.9	33.9	-77.03	67.04	15.92	16.10	20.86	4.71	16.60
ss10c1	28.8	34.9	-78.17	79.54	5.35	5.64	17.26	9.45	10.86
ss10d1	27.9	34.1	-65.45	48.10	3.87	4.49	12.20	6.82	7.84
ss52a	-30.8	23.8	-37.62	39.93	4.88	5.18	10.66	5.18	7.12
ss52b	-30.3	25.3	-23.40	28.61	4.75	5.02	9.86	4.50	6.54
ss52c	-31.1	25.2	-37.98	44.16	2.06	2.20	4.70	2.66	3.36
ss52d	-31.2	24.7	-46.15	20.99	0.30	0.37	3.47	2.33	2.35
ss52e	-30.5	24.4	-23.68	9.86	-1.61	-1.62	4.46	2.30	2.81
ss56a	-2.3	29.3	-78.96	79.39	-3.52	-4.01	14.97	9.46	10.09
ss56b	-1.3	29.7	-24.31	21.68	-0.93	-0.81	4.61	2.96	3.10
ss56c	-1.8	30.2	-42.88	53.41	5.88	5.69	10.44	4.12	7.18
ss56d	-2.5	30.2	-27.59	22.69	0.22	0.41	4.98	3.20	3.21
ss56e	-2.1	29.9	-15.23	23.31	1.05	1.02	4.68	2.76	2.95
ss61a	9.5	10.8	-73.95	74.44	7.72	7.78	11.97	4.37	8.87
ss61b	10.5	11.6	-46.30	53.11	5.30	5.37	8.78	3.53	6.37
ss61c	9.7	11.9	-39.32	65.60	5.49	5.37	9.68	3.97	6.78
ss61d	9.2	11.8	-62.55	48.69	6.63	6.82	9.99	3.19	7.36
ss61e	9.8	11.3	-67.26	77.08	5.31	5.55	8.63	3.57	6.40
ss63a	30.5	-5.3	-23.82	13.62	-5.11	-5.17	8.86	3.09	5.98
ss63b	31.3	-5.1	-32.83	41.15	-1.45	-1.51	8.10	4.86	5.08
ss63c	31.2	-4.6	-41.19	53.64	3.59	3.71	7.29	3.36	4.92
ss63d	30.7	-4.1	-21.19	17.80	-0.60	-0.48	4.13	2.66	2.72
ss63e	30.5	-4.7	-19.16	14.36	-0.44	-0.46	4.76	2.89	2.93
ss101	28.5	34.0	-38.98	49.22	8.99	9.25	14.86	5.11	10.34
ex1p9	15.0	44.0	-35.43	50.13	6.03	6.53	13.19	6.19	8.64
ex2p11	34.0	50.0	-47.87	58.98	-3.16	-3.34	8.58	5.06	5.97
ex3p53	-23.5	29.1	-7.65	6.00	-1.26	-1.28	3.35	1.63	2.06
ex3p55	-2.7	35.5	-33.55	23.65	-3.96	-3.89	9.42	4.45	5.96
ex3p57	-17.0	31.0	-31.13	39.56	4.93	4.84	8.36	3.02	5.78
ex3p62	13.5	22.5	-13.48	12.85	-1.24	-1.27	3.71	1.91	2.28
ex4p59	22.5	6.5	-74.77	27.48	-2.48	-2.36	6.04	3.30	4.13
ex5p54	-24.5	16.5	-7.51	12.51	2.60	2.51	4.43	1.49	3.00
ex5p58	-9.5	16.5	-22.30	14.42	2.26	2.37	4.89	2.28	3.22
Average			-38.81	37.98	2.42	2.50	8.88	4.01	6.06

Table 2.9: Statistics for the height difference between SRTM and height patch data for Africa. All height quantities are in meters. Latitude and longitude are approximated to the nearest tenth of a degree.

Patch	Lat	Lon	Min.	Max.	Average	Median	90% Diff	STD	RMS
ss12a	34.1	62.6	-38.33	63.86	1.87	1.76	10.96	6.65	6.91
ss12b	34.6	63.0	-31.75	29.24	0.31	0.25	6.76	4.21	4.22
ss12c	34.5	63.8	-70.77	79.73	-1.83	-2.36	28.38	18.48	18.57
ss12d	33.6	62.8	-40.64	48.94	3.58	3.39	12.55	7.00	7.86
ss12e	34.0	62.8	-43.58	36.63	0.86	0.93	9.60	5.87	5.93
ss13a	41.4	76.5	-79.38	74.44	-4.81	-4.67	17.99	10.62	11.65
ss13b	41.8	77.0	-68.79	79.68	-4.47	-4.32	10.99	6.00	7.48
ss13c	41.6	77.5	-57.09	43.06	-6.66	-6.23	14.37	6.22	9.11
ss13d	40.9	75.8	-77.60	77.43	0.89	0.58	9.72	6.94	7.00
ss13e	41.3	76.8	-31.68	42.03	-0.36	-0.46	7.51	4.75	4.76
ss16a	53.9	89.2	-35.91	38.50	-3.49	-2.68	10.93	5.07	6.15
ss16b	54.3	89.2	-69.48	14.21	-14.58	-13.60	27.35	9.28	17.28
ss16c	54.6	90.3	-20.16	27.33	-5.92	-5.85	8.11	1.97	6.23
ss16d	53.5	90.2	-25.88	16.18	-5.75	-5.74	11.68	4.58	7.35
ss16e	53.9	90.1	-24.88	15.63	-7.29	-7.21	13.88	5.06	8.88
ss21a	49.8	121.3	-30.71	19.60	-4.62	-3.39	11.14	4.73	6.61
ss21b	50.3	121.1	-12.64	20.88	3.03	2.81	7.29	3.29	4.47
ss21c	50.6	122.0	-24.44	19.59	-1.20	-0.91	7.59	4.49	4.65
ss21d	49.8	122.4	-29.77	22.99	-7.71	-7.37	14.48	5.10	9.25
ss21e	50.0	122.1	-45.73	27.86	-7.72	-6.31	16.97	6.63	10.17
ss29a	16.8	100.6	-32.82	17.67	0.81	0.92	5.83	3.58	3.67
ss29b	17.4	100.5	-23.43	79.26	22.36	21.31	32.59	9.00	24.10
ss29c	17.3	101.1	-28.65	28.87	2.75	2.67	7.61	3.84	4.73
ss29d	16.9	101.8	-67.89	30.44	2.39	3.29	8.80	5.53	6.03
ss29e	16.9	101.1	-78.79	51.72	-31.25	-31.98	39.05	7.56	32.15
ss38a	39.8	26.8	-49.60	38.61	-0.29	-0.16	9.42	5.74	5.75
ss38b	40.1	26.8	-17.15	20.00	1.84	1.84	6.28	3.40	3.86
ss38c	40.5	27.8	-23.24	24.56	-1.19	-1.14	8.20	4.82	4.96
ss38d	39.6	28.4	-11.23	29.19	7.48	7.33	11.58	3.41	8.22
ss38e	40.1	27.5	-26.06	42.66	2.56	2.60	7.99	4.35	5.05
ex1p26	31.0	90.0	-10.09	19.38	5.86	5.87	8.49	2.26	6.28
ex1p27	37.0	103.9	-19.30	31.53	7.79	7.90	12.14	3.77	8.66
ex1p34	48.0	8.0	-44.62	32.32	-6.69	-6.88	15.33	7.07	9.73
ex1p36	49.0	21.0	-25.80	21.89	0.89	0.86	5.84	3.48	3.60
ex2p8	42.0	44.0	-23.58	17.02	-0.68	-0.60	4.39	2.91	2.99
ex2p15	49.0	76.0	-16.90	16.59	-0.35	-0.31	5.04	3.07	3.09
ex2p22	55.0	129.5	-27.37	4.50	-6.71	-5.68	12.65	4.33	7.99
ex4p25	23.0	77.0	-12.97	9.56	-0.01	-0.05	3.23	1.98	1.98
ex4p28	25.0	104.0	-51.67	36.90	-2.63	-2.76	8.51	4.82	5.49
ex4p30	42.0	121.0	-23.46	9.43	-6.18	-6.21	9.71	2.95	6.85
ex4p32	39.5	-4.5	-23.19	14.93	-3.37	-3.25	6.98	2.94	4.47
ex5p17	43.5	89.0	-79.35	72.36	-5.78	-4.58	18.73	9.92	11.48
ex5p19	56.0	107.5	-35.90	11.39	-5.48	-5.23	12.18	6.19	8.26
ex5p33	46.0	2.0	-42.34	18.14	-3.37	-1.85	12.76	6.46	7.28
ex6p14	39.0	75.5	-72.24	58.34	4.66	5.43	16.04	9.35	10.45
ex6p18	39.5	54.5	-31.58	29.72	1.59	1.67	3.31	1.75	2.37
ex6p20	47.0	100.0	-23.98	34.92	-2.53	-2.49	5.88	2.90	3.85
ex6p23	33.0	75.0	-75.77	79.72	-4.25	-3.71	15.12	8.91	9.87
ex6p24	10.0	77.0	-70.54	62.65	-1.64	-1.64	12.04	7.38	7.56
ex6p35	55.9	-3.0	-79.99	79.99	-2.14	-0.51	40.00	28.88	28.96
Average			-40.17	36.44	-1.79	-1.57	12.48	5.99	8.28

Table 2.10: Statistics for the height difference between SRTM and height patch data for Eurasia.

Patch	Lat	Lon	Min.	Max.	Average	Median	90% Diff	STD	RMS
ss42a	30.0	-108.1	-47.03	20.92	-10.35	-9.88	19.36	6.90	12.44
ss42b	31.1	-107.4	-38.97	11.35	-4.82	-4.51	9.36	3.79	6.13
ss42c	30.9	-107.1	-49.64	41.32	-10.86	-10.59	14.86	3.73	11.48
ss42d	29.9	-106.9	-133.52	118.57	-6.61	-6.60	10.79	6.33	9.15
ss42e	30.6	-107.7	-90.39	91.46	-7.66	-7.34	16.37	7.61	10.80
ss44a	37.5	-116.1	-68.61	81.28	7.65	7.36	12.81	4.78	9.02
ss44b	37.9	-116.1	-57.13	47.01	5.78	5.72	11.42	4.90	7.58
ss44c	38.1	-115.7	-44.42	64.13	2.18	2.04	10.02	6.24	6.61
ss44d	36.8	-115.1	-129.62	144.79	0.85	0.53	12.05	10.16	10.20
ss44e	37.5	-115.5	-46.45	38.11	4.16	4.28	6.81	3.31	5.32
ss47a	34.5	-95.6	-20.18	23.25	1.45	1.78	8.59	5.05	5.25
ss47b	35.1	-94.6	-18.90	19.15	1.95	2.31	6.48	3.58	4.08
ss47c	34.7	-94.1	-19.53	28.22	2.49	2.50	9.90	5.53	6.06
ss47d	34.4	-94.1	-20.79	28.76	-0.15	-0.63	9.32	5.74	5.75
ss47e	34.5	-94.9	-15.50	26.76	4.98	6.14	11.67	5.91	7.73
ss51a	40.4	-79.0	-31.35	24.80	-4.99	-4.67	12.59	5.85	7.69
ss51b	40.8	-79.0	-22.96	28.14	1.26	1.16	9.46	5.52	5.66
ss51c	41.2	-77.7	-17.88	21.37	-2.18	-2.26	7.89	4.27	4.79
ss51d	40.7	-77.7	-26.77	11.95	-6.98	-7.51	12.31	4.54	8.32
ss51e	41.0	-78.3	-21.62	25.79	3.58	4.19	10.00	5.24	6.35
ex4p46	35.4	-102.1	-8.84	26.04	2.08	2.07	4.45	1.90	2.81
ex4p48	47.0	-96.0	-7.52	5.54	-1.80	-1.82	3.22	1.13	2.13
ex4p50	45.0	-91.5	-30.60	17.07	-4.67	-5.07	8.84	4.11	6.22
ex5p41	26.0	-101.0	-21.86	19.38	4.05	4.08	6.18	1.88	4.46
ex6p45	40.0	-105.1	-19.70	7.15	-6.88	-6.89	9.87	2.43	7.30
Average			-40.39	38.89	-1.02	-0.94	10.18	4.82	6.93

Table 2.11: Statistics for the height difference between SRTM and height patch data for North America. All height quantities are in meters. Latitude and longitude are approximated to the nearest tenth of a degree.

Patch	Lat	Lon	Min.	Max.	Average	Median	90% Diff	STD	RMS
ss66a	9.6	-75.1	-27.06	23.84	0.16	0.42	6.71	4,21	4.21
ss66b	10.6	-75.2	-24.45	30.13	0.50	0.50	7.86	4.79	4.81
ss66c	10.7	-73.6	-76.17	31.90	-17.71	-17.27	26.42	7.19	19.12
ss66d	10.1	-73.9	-45.12	30.99	-1.26	-0.97	8.84	5.19	5.34
ss66e	10.8	-73.8	79.83	79.94	-17.07	-17.08	27.77	10.23	19.90
ss68a	-4.3	-79.7	-72.19	44.09	-3.88	-4.06	15.04	8.42	9.27
ss68b	-4.9	-79.5	-77.43	79.77	-0.84	-2.36	20.45	13.85	13,88
ss68c	-4.1	-78.4	-65.64	79.95	7.10	6.38	19.98	10.68	12.83
ss70a	-28.6	-49.7	-79.20	79.39	-1.15	1.21	11.64	8.98	9.06
ss70b	-28.6	-50.2	-21.45	12.08	-3.60	-3.54	6.55	2.52	4.39
ss70c	-28.0	-50.1	-18.50	12.73	-2.31	-2.30	6.23	3.10	3.86
ss70d	-27.8	-48.9	-51.04	55.72	-2.26	-2.66	11.79	7.02	7.38
ss70e	-28.3	-49.6	-76.33	79.59	1.95	2.07	6.08	4.18	4.62
ss73a	-14.7	-41.9	-9.07	19.52	1.68	1.63	4.32	2.11	2.69
ss73b	-14.2	-41,8	-19.40	19.56	4.57	4.62	7.28	2.30	5.12
ss73c	-14.1	-41.7	-18.33	21.36	1.91	1.85	5.22	2.65	3.27
ss73d	-14.7	-41.8	-8.38	9.49	0.56	0.58	3.07	1.78	1.87
ss73e	-14.4	-41.3	-20.53	28.7	2.65	2.73	6.25	2.97	3.98
ss76a	-53.9	-71.9	-75.35	79.83	4.02	4.01	12.97	7.82	8.80
ss76b	-53.5	-72.9	-77.76	78.97	1.37	2.66	15.02	9.98	10,07
ss76c	-53.1	-72.5	-24.08	43.93	8.44	8.63	13.27	4.35	9.50
ss76d	-53.7	-71.5	-58.06	73.28	6.66	6.63	12.04	6.18	9.08
ss76e	-53.2	-71.8	-32.02	66.20	2.61	2.85	9.13	5.73	6.29
ex3p69	-11.5	-63.5	-25.05	2.91	-9.20	-9.06	12.25	2.43	9.52
ex5p67	5.0	-61.9	-23.19	27.07	4.16	4.27	8.38	3.61	5.51
ex6p74	-30.9	-64.9	-42.63	36.52	1.38	1.45	6.48	3.83	4.07
Average			-44.16	44.13	-0.37	-0.355	11.19	5,62	7,63

Table 2.12: Statistics for the height difference between SRTM and height patch data for South America. All height quantities are in meters. Latitude and longitude are approximated to the nearest tenth of a degree.

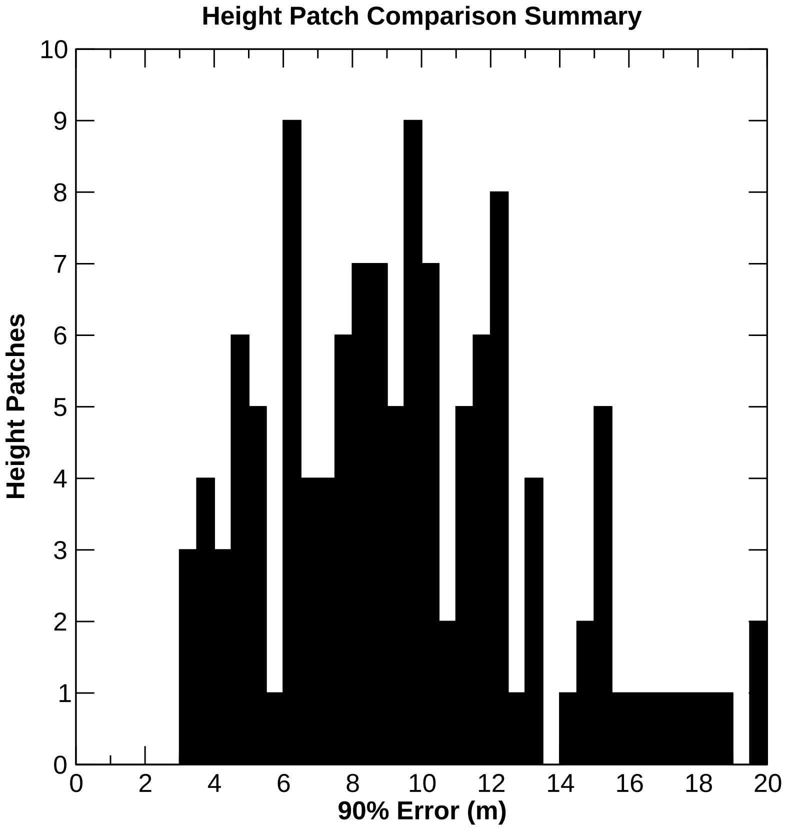

Figure 2.9: Histogram of the 90% error values for the comparison of the SRTM height data against the height patch data.

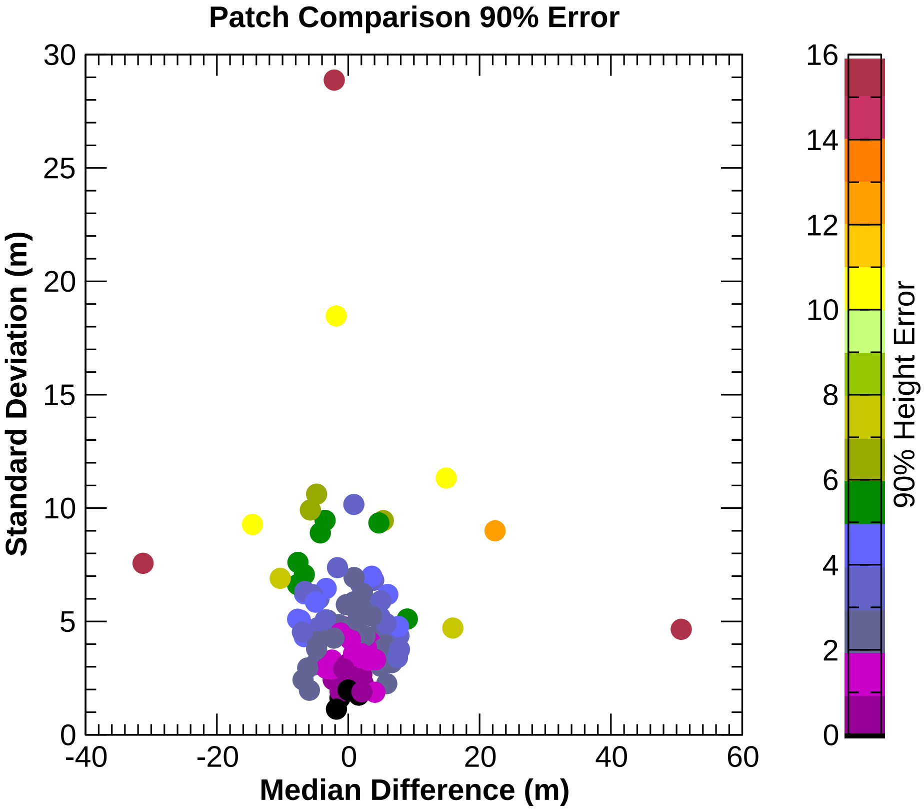

Figure 2.10: 90% Height errors plotted against height difference median and standard deviations for the SRTM to patch height data comparisons. Note that the largest differences are due to mean shifts in the two data sets, but there are a few data sets for which the difference is attributable to the within-cell RMS height difference.

2.4 Ocean and Land GCP Comparison

Even though the mosaic procedure uses the ocean and land GCPs for error reduction, the number of parameters estimated by the mosaicker (on the order of thousands) is much smaller than the number of ground control points (on the order of millions). Therefore, the post-fit residuals of the GCP data is still a valid measure of the instrument performance. In general, the ocean is darker than land, and we can expect higher random noise in the residuals. On the other hand, the slopes for the ocean are negligible, and slope induced errors will be minimized. The land GCPs used for this data set include a subset of the kinematic GPS GCPs, as well as a specially collected set of GCPs over Afghanistan, which is a region with extreme topography.

Table 2.13 summarizes the performance for each continent, while Figures 2.11–2.15 present the height error and error magnitude distribution functions. Notice that these results are consistent with those obtained using the kinematic GPS transects. For most of the data, the probability density function is well characterized by a Gaussian distribution, but for some continents (e.g., South America) a number of outliers exist which significantly deviate from a Gaussian distribution in the tails of the distribution.

Continent	Mean	Standard Deviation	90% Absolute Error
Africa	0.4	4.8	7.5
Australia	0.1	4.4	6.5
Eurasia	0.2	5.0	7.0
North America	-0.2	4.6	6.5
South America	0.0	5.1	6.5

Table 2.13: Summary of land and ocean GCP comparison with SRTM data. All quantities are in meters.

2.5 Land GCP Comparison

To examine further the deviation from Gaussian behavior, we separate the land only GCPs and recompute the histograms. The summary results are presented in Table 2.14 and in Figures 2.16–2.20. These results show that most of the outliers in the distribution do indeed come from the land GCPs. There is no mean shift in the bias, however, and the increase in 90% height error is due mainly to the increased proportion of outliers. The height error performance is still superior to that predicted by the height patches and by some of the DTED 2 cells.

Continent	Mean	Standard Deviation	90% Absolute Error
Africa	1.0	5.4	8.0
Australia	0.7	6.3	7.5
Eurasia	0.5	6.1	8.5
North America	-0.8	8.3	8.5
South America	-0.5	9.6	8.5

Table 2.14: Summary of land GCP comparison with SRTM data. All quantities are in meters.

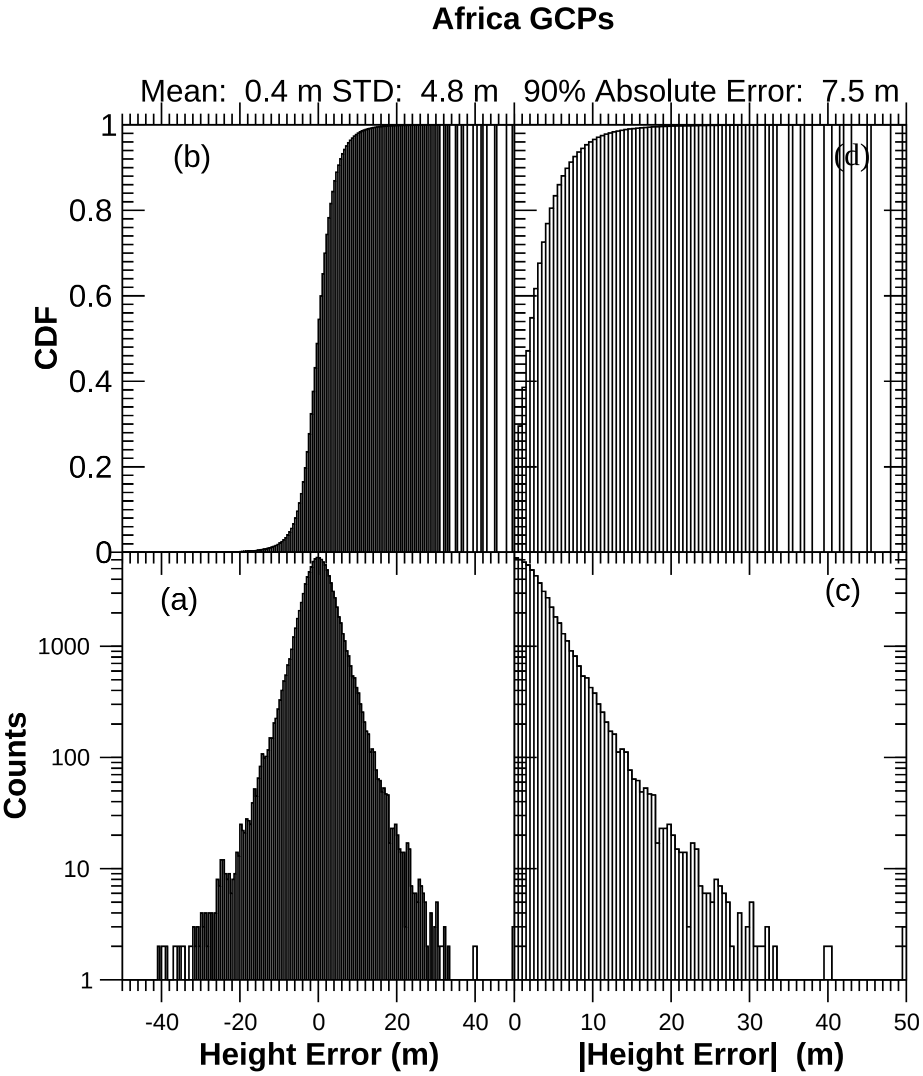

Figure 2.11: Africa ocean and land GCP height comparison. Panel (a) shows the distribution of the signed error; panel (b) the corresponding cummulative distribution function; panel (c) is the distribution of the error magnitude; and panel (d) is the cummulative distribution of the error magnitude.

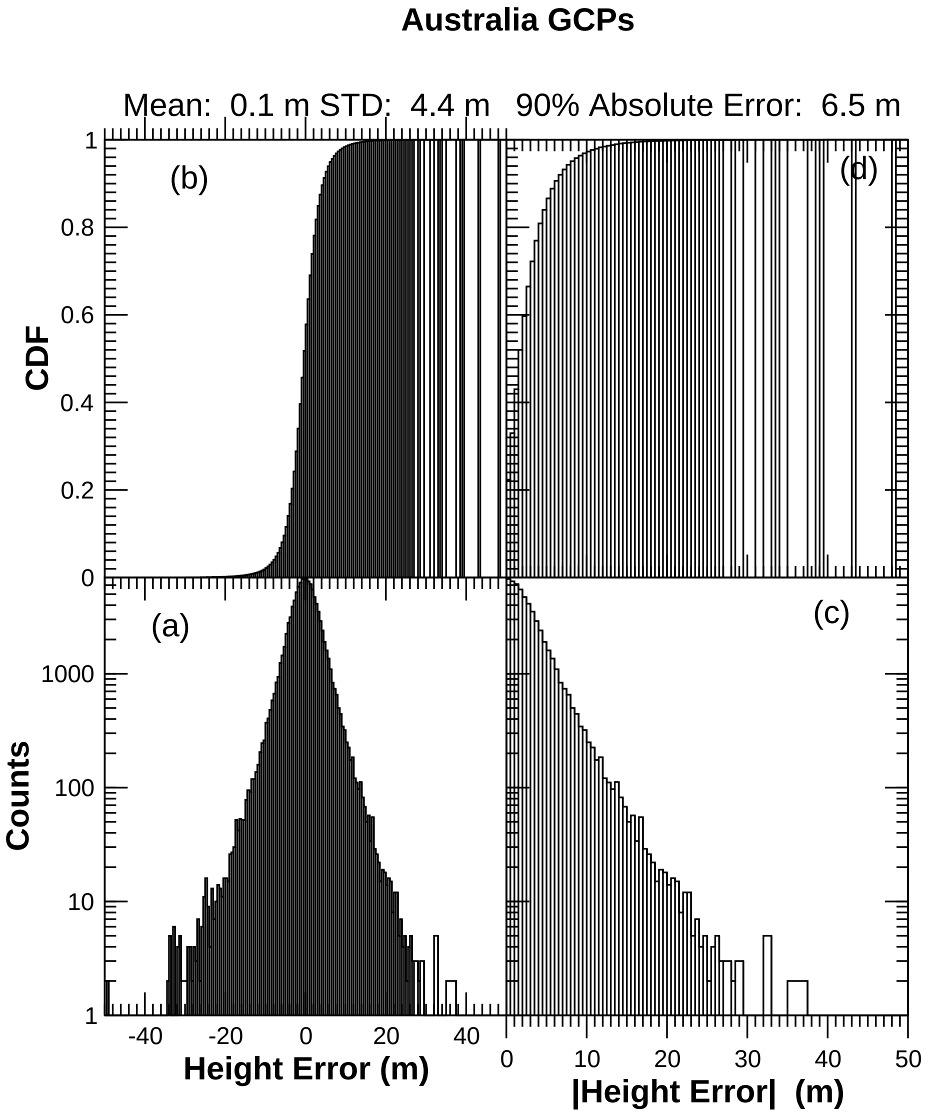

Figure 2.12: Australia ocean and land GCP height comparison. Panel (a) shows the distribution of the signed error; panel (b) the corresponding cummulative distribution function; panel (c) is the distribution of the error magnitude; and panel (d) is the cummulative distribution of the error magnitude.

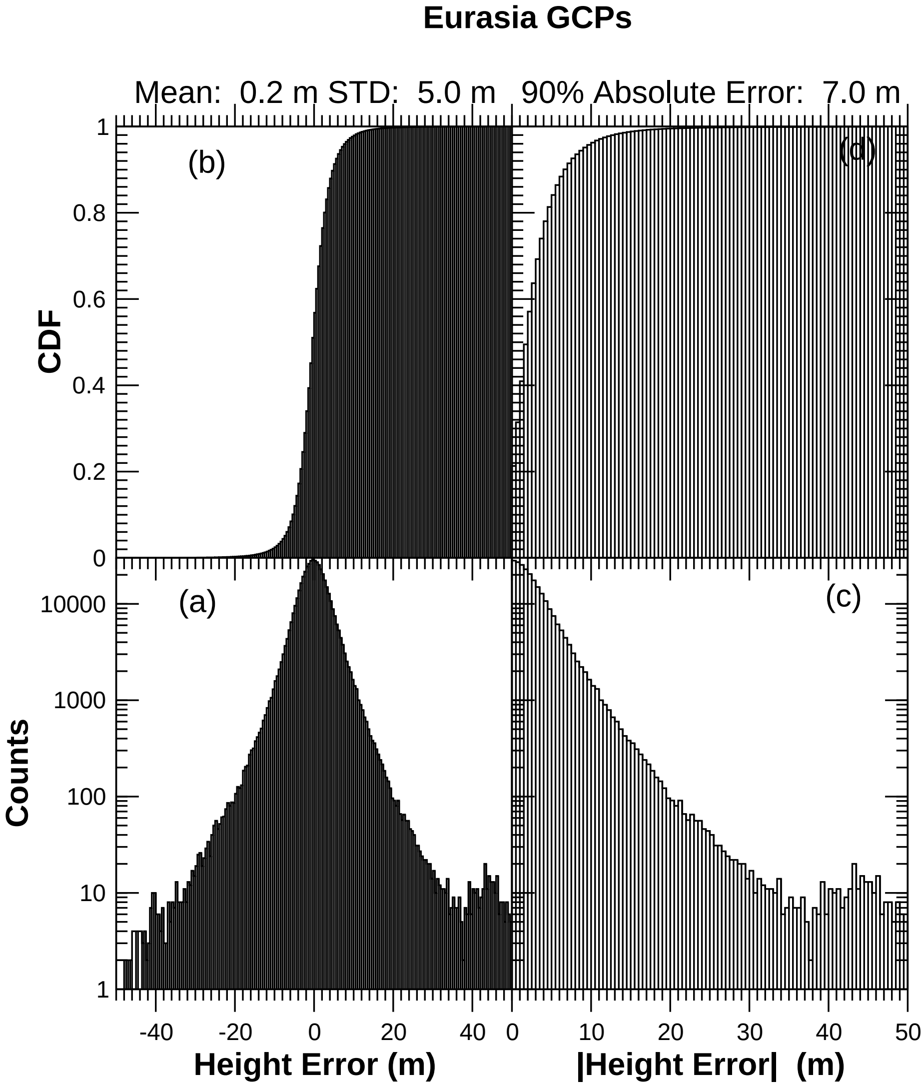

Figure 2.13: Eurasia ocean and land GCP height comparison. Panel (a) shows the distribution of the signed error; panel (b) the corresponding cummulative distribution function; panel (c) is the distribution of the error magnitude; and panel (d) is the cummulative distribution of the error magnitude.

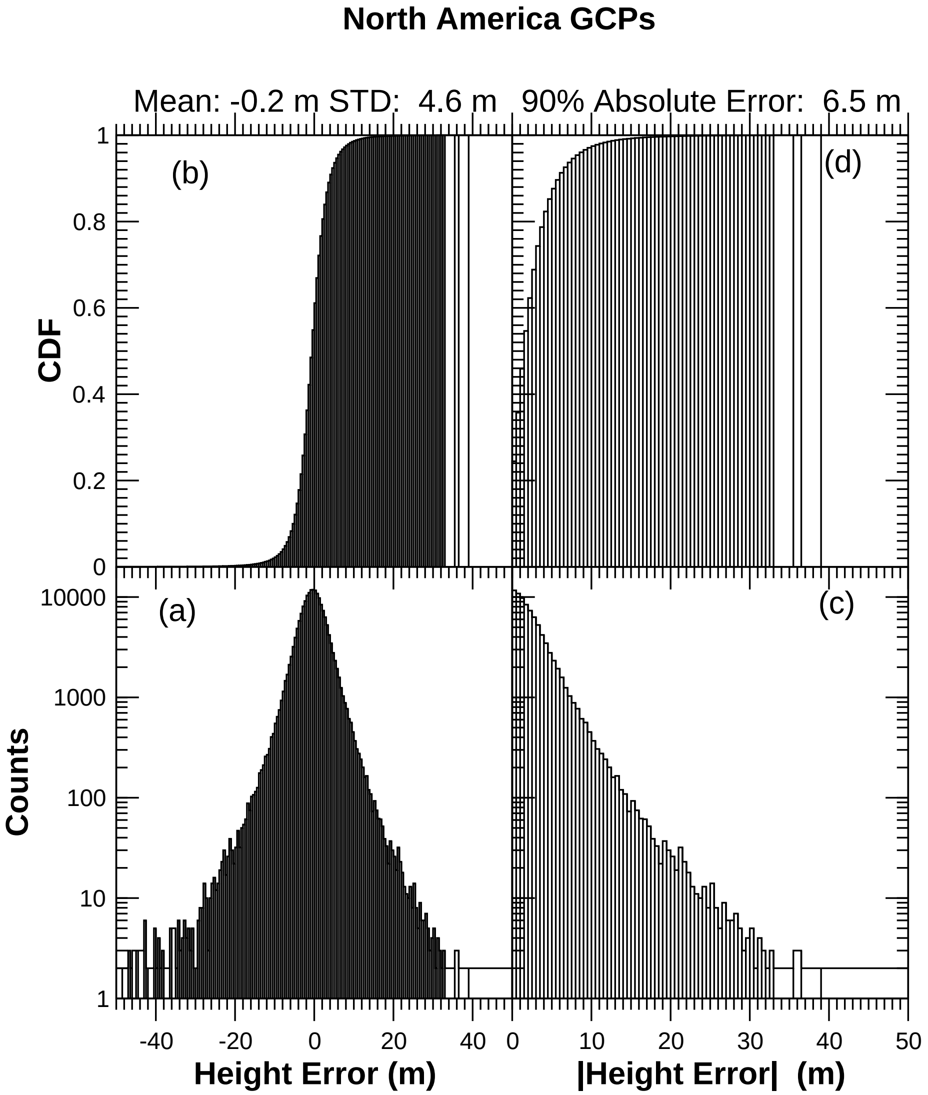

Figure 2.14: North America ocean and land GCP height comparison. Panel (a) shows the distribution of the signed error; panel (b) the corresponding cummulative distribution function; panel (c) is the distribution of the error magnitude; and panel (d) is the cummulative distribution of the error magnitude.

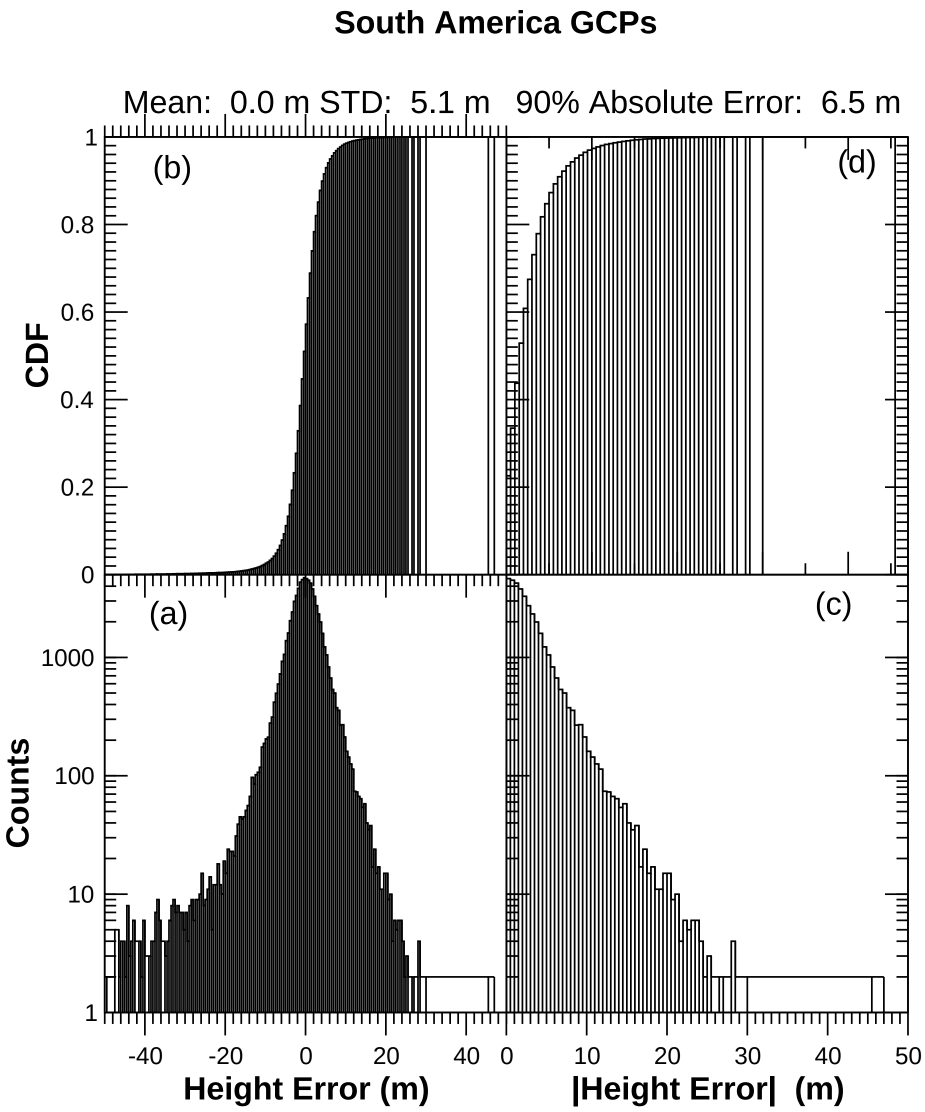

Figure 2.15: South America ocean and land GCP height comparison. Panel (a) shows the distribution of the signed error; panel (b) the corresponding cummulative distribution function; panel (c) is the distribution of the error magnitude; and panel (d) is the cummulative distribution of the error magnitude.

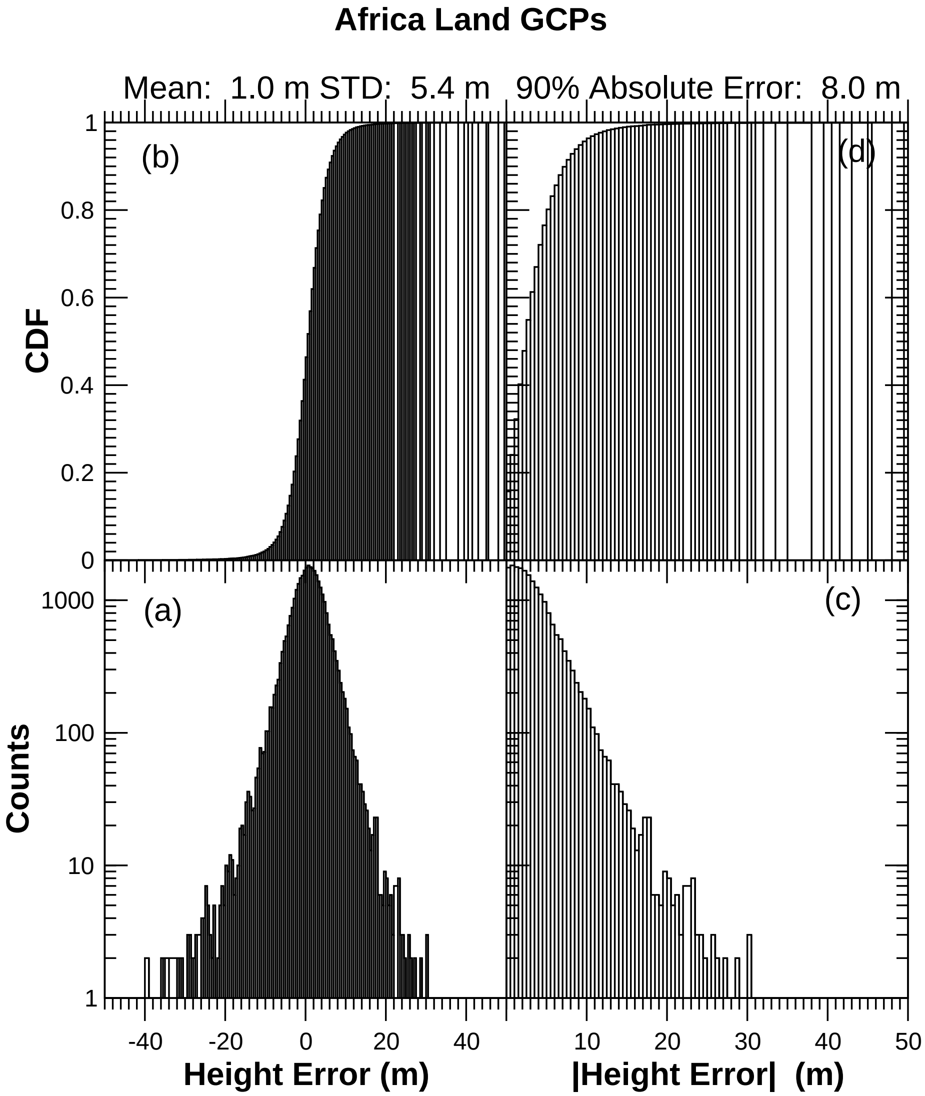

Figure 2.16: Africa land GCP height comparison. Panel (a) shows the distribution of the signed error; panel (b) the corresponding cummulative distribution function; panel (c) is the distribution of the error magnitude; and panel (d) is the cummulative distribution of the error magnitude.

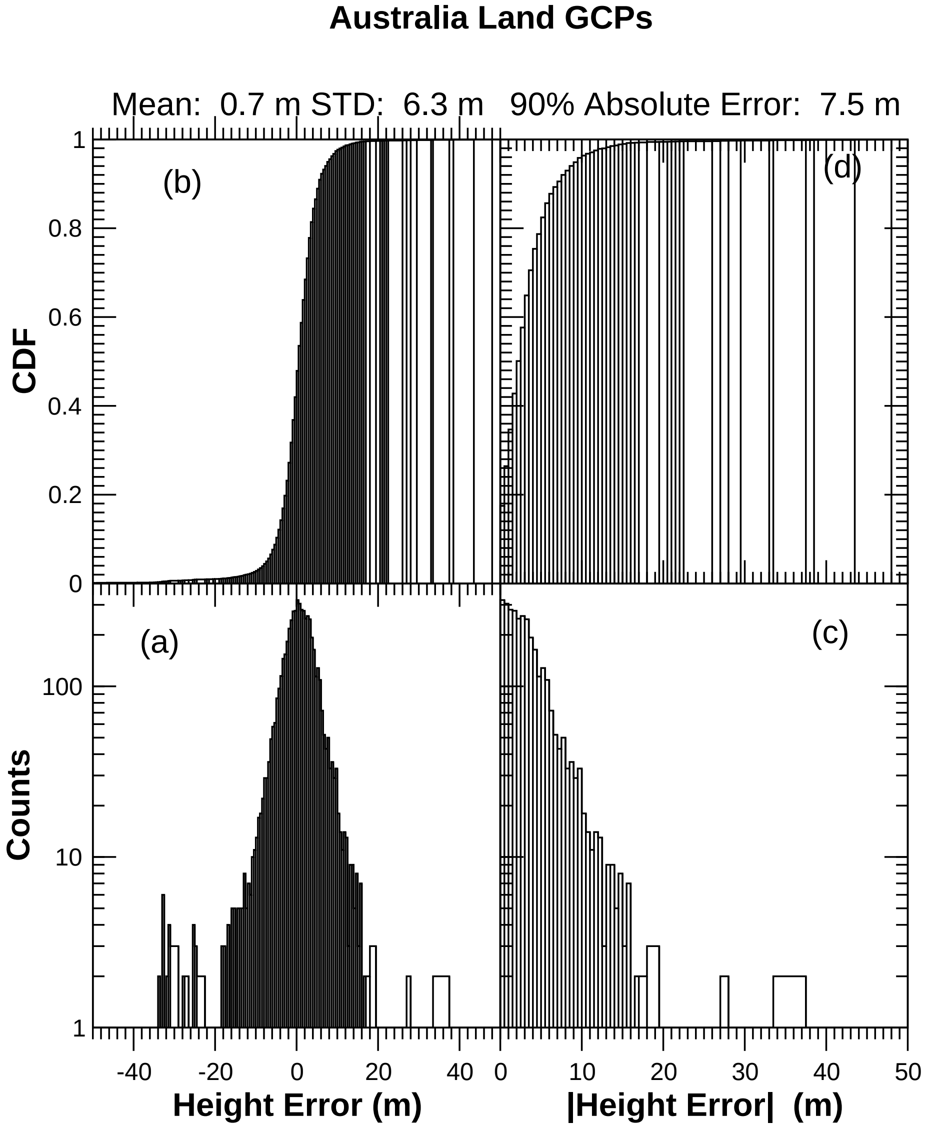

Figure 2.17: Australia land GCP height comparison. Panel (a) shows the distribution of the signed error; panel (b) the corresponding cummulative distribution function; panel (c) is the distribution of the error magnitude; and panel (d) is the cummulative distribution of the error magnitude.

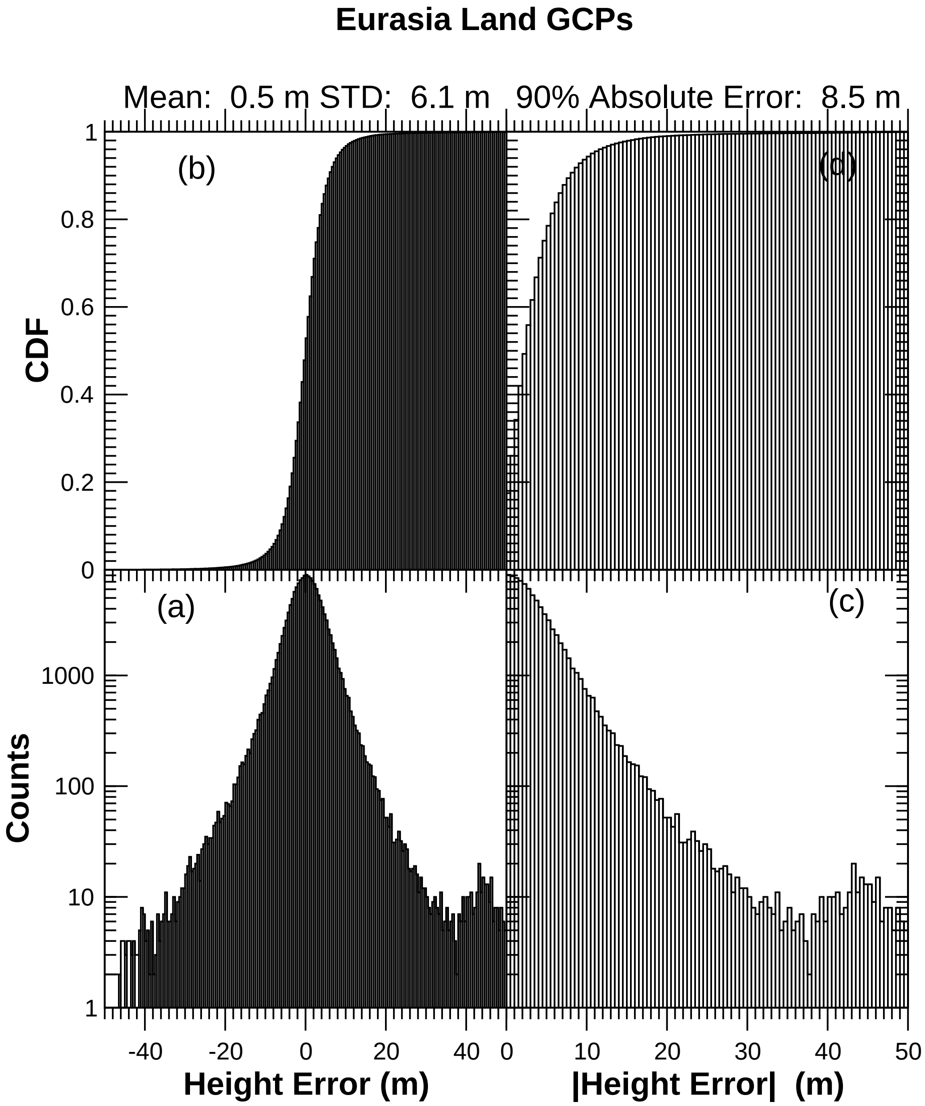

Figure 2.18: Eurasia land GCP height comparison. Panel (a) shows the distribution of the signed error; panel (b) the corresponding cummulative distribution function; panel (c) is the distribution of the error magnitude; and panel (d) is the cummulative distribution of the error magnitude.

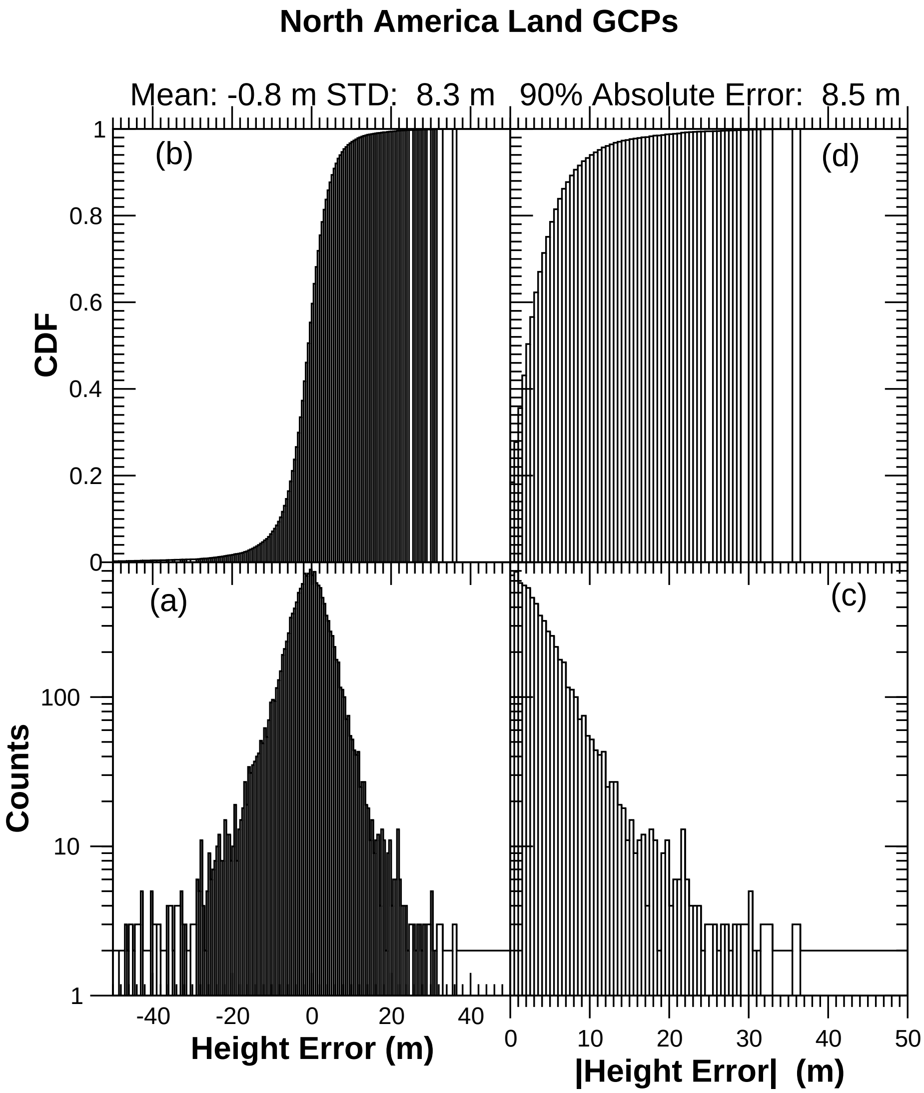

Figure 2.19: North America land GCP height comparison. Panel (a) shows the distribution of the signed error; panel (b) the corresponding cummulative distribution function; panel (c) is the distribution of the error magnitude; and panel (d) is the cummulative distribution of the error magnitude.

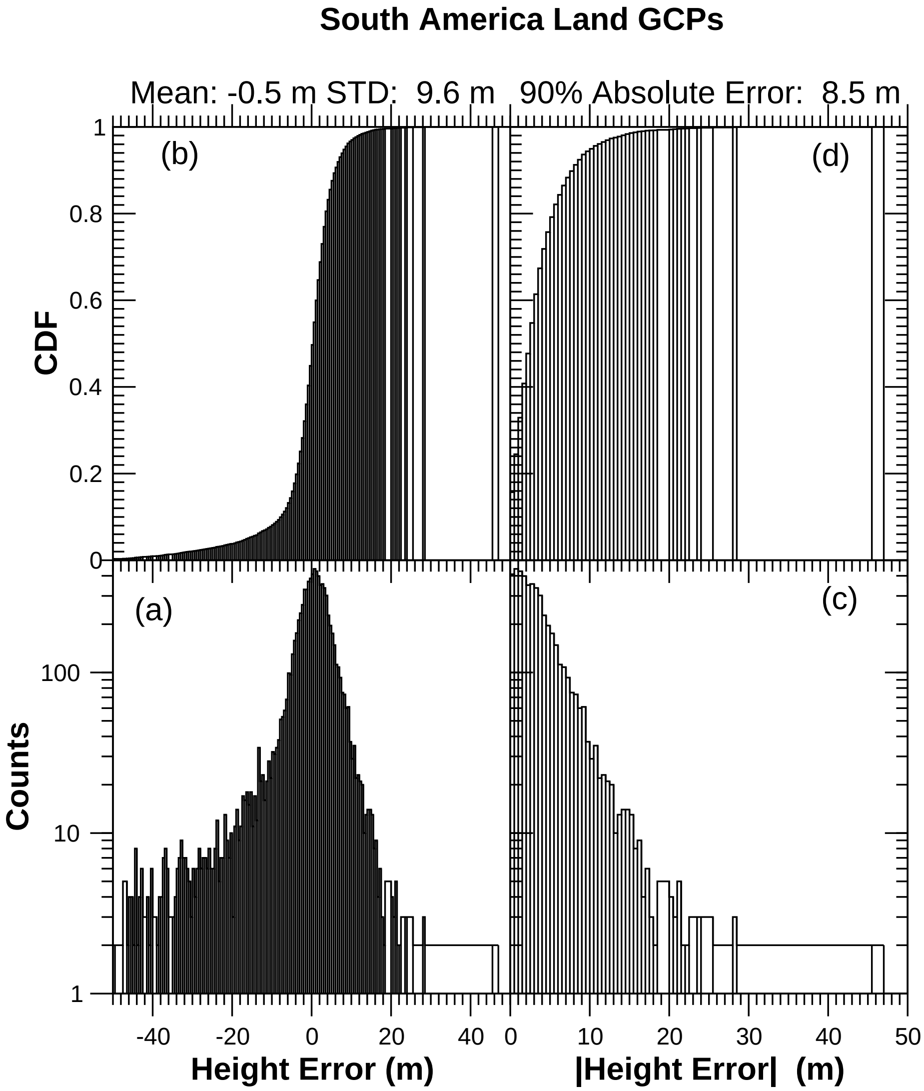

Figure 2.20: South America land GCP height comparison. Panel (a) shows the distribution of the signed error; panel (b) the corresponding cummulative distribution function; panel (c) is the distribution of the error magnitude; and panel (d) is the cummulative distribution of the error magnitude.

2.6 Absolute Height Error Conclusions

For all of the data sets examined, the SRTM data meets and exceeds the performance criteria, often by a factor of 2. There is a broad agreement between all the ground-truth data sources, but the largest deviations are exhibited by the height patches and some of the DTED 2 patches and land GCPs. Given the overall consistency in the mean error shown by the SRTM data, it is possible that the mean shifts between the data sets are not due to SRTM.

Chapter 3

Spatial Structure of the SRTM Errors

3.1 Long-Wavelength Error Characteristics from Kinematic GPS Transects

In order to separate long-wavelength errors from topographic errors, we average the SRTM errors relative to the kinematic GPS data using 0.5° boxcar low-pass filters (i.e., for any given latitude and longitude, all the differences of SRTM height minus the KGPS height within 0.25° degrees of latitude or longitude of the desired point are averaged). The resulting average errors for the different continents are shown in Figures 3.1–3.6.

Examination of these figures shows that the average errors have coherent long-wavelength signatures which can vary significantly over a continent. These errors are consistent with residual motion errors. There seems to no apparent correlation of the error to the underlying topography, or a preferred scale or direction of the error which persists across continents. The fact that the kinematic GPS data is essentially unbiased relative to SRTM show that the mosaicker has removed the mean long-wavelength error over the continent. The magnitude of the error is on the order of ~ 2 m. These errors are consistent with the error model introduced in Section 1.5.

3.2 Long-Wavelength Error Characteristics from Land and Ocean GCPs

To further visualize the nature of the long wavelength errors, we apply the same 0.5° boxcar low-pass smoothing filter as in section 3.1 to the land and ocean GCP residuals after the mosaic corrections. The results are presented in Figures 3.7–3.10 and Figure 1.5.

What these figures show is that, after mosaic corrections, there are no detectable residual tilts over the continents, there are still some detectable residual long-wavelength modulations over the water, although their magnitude is small. The magnitude of the long wavelength error then grows as the distance from the coast increases. The pre-eminent example of this behavior is the residual

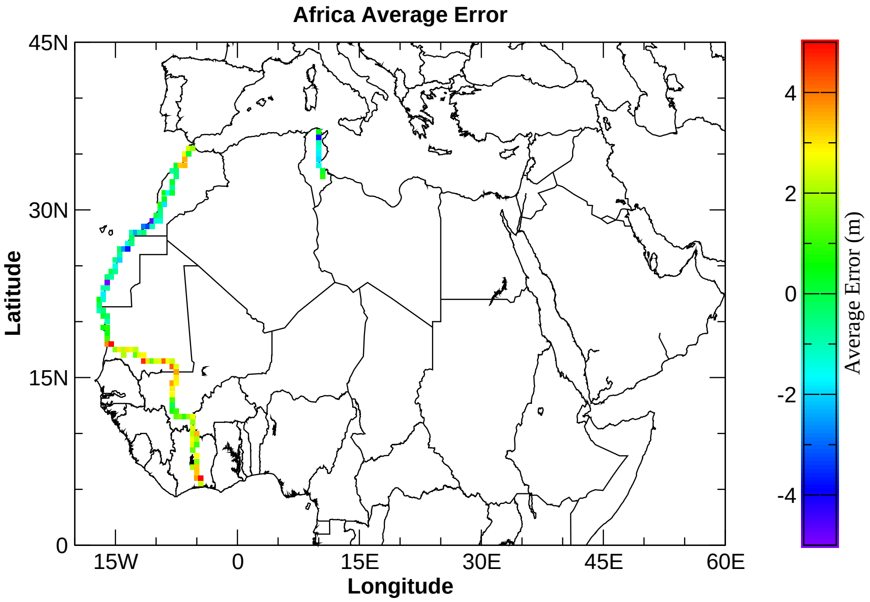

Figure 3.1: SRTM minus kinematic GPS height differences averaged over 0.5° of latitude and longitude for Africa.

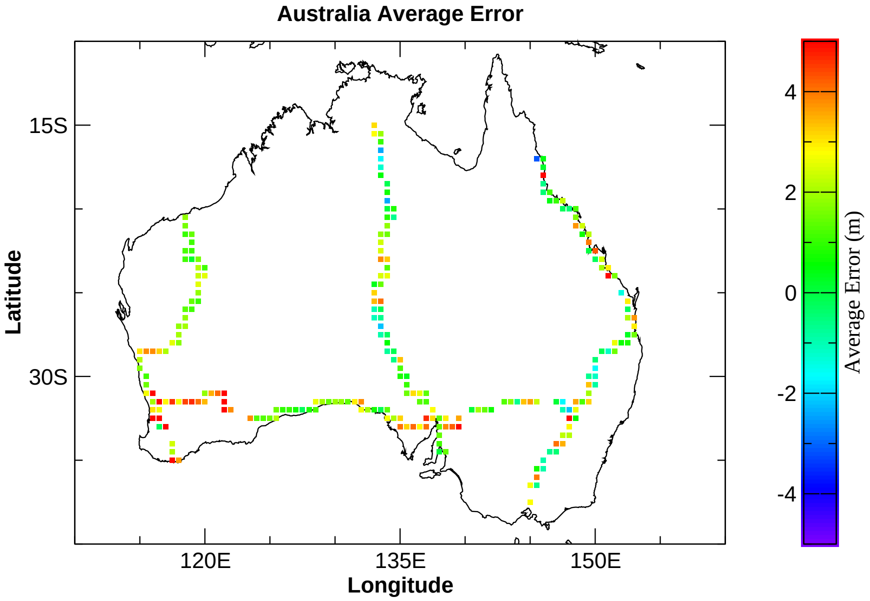

Figure 3.2: SRTM minus kinematic GPS height differences averaged over 0.5° of latitude and longitude for Australia.

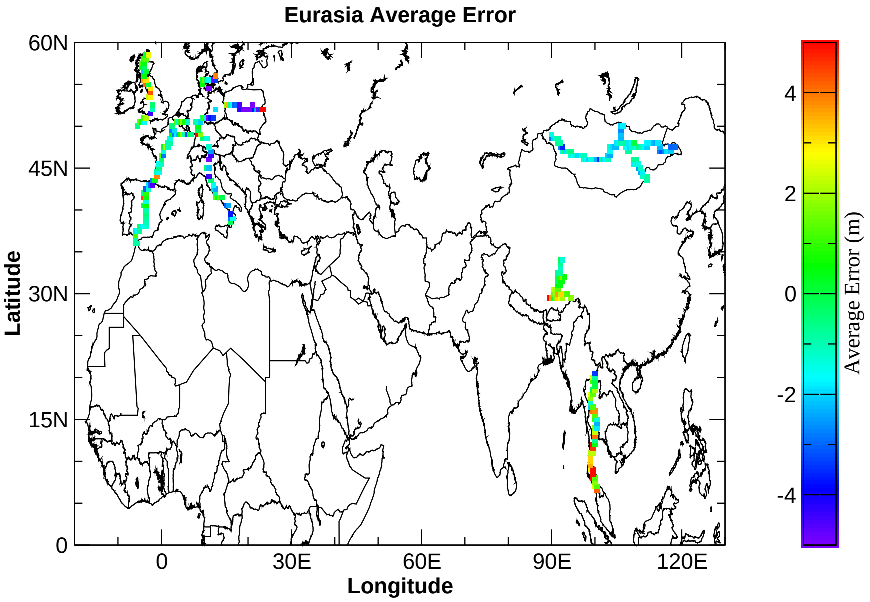

Figure 3.3: SRTM minus kinematic GPS height differences averaged over 0.5° of latitude and longitude for Eurasia.

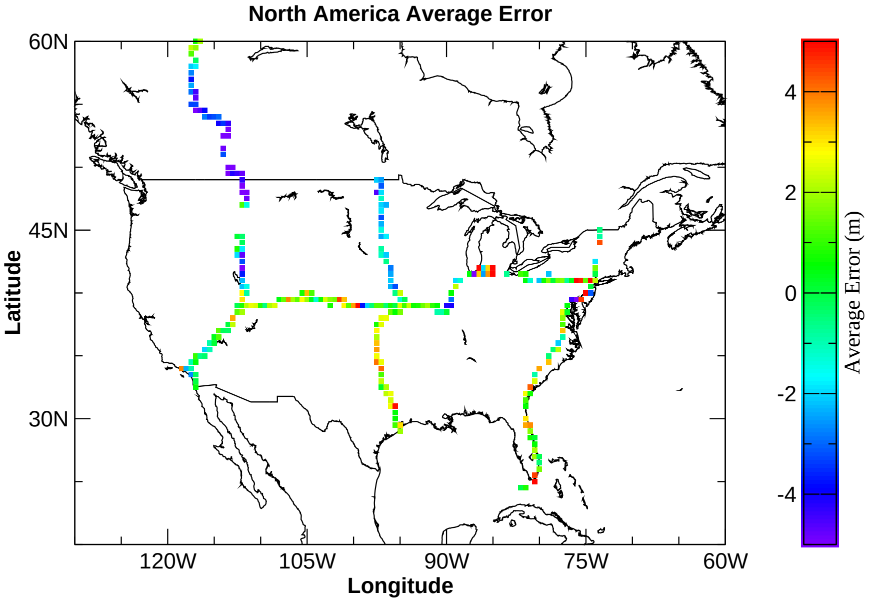

Figure 3.4: SRTM minus kinematic GPS height differences averaged over 0.5° of latitude and longitude for North America.

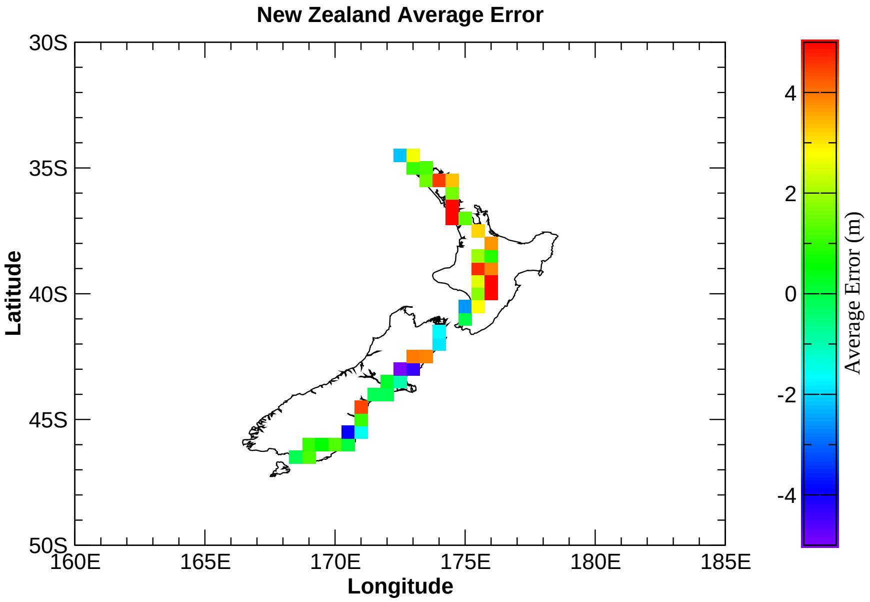

Figure 3.5: SRTM minus kinematic GPS height differences averaged over 0.5° of latitude and longitude for New Zealand.

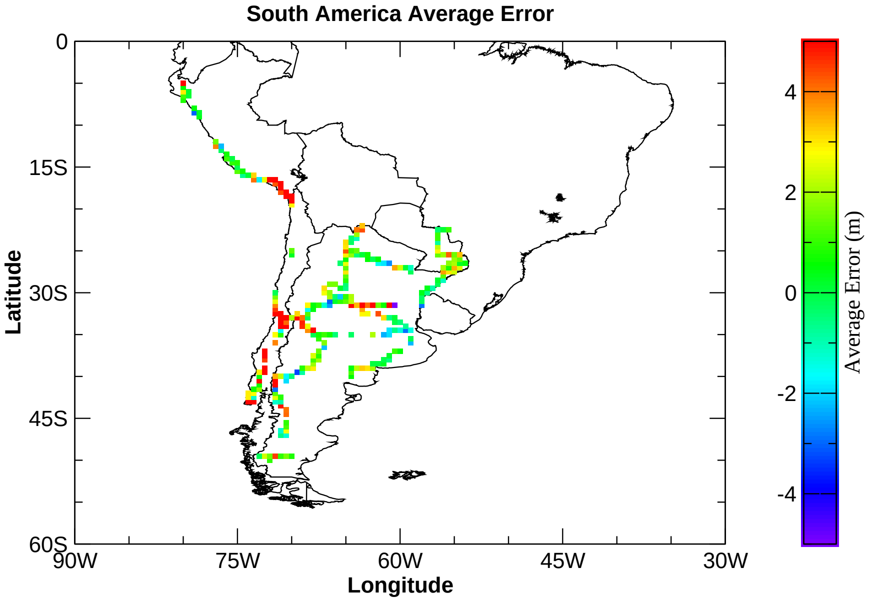

Figure 3.6: SRTM minus kinematic GPS height differences averaged over 0.5° of latitude and longitude for South America.

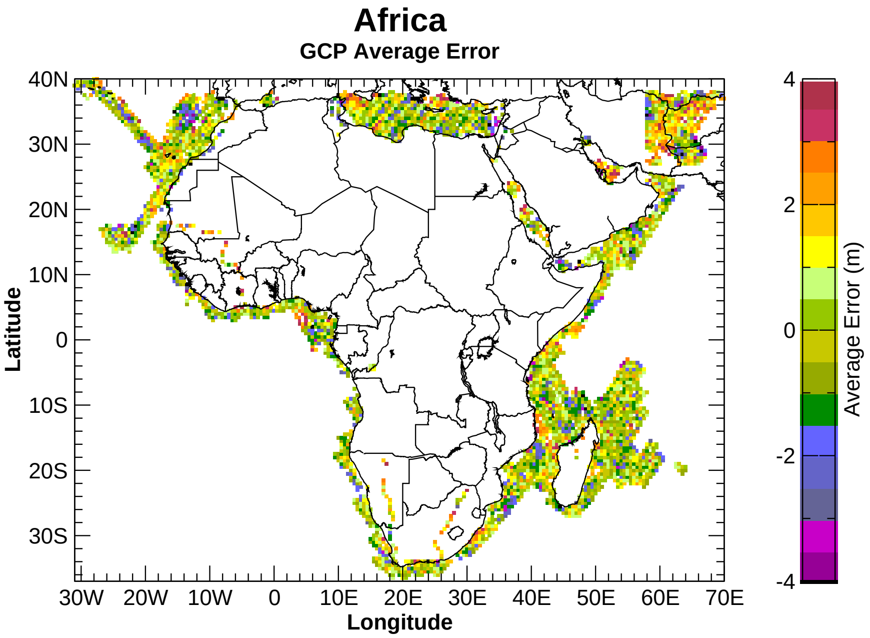

Figure 3.7: Africa residual long-wavelength errors for land and ocean GCPs after mosaic corrections are applied.

GCPs in Central Asia which can be seen in Figure 1.5. One can also notice in these figures that GCP outliers (black) tend to occur in isolated points.

3.3 The Height Error Structure and Correlation Functions

To study the spatial characteristics of the error, we compute the structure function (Equation 1.1) for the height error along the kinematic GPS tracks. The results are shown in Figures 3.11–3.15.

These results show that, when averaged over an entire continent, the structure function can either approach an asymptotic value (South America), show a slightly increasing trend with separation (North America, Australia), or show non-stationary behavior (Africa and Eurasia). These results show the presence of long-wavelength errors which can be coherent over continental scales, as one would expect for residual motion errors. On the other hand, even though fluctuations and long wavelength correlations exist, the magnitude of the relative RMS error is almost always smaller than 6 m, which corresponds to a relative 90% height error of about 10 m, which is the measurement requirement for SRTM.

To study the short-wavelength behavior of the error, we compute the height error correlation function using Equation 1.2. Figure 3.16 presents the behavior of the correlation function on separation scales from 0 to 400 km, or about twice the SRTM swath. The generic behavior is the same for all continents: a rapid decrease from a peak value followed by a plateau of correlation. Three continents (South America, North America, and Africa) exhibit almost identical behavior, although their structure function differs at larger scales. Australia and Eurasia show significantly

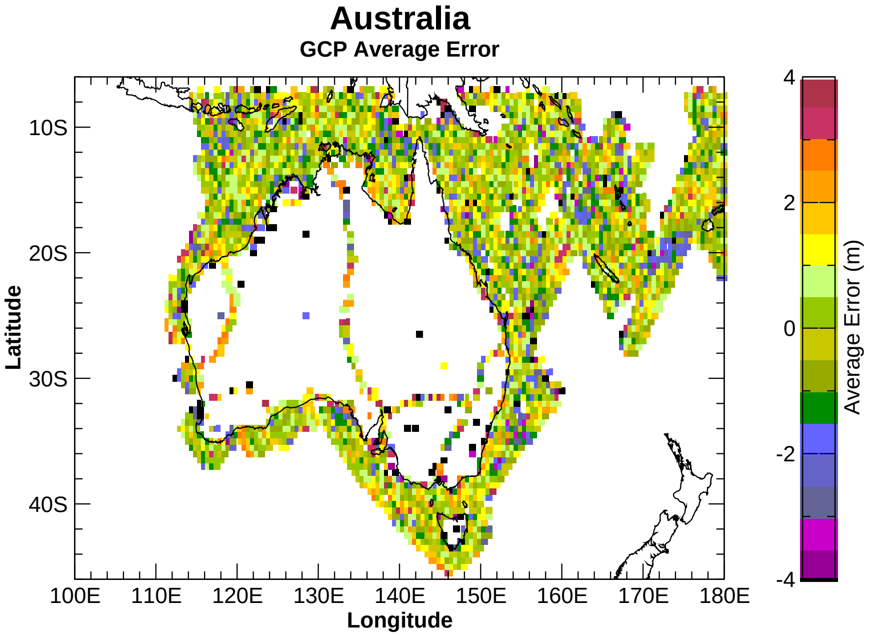

Figure 3.8: Australia residual long-wavelength errors for land and ocean GCPs after mosaic corrections are applied.

higher correlation plateaus. This is probably due to the fact that, since the kinematic GPS tracks were collected over flatter regions, the long wavelength error component makes up a larger fraction of the total error compared to regions which have greater topography. The results over New Zealand can be similarly explained as being caused by large topographic variations. However, more work needs to be done to verify these conjectures.

All of the correlation functions exhibit a very similar behavior near the origin. To study the further, Figure 3.17 presents a zoom of the previous figure around the origin. It is clear from this figure that in all cases, the correlation drops from its peak value of 1 at the origin to the plateau region for separations greater than approximately 100 m–200 m, while significant correlations are still apparent for separations of 50 m. This is consistent with the SRTM spatial averaging scheme, which applied a three pixel boxcar filter ($\sim$ 45 m correlation length) to reduce speckle noise.

Although the previous figures present the average behavior for a continent, it should be remembered that the short-wavelength behavior within a continent will show variability reflecting the local random errors. Figure 3.18 shows the variability in the short wavelength structure function for nearby kinematic GPS tracks which were processed as part of the same least squares adjustment. As can be seen, significant variability in the short wavelength behavior is present due to changes in the local conditions.

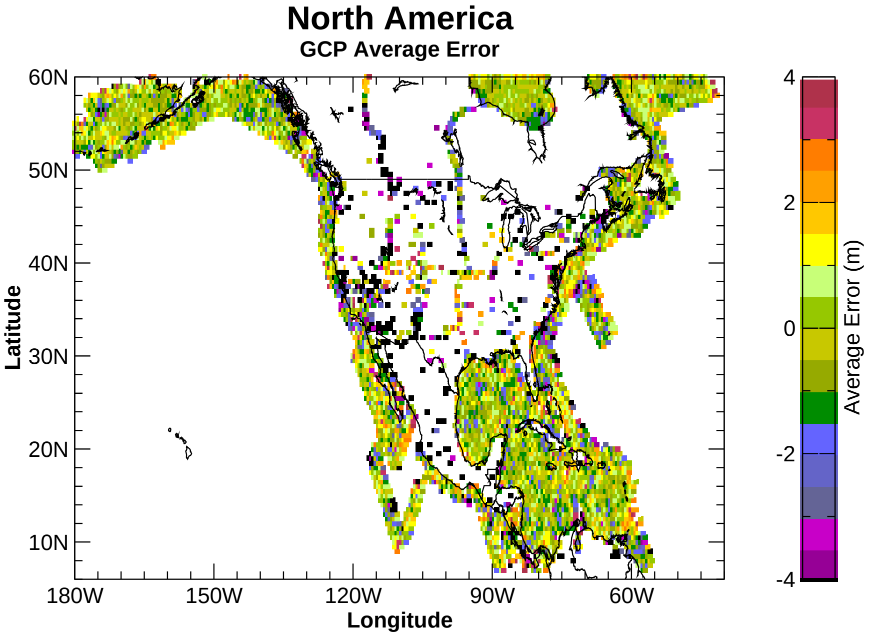

Figure 3.9: North America residual long-wavelength errors for land and ocean GCPs after mosaic corrections are applied.

3.4 Spatial Structure Conclusions

The SRTM error can be thought of as consisting of three parts: first, a long wavelength component, due to residual roll errors, with a magnitude of about 2 m and a spatially non-stationary behavior. The second component consists of random (i.e., medium to short wavelength) errors which add an additional spatially varying error component. Finally, at the shortest scales, speckle noise decorrelates for separations on the order of one to two pixels. The next chapter examines the nature of the random error in greater detail.

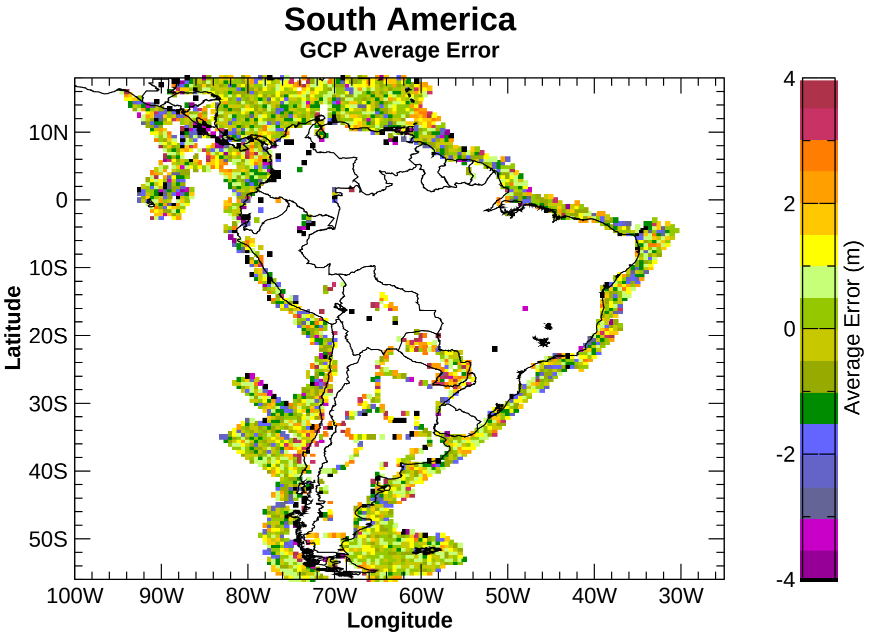

Figure 3.10: South America residual long-wavelength errors for land and ocean GCPs after mosaic corrections are applied.

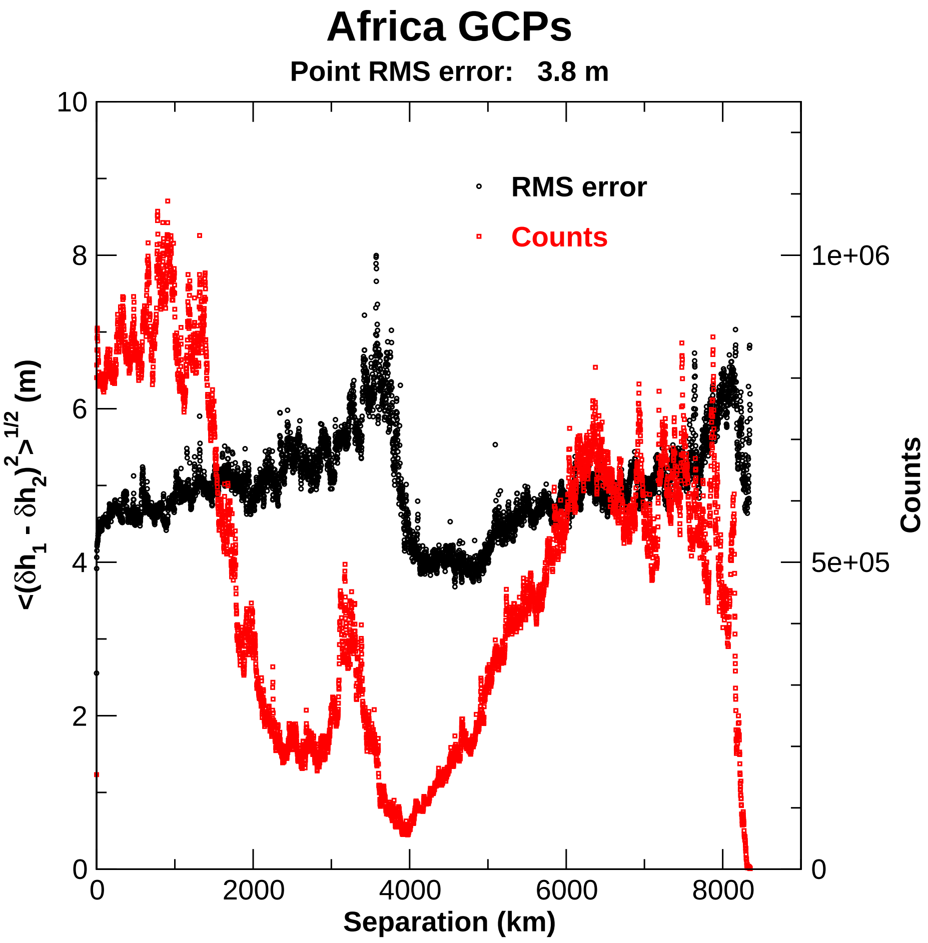

Figure 3.11: Structure function for the Kinematic GPS GCP errors for Africa (black, left axis) and number of points used in the estimate (red, right axis). The RMS height error computed using all points is 3.8 m.

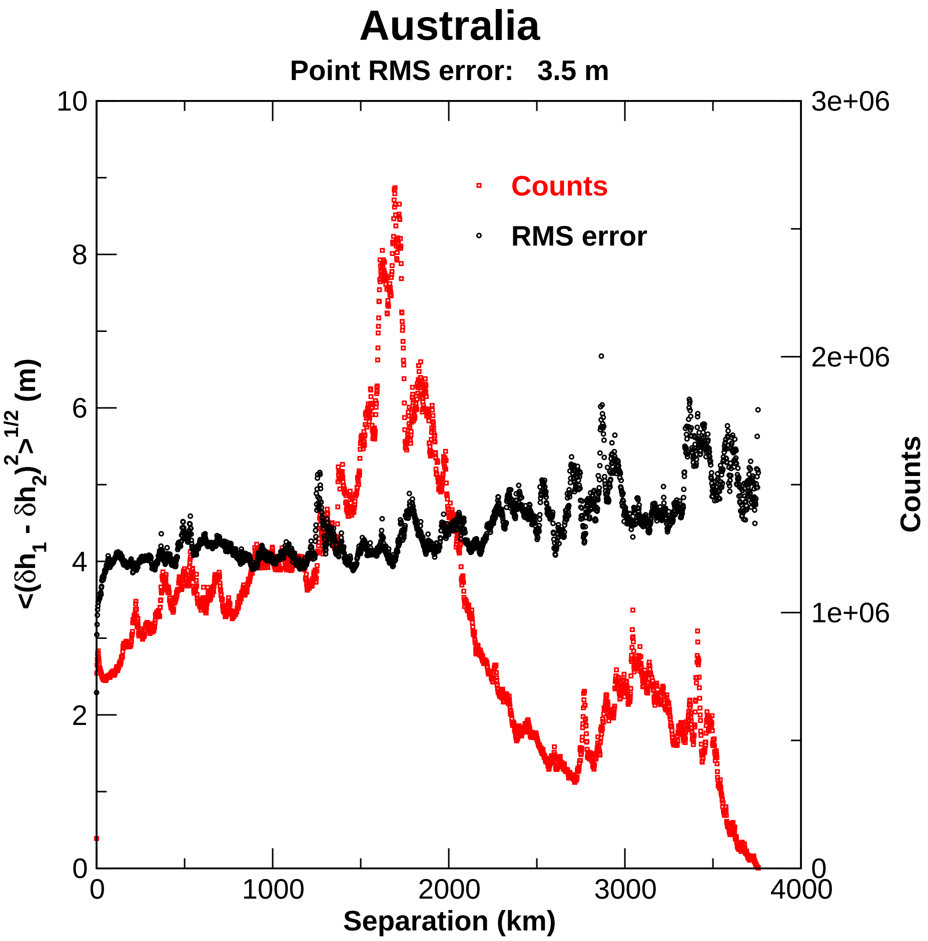

Figure 3.12: Structure function for the Kinematic GPS GCP errors for Australia (black, left axis) and number of points used in the estimate (red, right axis). The RMS height error computed using all points is 3.5 m.

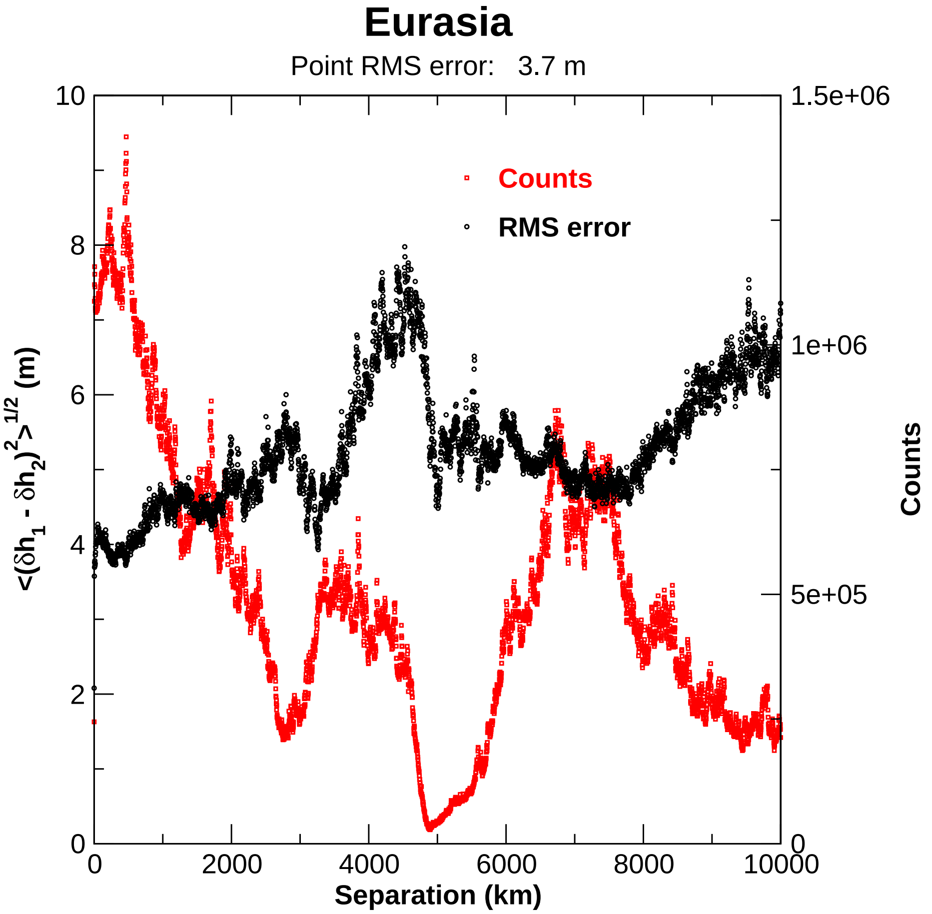

Figure 3.13: Structure function for the Kinematic GPS GCP errors for Eurasia (black, left axis) and number of points used in the estimate (red, right axis). The RMS height error computed using all points is 3.7 m.The different domains are caused by a different mean error in Malaysia.

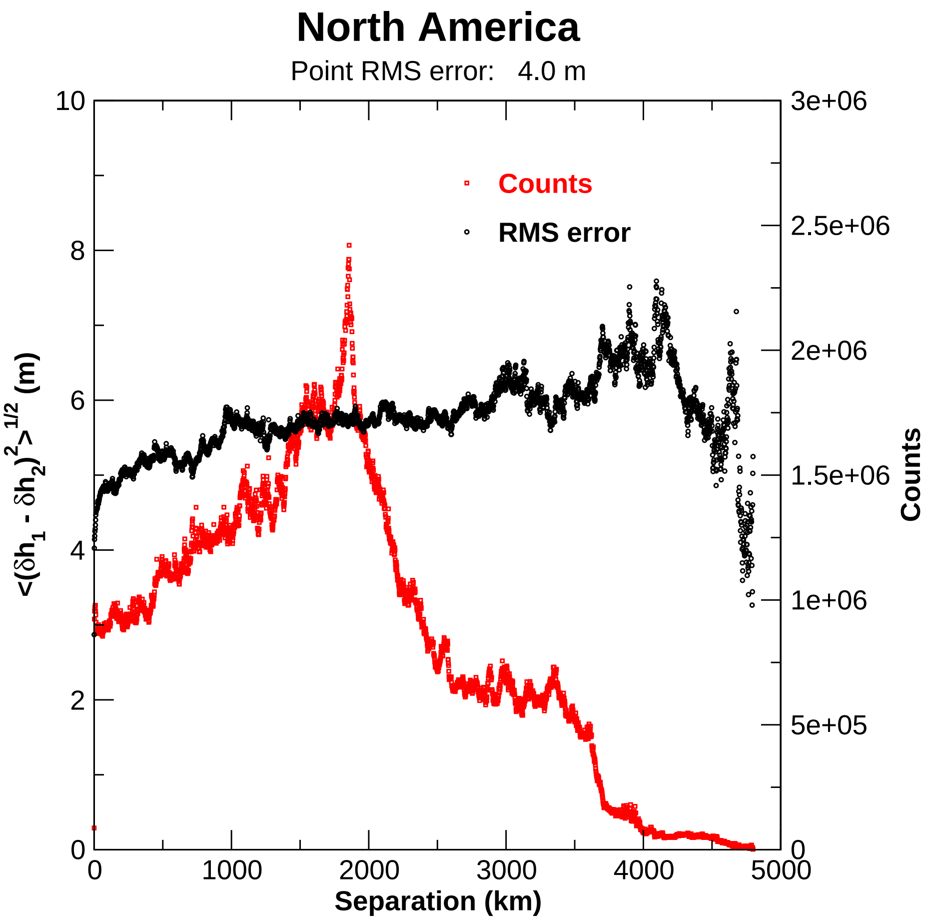

Figure 3.14: Structure function for the Kinematic GPS GCP errors for North America (black, left axis) and number of points used in the estimate (red, right axis). The RMS height error computed using all points is 4.0 m.

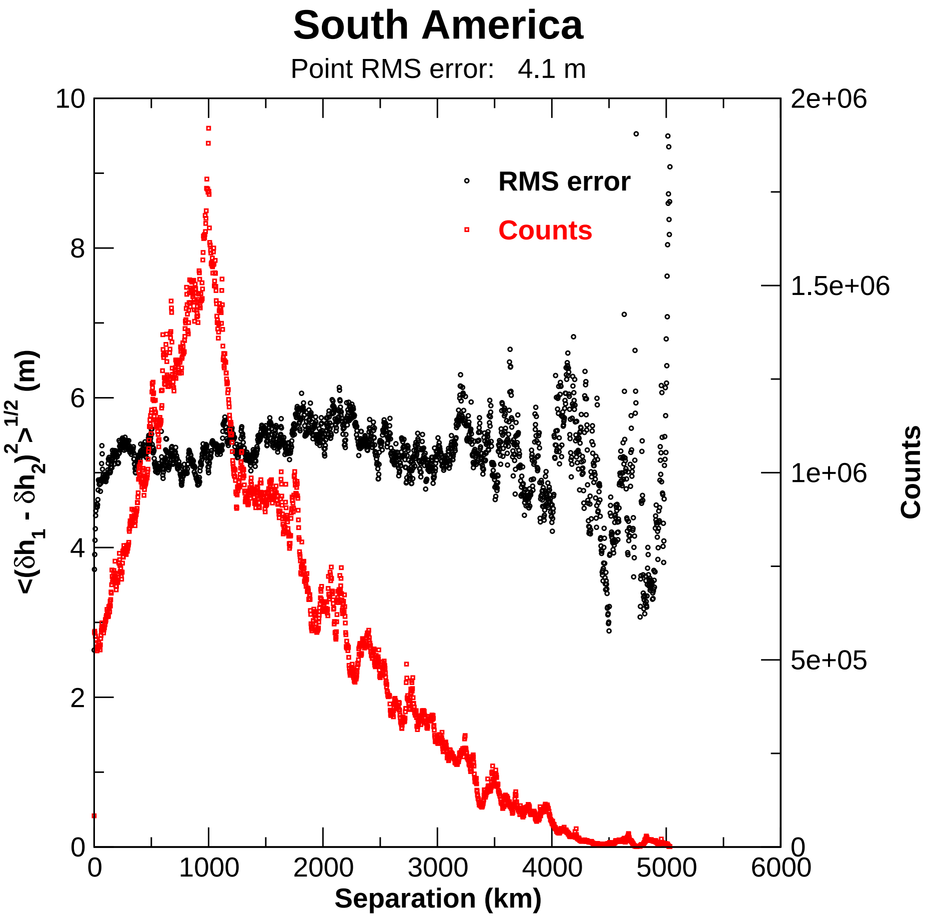

Figure 3.15: Structure function for the Kinematic GPS GCP errors for South America (black, left axis) and number of points used in the estimate (red, right axis). The RMS height error computed using all points is 4.1 m.

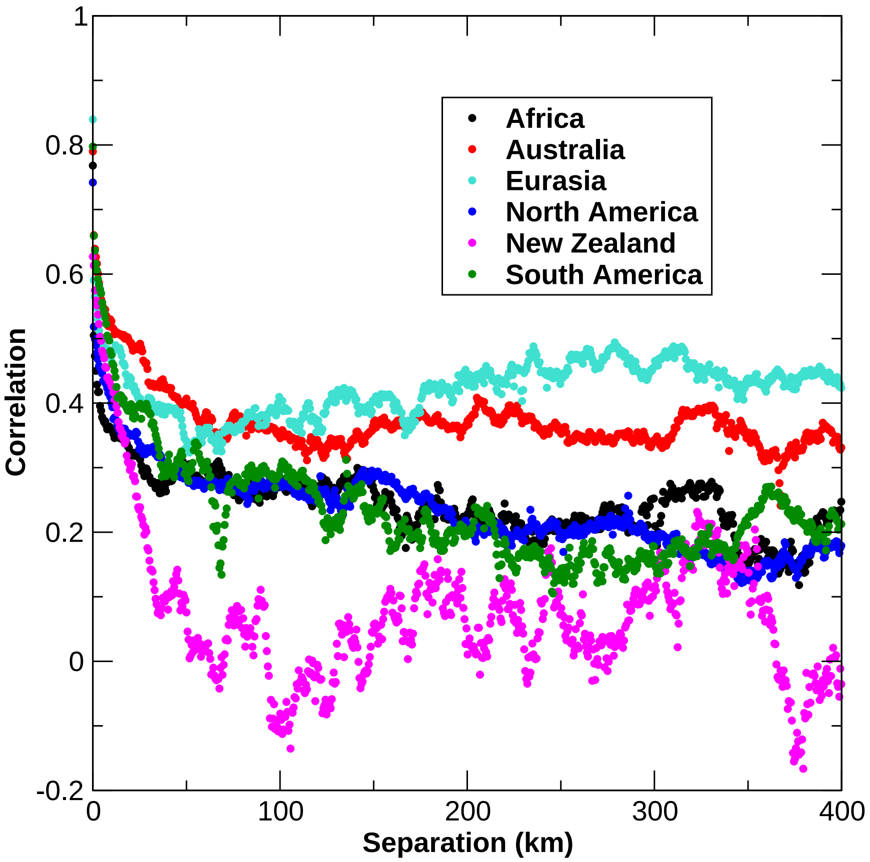

Figure 3.16: Correlation function for all continents over the scale of two SRTM swaths.

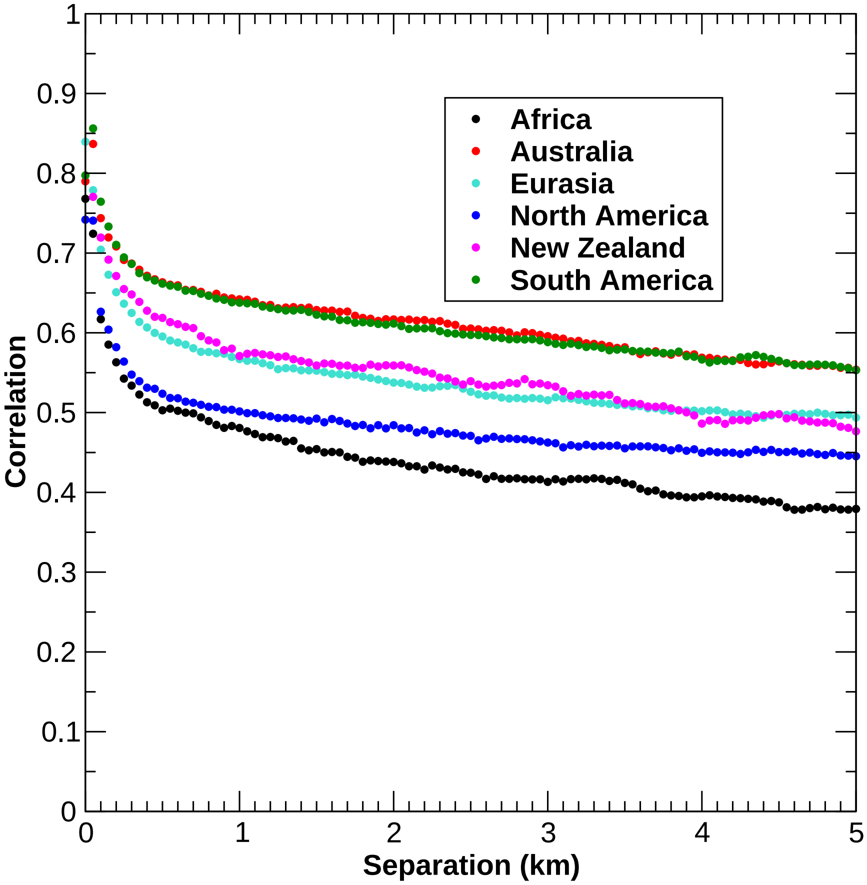

Figure 3.17: Zoom on the correlation function presented in Figure 3.16 for small distances from the origin.

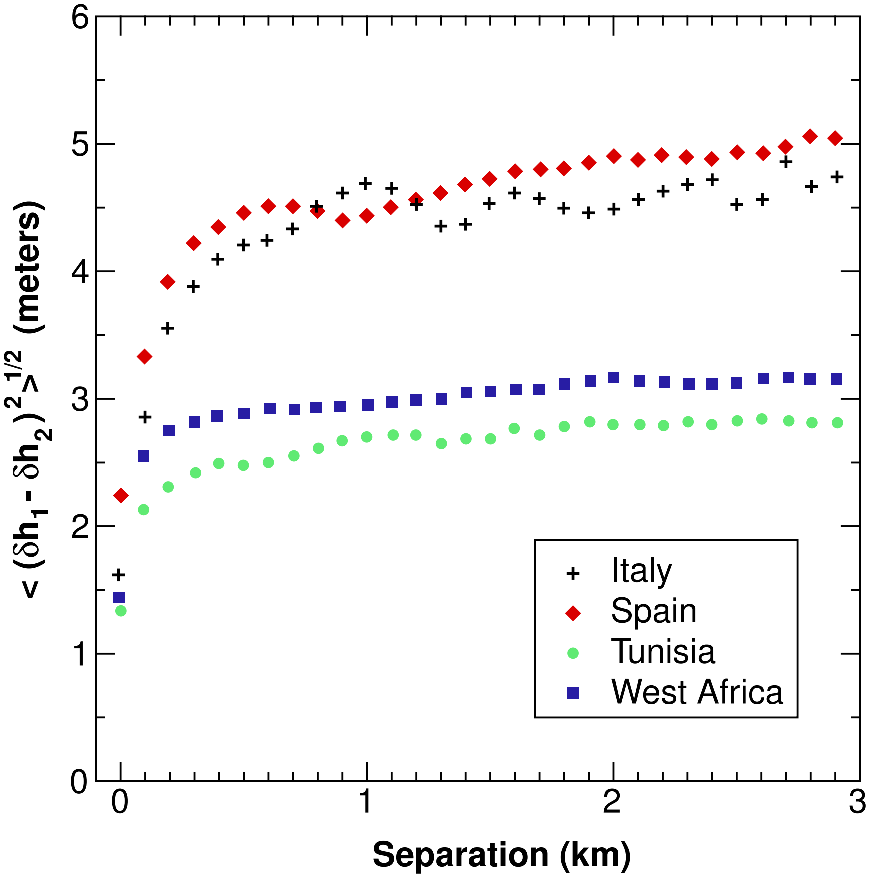

Figure 3.18: Variability of the structure function for different kinematic GPS tracks.

Chapter 4

Random Errors and the Terrain Height Error Data (THED)

4.1 Validation of THED from DTED Level-2 Comparisons

Random errors (i.e., zero-mean errors with very short spatial correlation lengths) are caused by instrument thermal noise and geometric decorrelation effects [5] [6]. The geometric decorrelation can be compensated suitable spectral filtering, at a loss in resolution, as proposed by Gatelli et al. [7]. For SRTM, spectral filtering was applied based on a flat reference surface, which left residual decorrelation for non-zero slopes.

Once the channel-to-channel correlation, γ, is estimated from the radar interferogram, the interferometric phase error can be computed by means of the equation

$$\delta\Phi = \frac{1}{\sqrt{2N_L}} \frac{\sqrt{1-\gamma^2}}{\gamma} \tag{4.1}$$

where N_L is the number of independent radar realizations, or "looks". In Appendix A, we describe in detail how the height error can be obtained from the phase error (see equation A.46). Special care must be taken when counting the number of looks since the looks used in forming the interferogram can be correlated [8]. The theoretical estimates obtained by using this process were made into the "Terrain Height Error Data" product delivered by JPL to NIMA.

To validate the the theoretical predictions we estimated the true, high frequency, random error by high passing the difference between known topography and the SRTM estimate. The high-pass filter was implemented by selecting a box size, removing a mean error plane by comparing against DTED Level-2 ground truth, and computing the root mean squared (RMS) of the residual. The selection of the optimal box size is governed by two factors: first, if the box is too small, equation 1.10 predicts that the error will be underestimated due to the correlation properties of the random error discussed in the previous chapter. On the other hand, if the box is too large, the topography will start to alias into the signal. After some experimentation, it was found that an average box size of 11 pixels represented a suitable compromise between these two criteria.

Figure 4.2 shows an example of the estimated random error for the topography around 29 Palms, California, shown in Figure 4.1. The greatest errors are associated with regions of higher relief, but also with regions of reduced radar brightness. Figure 4.3 shows the computed THED values computed from the correlation after scaling for the effective number if looks.. The correlation between the two images is apparent, although the THED seems to underestimate the measured errors for large errors (or low correlation).

In order to formalize this relationship, we used 22 of the DTED 2 cells and repeated the procedure outlined above. The results of the comparisons are shown in Figure 4.4. There is a tight correlation between the two data sets, with a small deviation at the higher error values. This underestimate of the error may be due to the high-pass filtering process aliasing or biases in the estimation of correlation for low correlation values. However, for the bulk of the data, the correlation is quite good. The results presented in Figure 4.4 validate the accuracy of the SRTM THED using globally distributed DTED 2 data with about 31 million observations.

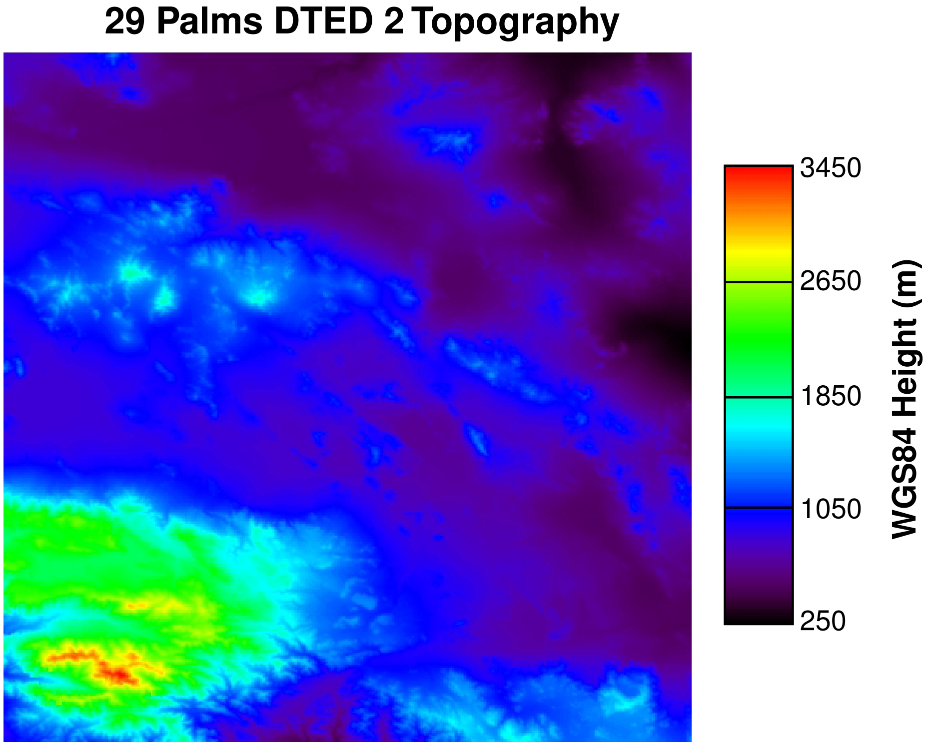

Figure 4.1: Topography for the 29 Palms DTED 2 cell used to illustrate random errors

4.2 Global Random and Absolute Error Performance

Given the THED values generated by the processor, it is possible to combine them following the prescription presented in section 1.6 to generate global maps of the random and absolute errors.

Figures 4.5–4.9 show the random error maps for each of the major continents. These maps show how the increased number of looks which are obtained at higher latitudes reduces the random error.

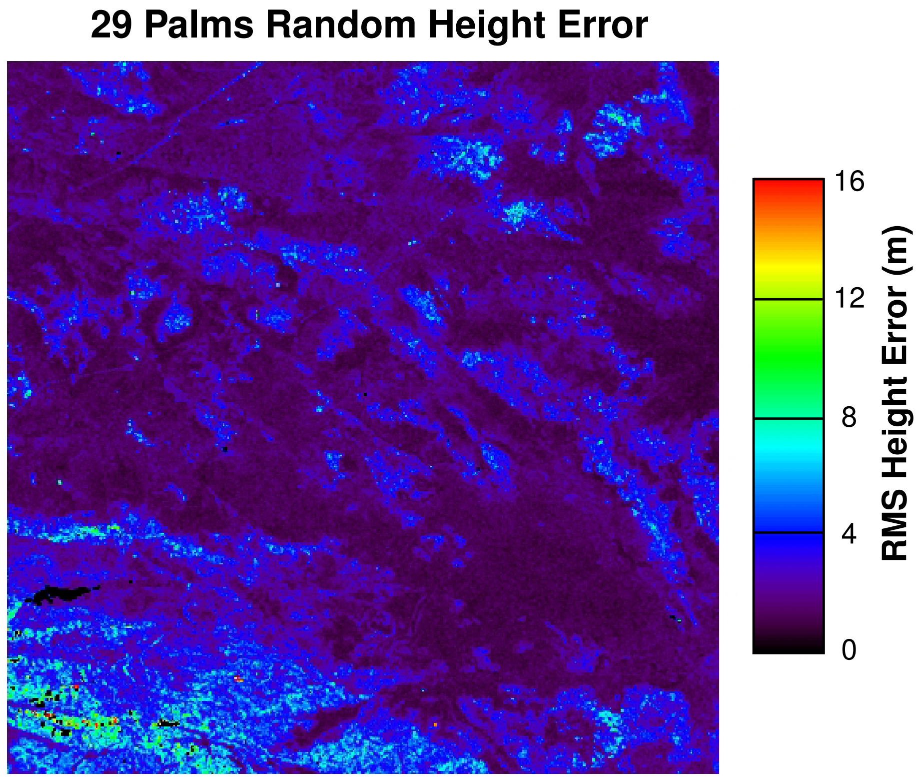

Figure 4.2: Height RMS calculated using an 11 pixel averaging window. This is an estimate of the height random error.

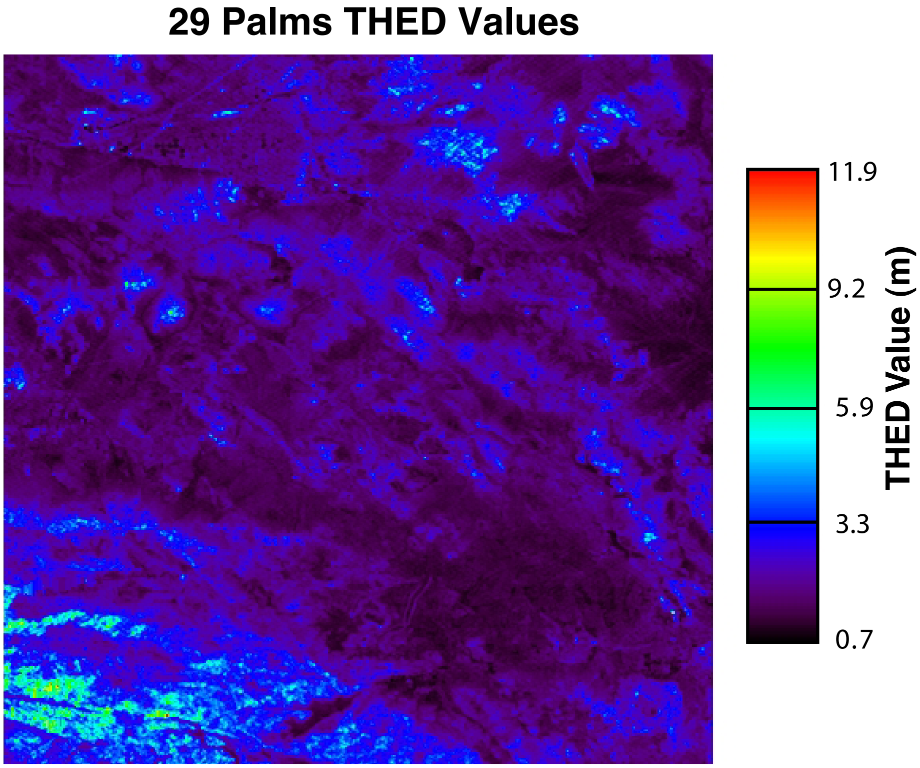

Figure 4.3: THED values computed for the 29 Palms cell.

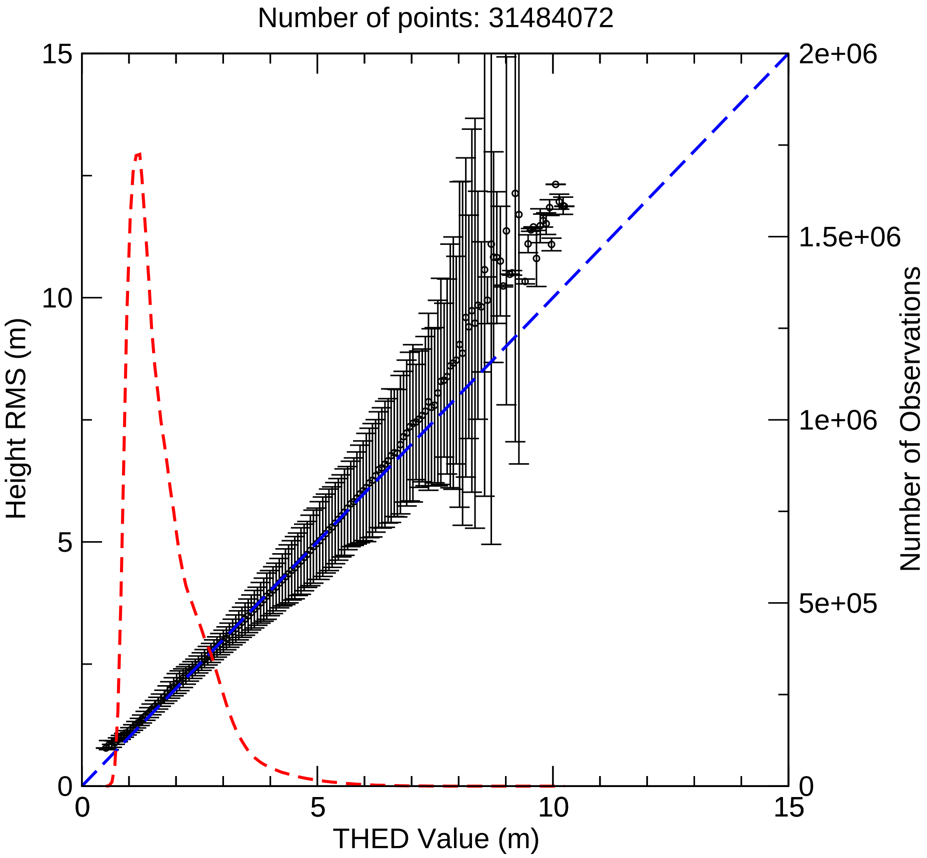

Figure 4.4: Statistical relationship between the THED values and the estimated random error. The red dashed curve represents the (arbitrarily normalized) histogram of the values used to derive the relationship. Notice the excellent agreement for most of the data range. A slight underestimate of the validation error estimates can be seen for large error values.

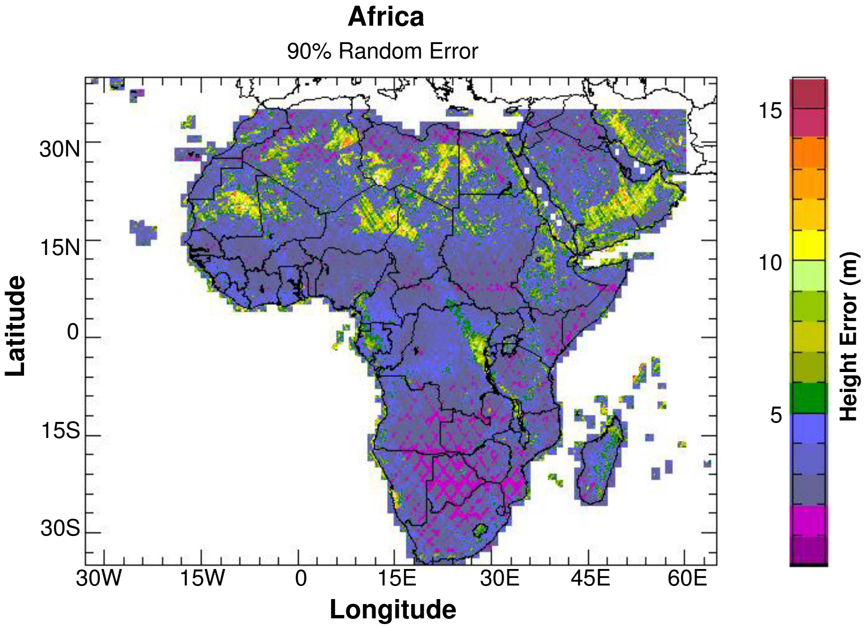

Figure 4.5: Africa random error map at 1/8° resolution.

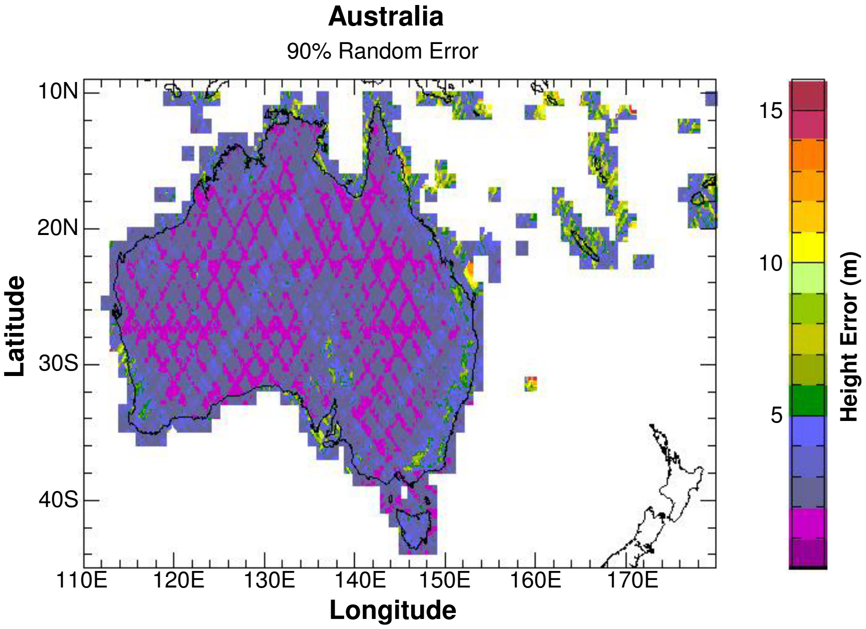

Figure 4.6: Australia random error map at 1/8° resolution.

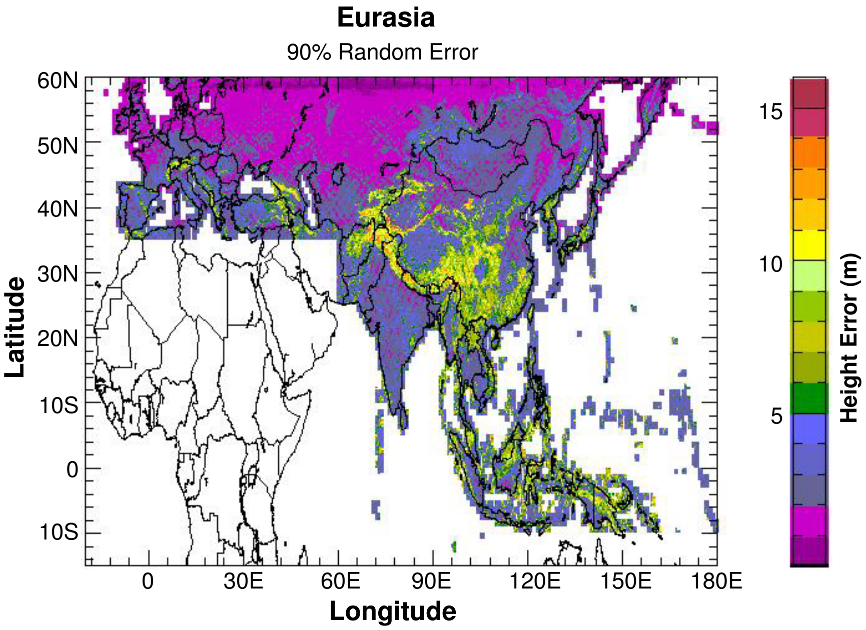

Figure 4.7: Eurasia random error map at 1/8° resolution.

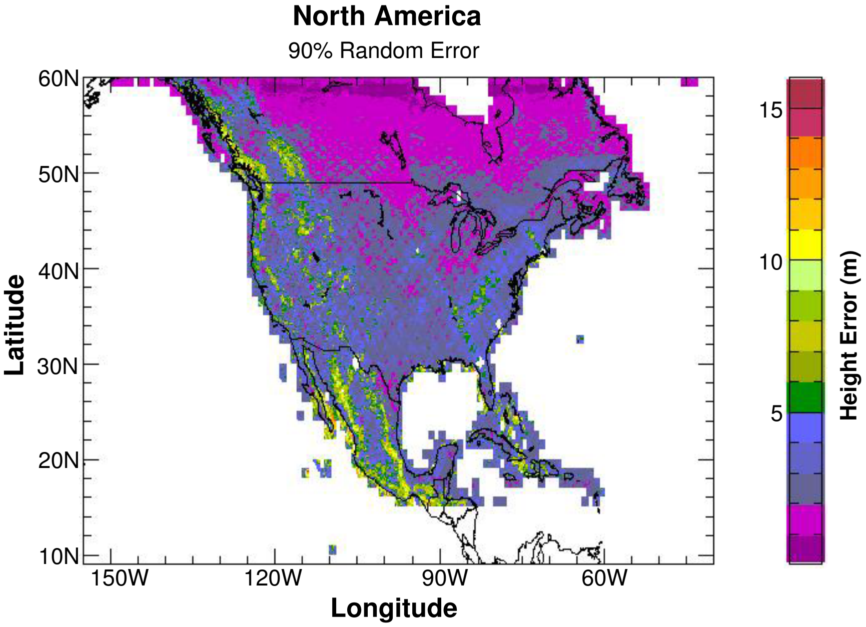

Figure 4.8: North America random error map at 1/8° resolution.

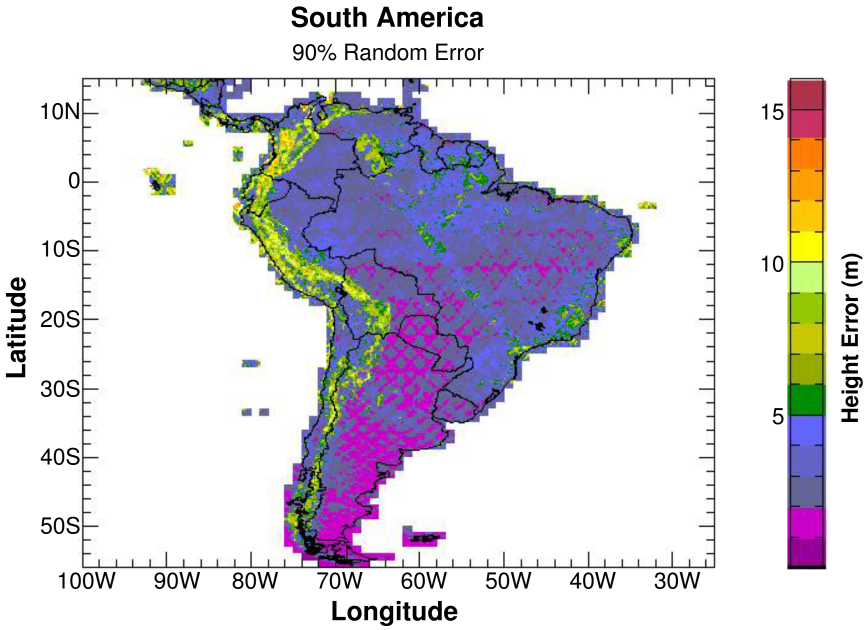

Figure 4.9: South America random error map at 1/8° resolution.

Because the number of looks varied at lower latitudes, a cross-hatched pattern is seen in some areas. This again reflects the fact that areas with additional data will have lower random errors.

The maps also show the relationship between topography and random error (Himalayas, Andes, Rockies, etc.) and between radar brightness and random error (Sahara, Saudi Arabia). Except in areas of high relief or low cross section, the error is typically < 5 m. At higher latitudes or for flat regions with good coverage, the magnitude of the random error can be < 2 m (90%). In the areas of highest error, values are on the order of 10 m.

Finally, we combine the random errors together with the long wavelength error estimates to obtain the formal estimates of absolute error shown in Figures 4.10–4.14. Note that some of the patterning in the random error maps, due to variations in sampling, is also seen in the absolute error maps.

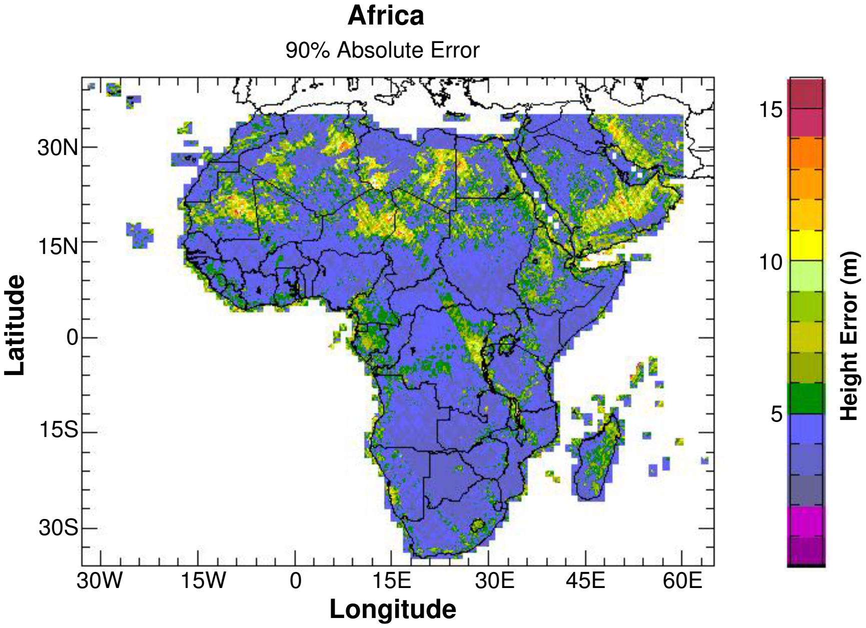

Figure 4.10: Africa estimated absolute 90% vertical error.

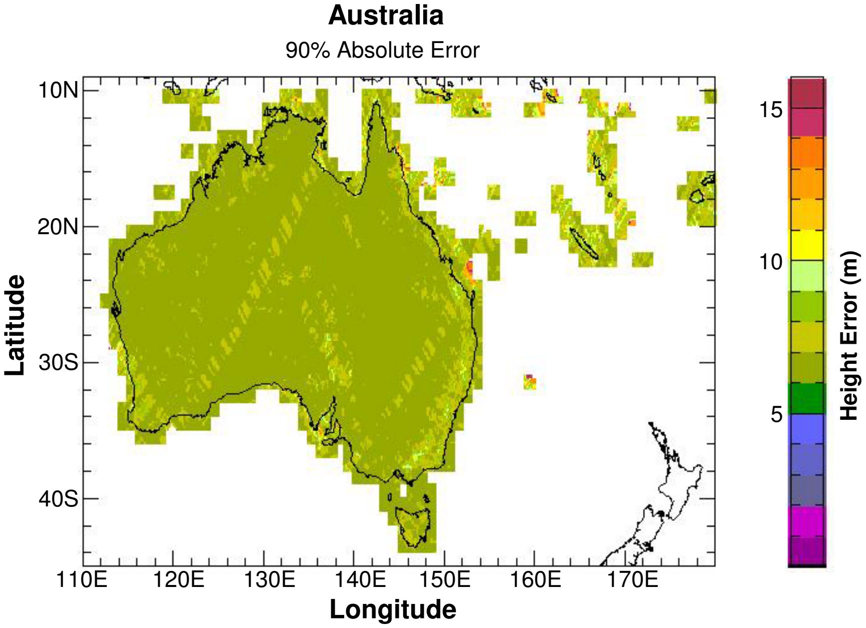

Figure 4.11: Australia estimated absolute 90% vertical error.

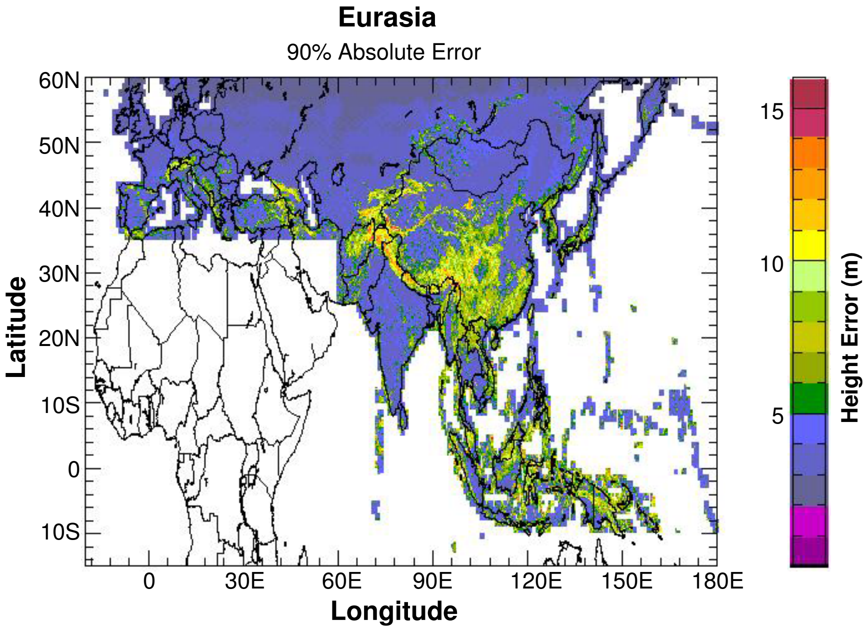

Figure 4.12: Eurasia estimated absolute 90% vertical error.

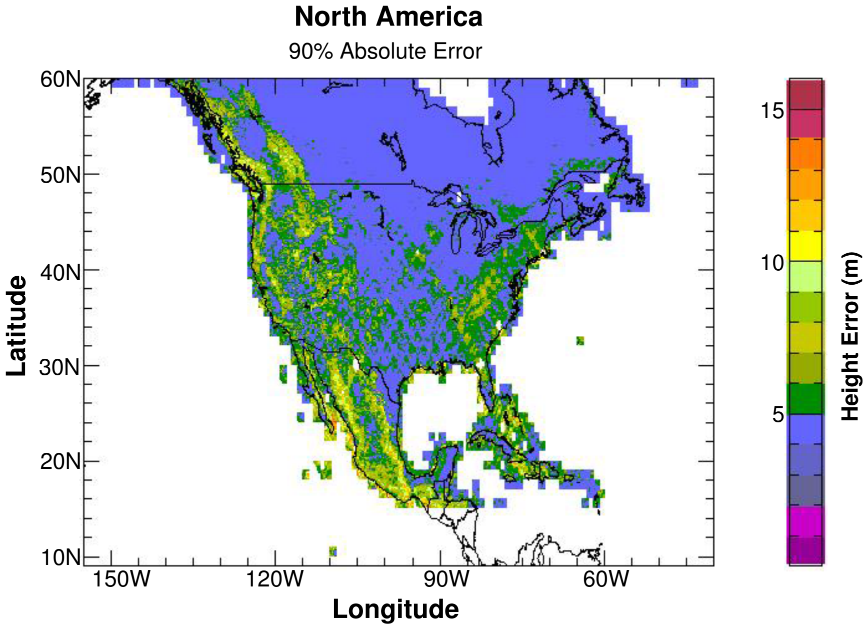

Figure 4.13: North America estimated absolute 90% vertical error.

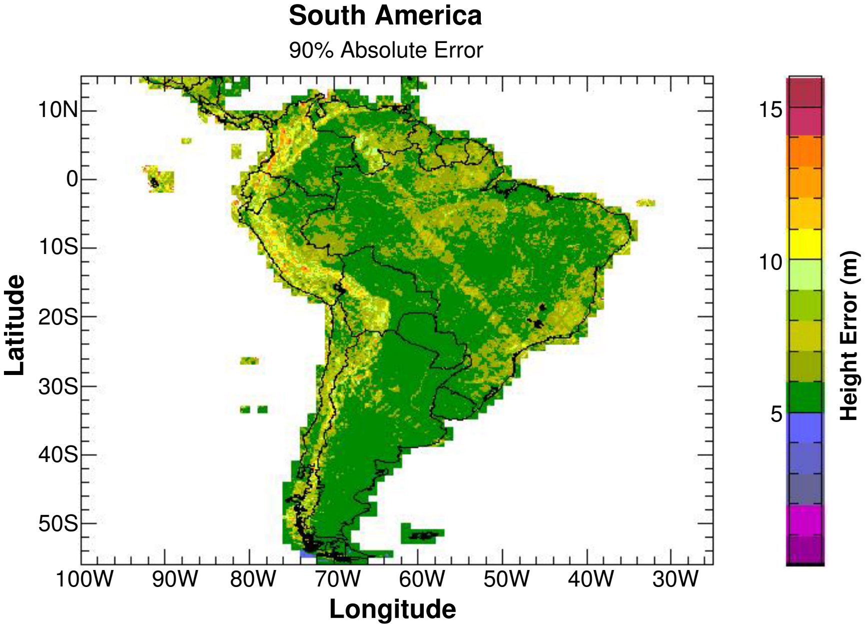

Figure 4.14: South America estimated absolute 90% vertical error.

Chapter 5

Geolocation Error

In contrast to the previous sections, the estimation of geolocation accuracy requires the identification of specific geometric features in either the SRTM topography or in the image. In the following sections, both techniques are utilized, sometimes jointly to obtain estimates of the geolocation accuracy of SRTM.

In the first section, radar corner reflectors, which can be identified in the image (both in the range-Doppler and ground planes) are used to estimate the system delay errors, which cause a geolocation error in the look direction of the radar.

In the second section, kinematic GPS track topography and road detection are combined to estimate the residual planimetric errors after timing errors are corrected.

The final geolocation results are reported in Table 1.3, which shows that the geolocation requirements are amply met by the SRTM data.

5.1 Geolocation Error from Corner Reflectors

5.1.1 Ground Truth

Standard 6′ (1.8 meter) and 8′ (2.4 meter) trihedral corner reflectors were deployed at calibration sites in California and Australia for both the ascending-orbit and descending-orbit phases of the SRTM mission. Ground truth was established to within 10 cm (absolute) by surveying the GCP locations using the GPS and reducing data with the JPL GIPSY software.

5.1.2 Range Estimation in the SRTM Range-Doppler Data Products

For each patch of data produced by the SRTM GloboProc processor, raw data are motion compensated to a reference path $\vec{P}(S_p)$, which is linear in the SCH-coordinate system, and parameterized in terms of the platform's along track coordinate S_p:

$$\begin{aligned} C_p(S_p) &= C_0 + (S_p - S_0)\frac{dC}{dS} \\ H_p(S_p) &= H_0 + (S_p - S_0)\frac{dH}{dS}, \end{aligned} \tag{5.1}$$

where (S_0, C_0, H_0) are the platform's initial position. The range to the GCP is then:

$$\begin{aligned} r(S_p) &= ||r(\vec{S}_p)||, \\ \vec{r}(S_p) &= \vec{P}(S_p) - \vec{P}_{\mathrm{GCP}}, \end{aligned} \tag{5.2}$$

where $\vec{P}_{\mathrm{GCP}}$ is this fixed target position. The GCPs Doppler shift as the platform moves along-track is:

$$f(S_p, \vec{r}) = \frac{2}{\lambda}\vec{V} \cdot \frac{\vec{r}}{r}, \tag{5.3}$$

where λ is the radar wavelength and $\vec{V}$ is the platform velocity. The Doppler centroid along the ground swath (as given in the baseline file) is approximated by a cubic polynomial in range:

$$f_0(S_p, |r|) = d_0 + d_1|r(S_p)| + d_2|r(S_p)|^2 + d_3|r(S_p)|^3. \tag{5.4}$$

In order to find the platform position at imaging, Equation 5.3 and Equation 5.4 are evaluated at possible platform positions associated with records in the baseline file, and interpolated so that the values of S_p^i that yields

$$f(S_p^i, \vec{r}) \approx f_0(S_p^i, |r|) \tag{5.5}$$

can be obtained. The platform position at imaging is given by Equation 5.1 evaluated at $S_p = S_p^i$.

Corner reflector positions are extracted from the single-look complex (SLC) data products using a 32-fold oversampling (i.e., Nyquist interpolating the band-limited data so that the point to point separation is 1/32 of the original data spacing). The peak pixel position N_{pix} is converted to a range using

$$||r|| = r_0 + \delta r N_{\mathrm{pix}}; \tag{5.6}$$

the starting range r_0 and range bin size $\delta r = 13.24\,\mathrm{m}$ are obtained from the processor by setting the `mocomp_params` debug flag.

5.1.3 Optimizing the Common Range Delay

The optimum common range delays are determined for each beam as follows: Range offsets are measured for each GCP for five time delays spanning $0.08\,\mu$s near the optimum. At each time delay, the average range offset is calculated for all GCPs, and the resulting 5 points are fit with a line. The optimum time delay is then the root of the linear fit. The results are shown in Fig 5.1, and the optimum time delays are given in Table 5.1.

5.1.4 Error Analysis

The standard deviation of the range error for each beam is given in Table 5.2. The average value is 1.3 m. The distribution of range offsets for all beams is shown in Figure 5.2.

Systematic Dependences

The range offsets are plotted versus orbit number in Figure 5.3, along with a linear fit of the range offset versus orbit. The slope of the linear fit is -5.9 ± 4.2 mm/orbit. Dividing the measurements into descending and ascending orbits (early and late times) gives the time-dependence shown in

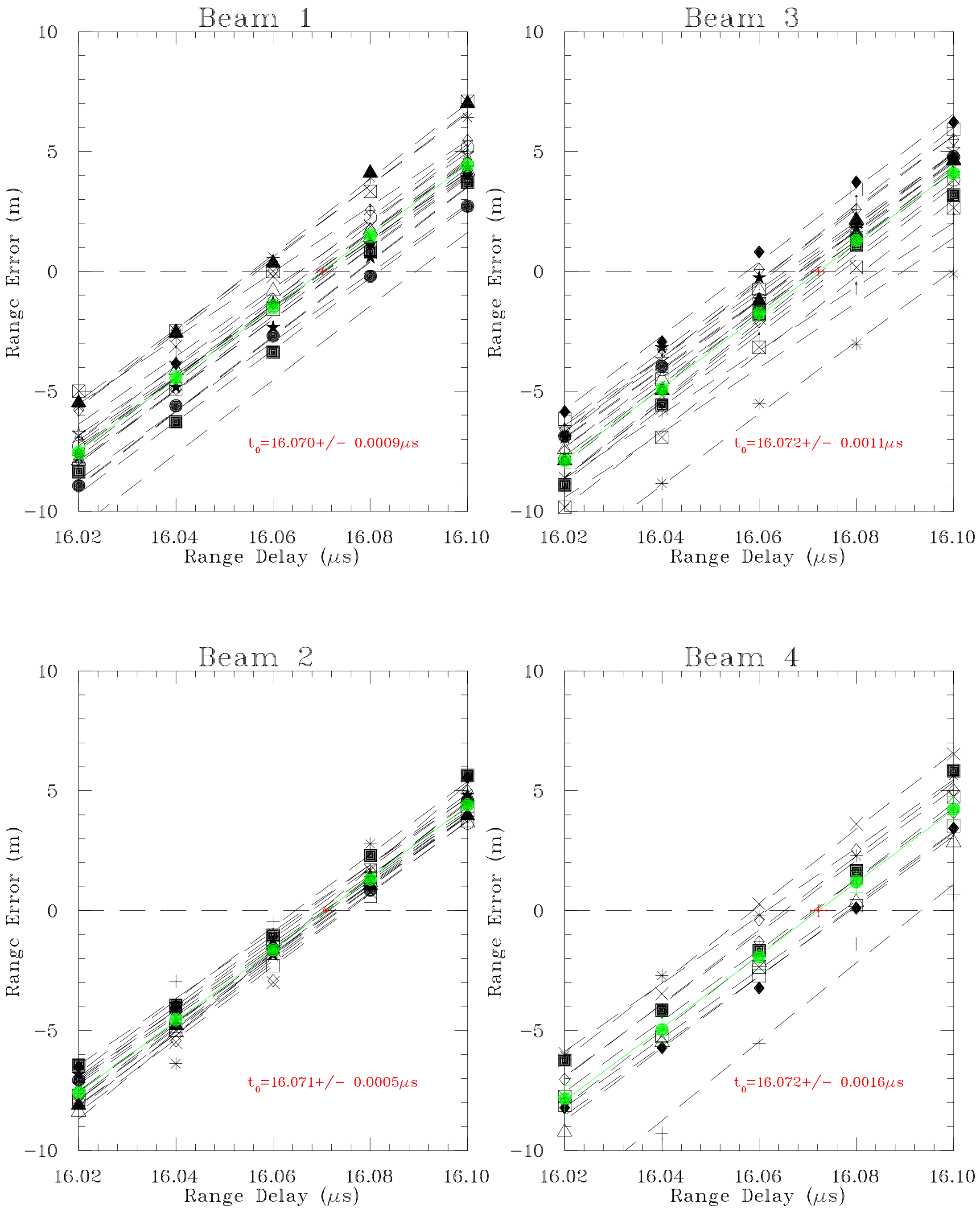

Figure 5.1: Range offset versus time delay for all GCPs in each of Beams 1-4. The various symbols are assigned to different GCPs and the black dashed lines are linear fits to each GCP. The green line shows the fit to the average as described in the text, and the red point shows the optimum time delay, t_0, along with the one standard deviation (statistical) uncertainty.

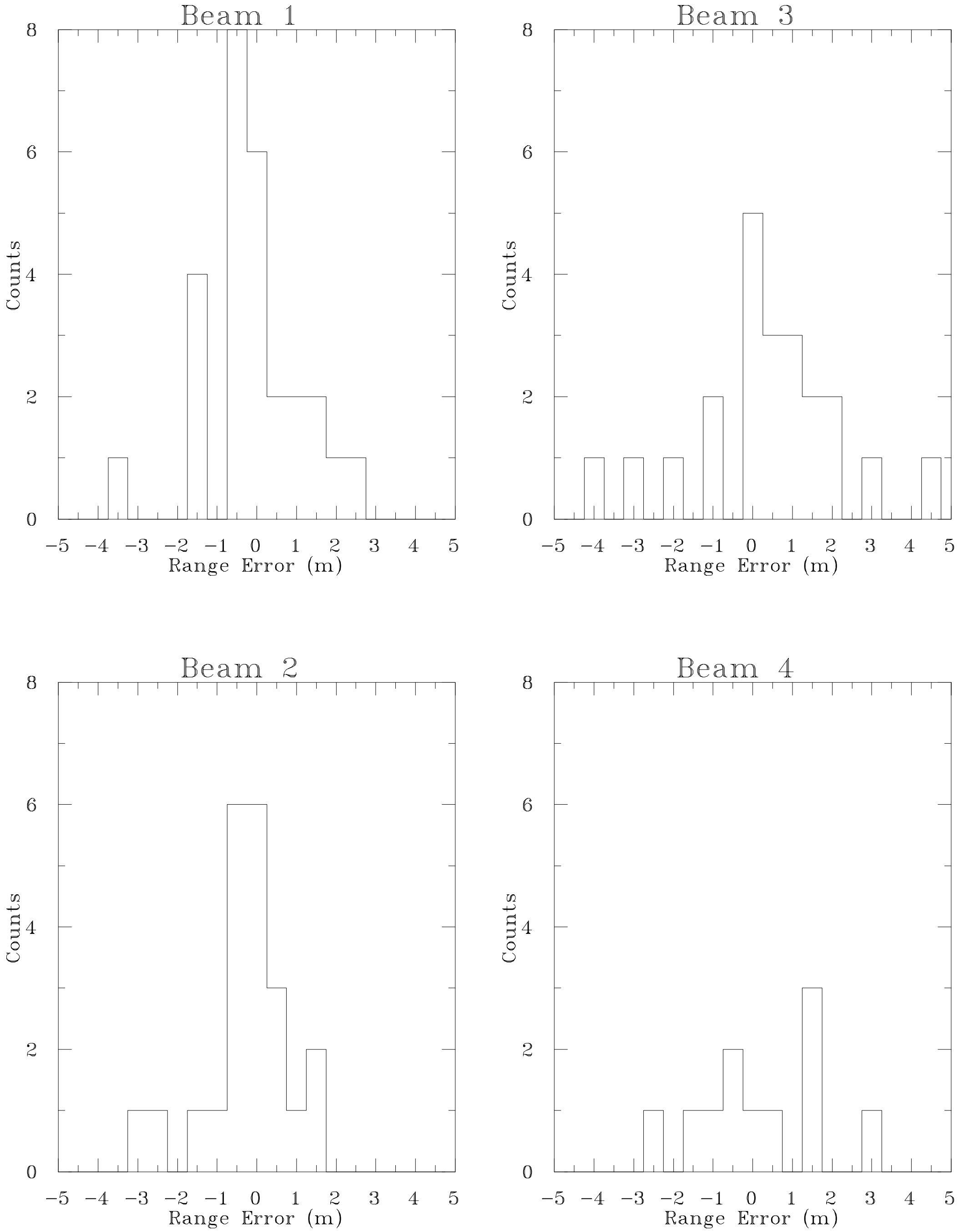

Figure 5.2: Distribution of range offsets for beams 1–4. Counts are are given per 0.5 m bin.

Table 5.1: Common time delays, which are a correction to the two-way travel time, with statistical uncertainty for each beam.

Beam	Time Delay (μs)
1	16.070 ± 0.0009
2	16.071 ± 0.0004
3	16.072 ± 0.0011
4	16.072 ± 0.0016

Table 5.2: Moments of the distribution of range offsets.

Beam	No. of GCPs	$\langle \delta R \rangle$ (m)	σ (m)
1	27	-0.11 ± 0.23	1.2
2	22	-0.24 ± 0.23	1.1
3	21	$+0.31 \pm 0.39$	1.8
4	10	$+0.16 \pm 0.49$	1.6

Table 5.3. There is a change of -0.37 ± 0.32 m going from descending to ascending orbits. Dividing the GCPs into Northern Hemishpere (California) and Southern Hemispere (Australia) yields no systematic differences.

5.1.5 Corner Reflector Location

The location of the corner reflector peak in the SLC imagery should move linearly with respect to changes in the time delay. The response for a typical corner reflector is shown in Figure 5.4 (top). The observed slope of -150 ± 2 m/μs is consistent with the expected value $0.5c/n$, where c is the speed of light and $n \approx 1$ is the index of refraction. Figure 5.4 (bottom) shows the residual of the linear fit. The residual is oscillatory with a peak range of roughly ±0.6 m; the mimima occur when the GCP peak is located either at a pixel edge or center. No corrections for this effect were applied

Table 5.3: Temporal and spatial dependence of range offsets.

Data Qualifier	No. of GCPs	Mean Range Offset (m)
Descending	39	$+0.21 \pm 0.27$
Ascending	31	-0.16 ± 0.17
California	43	-0.02 ± 0.20
Australia	27	$+0.09 \pm 0.22$

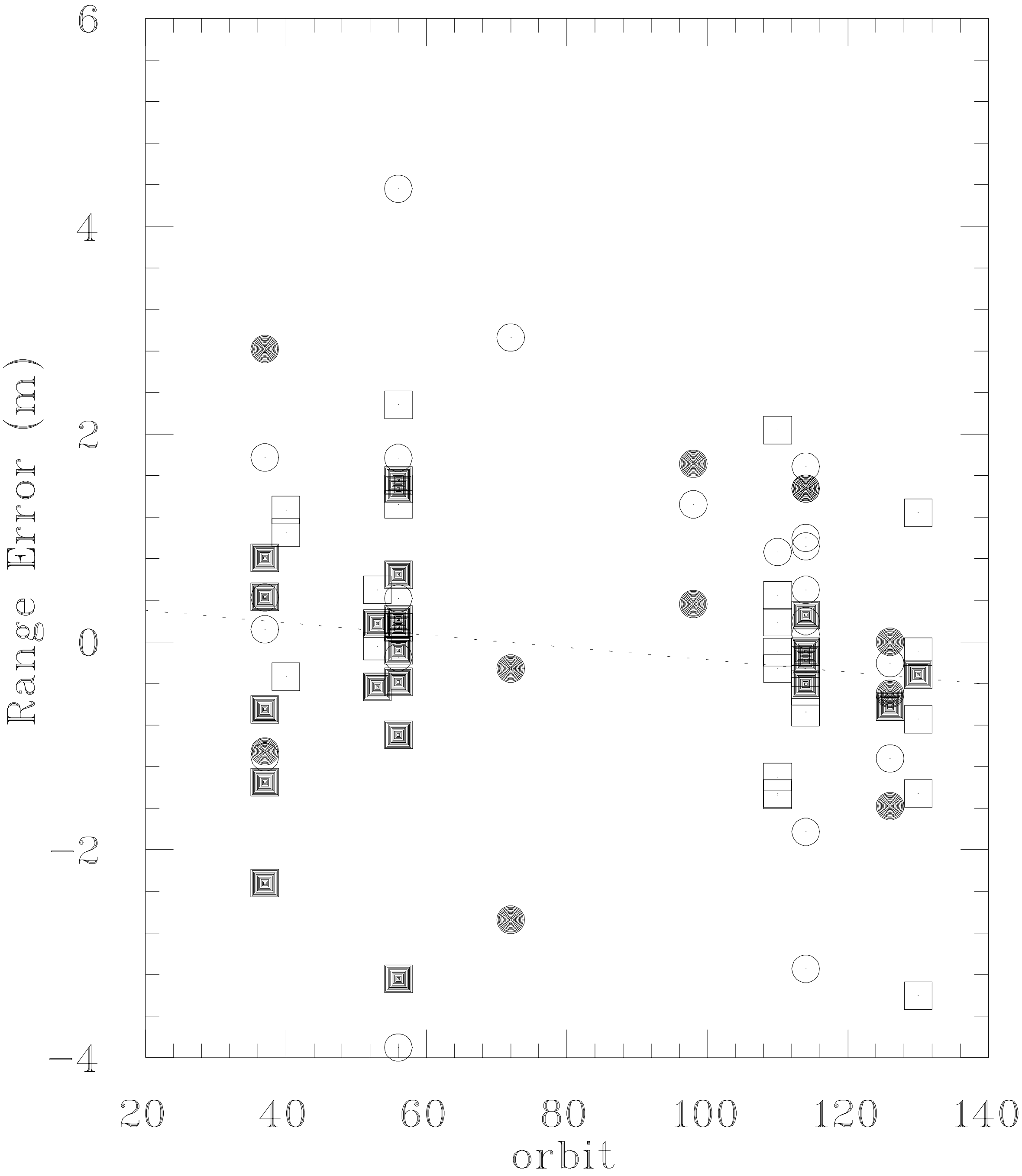

Figure 5.3: Range offsets for beams 1 (open squares), 2 (filled squares), 3 (open circles) and 4 (filled circles). The dashed line is a linear fit.

to this analysis.

5.2 Geolocation Error from Kinematic GPS GCPs

5.2.1 Geolocation Validation

DEM Geolocation Validation

The DEM Geolocation validation is derived by testing how well the shape of a kinematic GPS track conforms to the DEM surface, on a cell by cell basis (see Figure 5.5). The GPS track is shifted from its nominal position over a grid of ±2 arc-seconds in 0.1 arc-second steps, in both the North/South, East/West directions. For each grid point, the standard deviation $\sigma(\delta_{\mathrm{lat}}, \delta_{\mathrm{lon}})$ of the height error (i.e., the difference between the 32-oversampled SRTM heights and the GPS heights) is recorded. The best-fit geolocation error is determined by the minimum of the surface over the grid. The surface for a mountainous region appears in Figure 5.6. If each SRTM pixel were independent, the uncertainty in the minimum's position, $(\delta x, \delta y)$, could be estimated by the extent of the one-sigma contour defined by:

$$\sigma(\delta_{\mathrm{lat}}, \delta_{\mathrm{lon}}) \leq \sigma^{\mathrm{min}} + \frac{\sigma^{\mathrm{min}}}{\sqrt{N}}, \tag{5.7}$$

where N is the number of pixels in the cell containing at least one ground truth point and σ^{min} is standard deviation at the minimum. It has been determined empirically that Eq. 5.7 overestimated the uncertainty by about a factor of two, and this discrepancy is attributed to pixel-to-pixel correlations in the height error.

Image Geolocation Validation

The DEM Geolocation image validation is based on the assumption that roads are darker than their surroundings. The image brightness, at a GPS point is defined by a cubic convolution interpolation of the image at the latitude and longitude of the GPS data point.

For a surface of constant brightness (e.g., a road), the brightness of the sampled points will be χ^2-distributed with $2n$ degrees of freedom, where n is the number of looks. SRTM data typically have between 2 and 5 looks.

Data are analyzed on a cell by cell basis. In order to avoid contamination of the measured mean brightness by bright objects such as buildings or vehicles, any data point within 3 pixels of a point brighter than 8 times the median brightness is rejected (Figure 5.7).

The entire GPS track over a cell is shifted from its nominal position over a grid of ±2 arc-seconds in 0.1 arc-second steps, in both the North/South, East/West directions. For each grid point, the mean brightness of the interpolated $\bar{I}(\delta_{\mathrm{lat}}, \delta_{\mathrm{lon}})$ image is recorded. The best-fit geolocation error is determined by the minimum of the surface over the grid. A surface for a typical cell appears in Figure 5.9. The uncertainty in the position of the minimum is estimated by the extent one-sigma contour defined by:

$$\bar{I}(\delta_{\mathrm{lat}}, \delta_{\mathrm{lon}}) \leq \bar{I}_{\mathrm{min}} + \frac{\sigma_{\bar{I}}^{\mathrm{min}}}{\sqrt{N}}, \tag{5.8}$$

where σ_{min} is the standard deviation at the minimum. As with the height error analysis, correlations in the magnitude of adjacent pixels cause Eq. 5.8 to overestimated the uncertainty in the position of the minimum by about a factor of two.

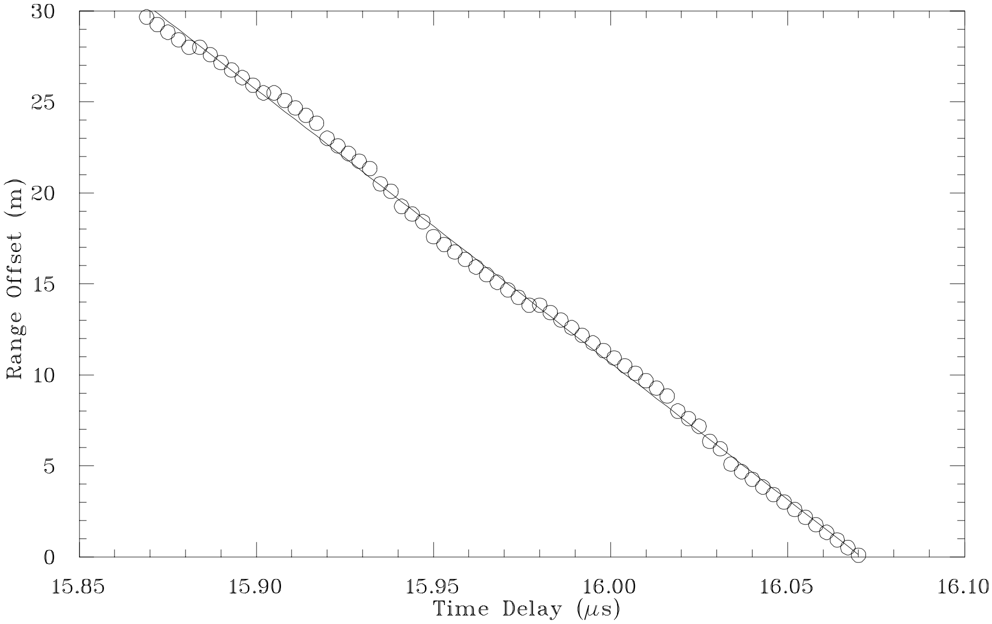

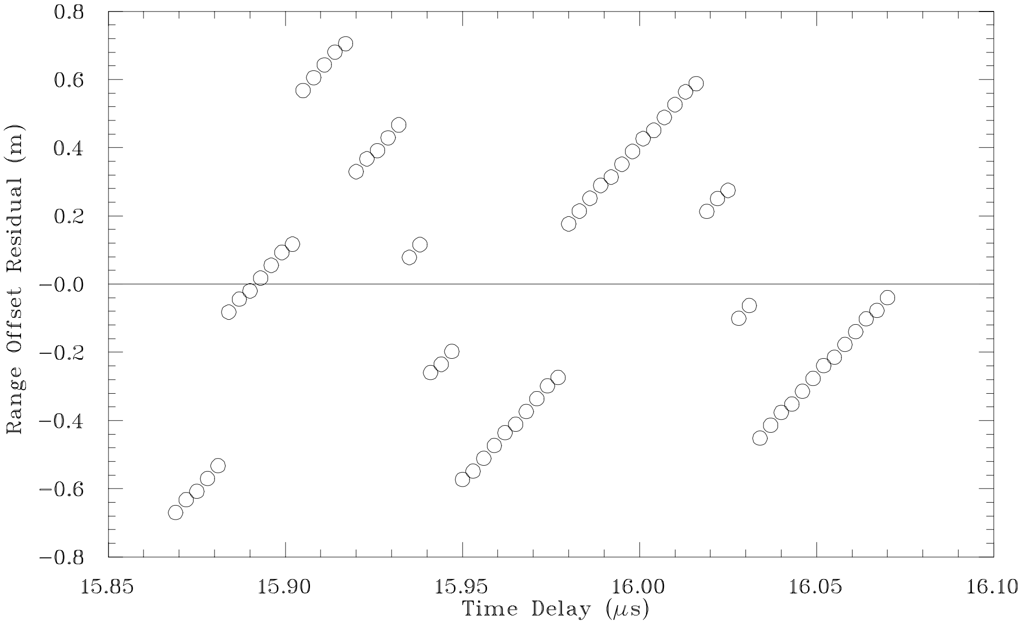

Figure 5.4: Top: Range offset versus time delay (open circles) and a linear fit (solid line). Bottom: Residual of linear fit. The range data were originally sampled at 13.24 m, but were processed to obtain a final sampling of 0.41 m.

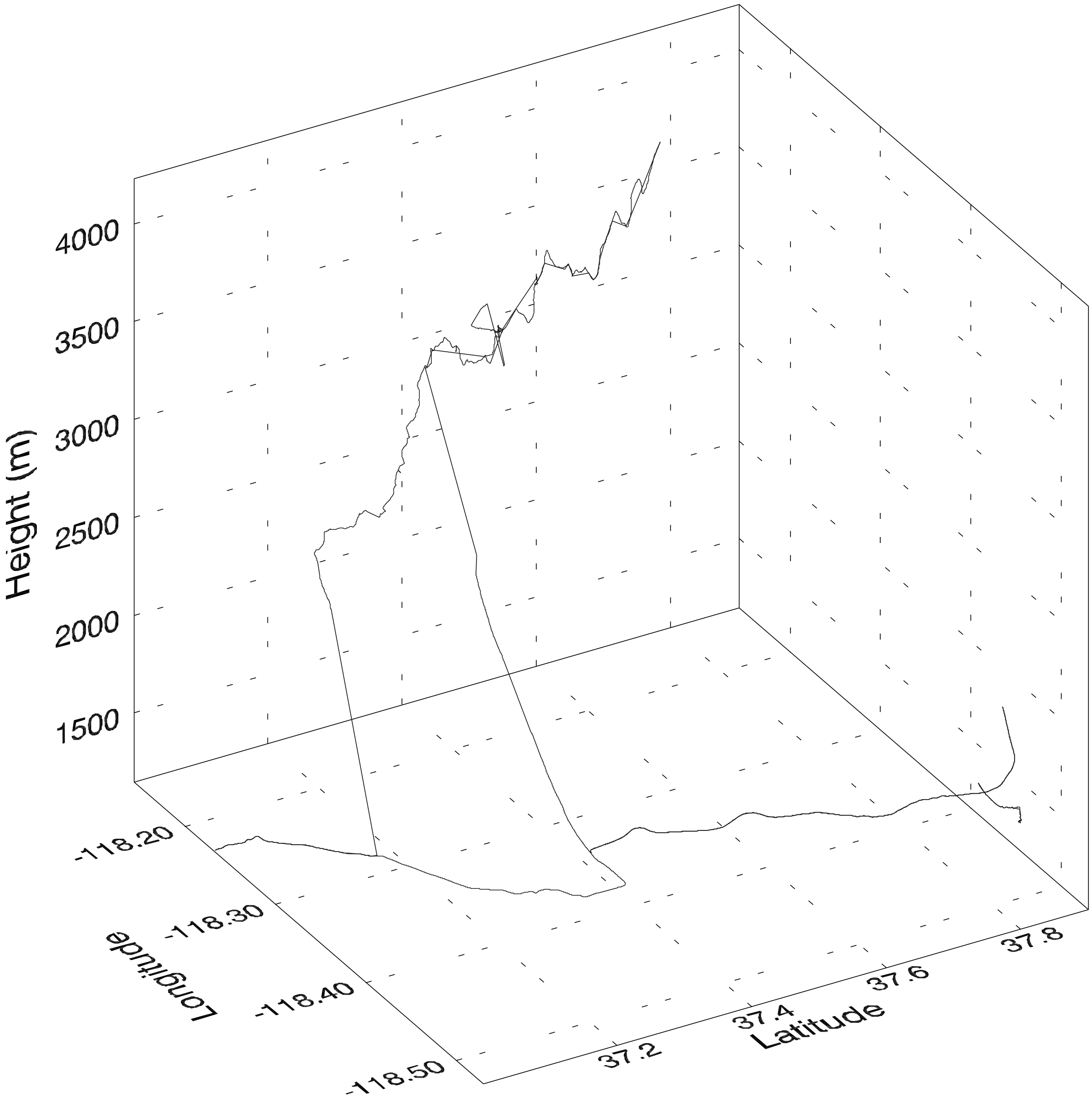

Figure 5.5: Kinematic GPS track over mountainous terrain, used in Figure 5.6. There are 6941 points.

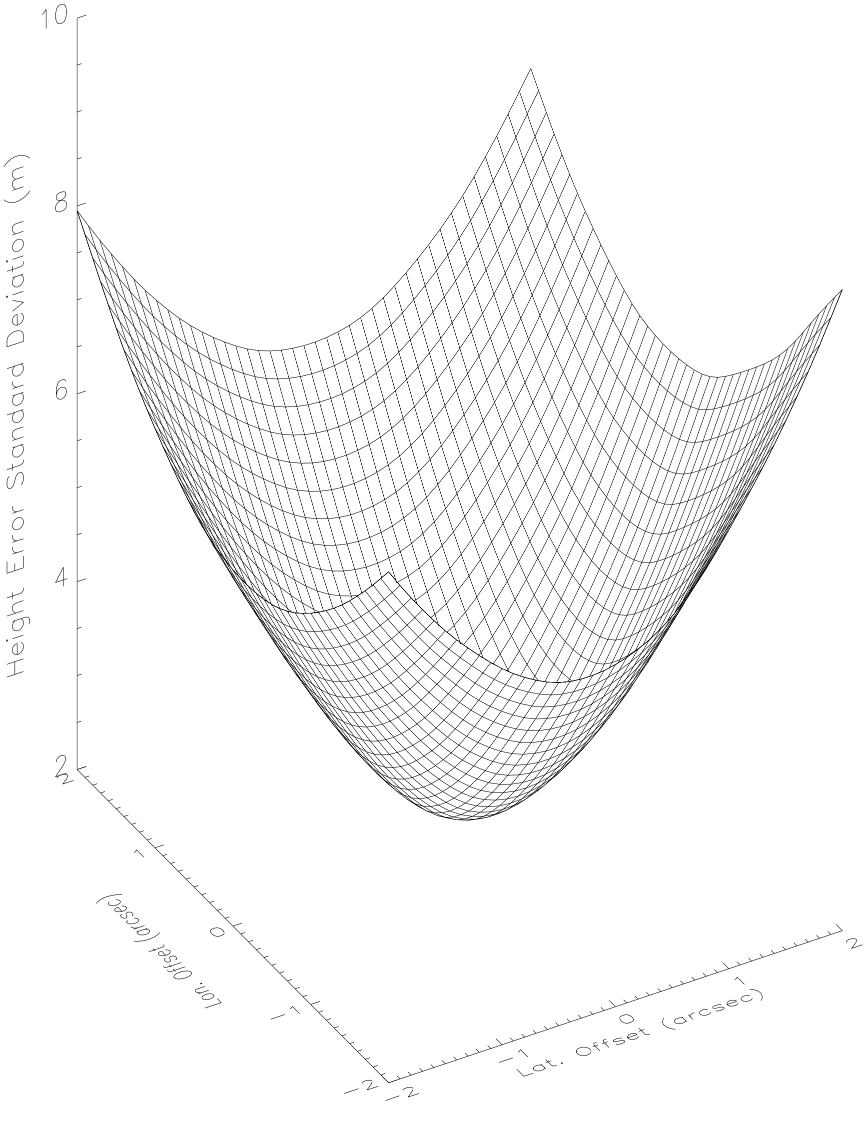

Figure 5.6: Surface plot of the standard deviation of the height error sampled along a kinematic GPS track over a mountainous SRTM cell (Figure 5.5). The best-fit σ is 2.38 meters. Eq. 5.7 yields a one-σ contour of 2.40 meters.

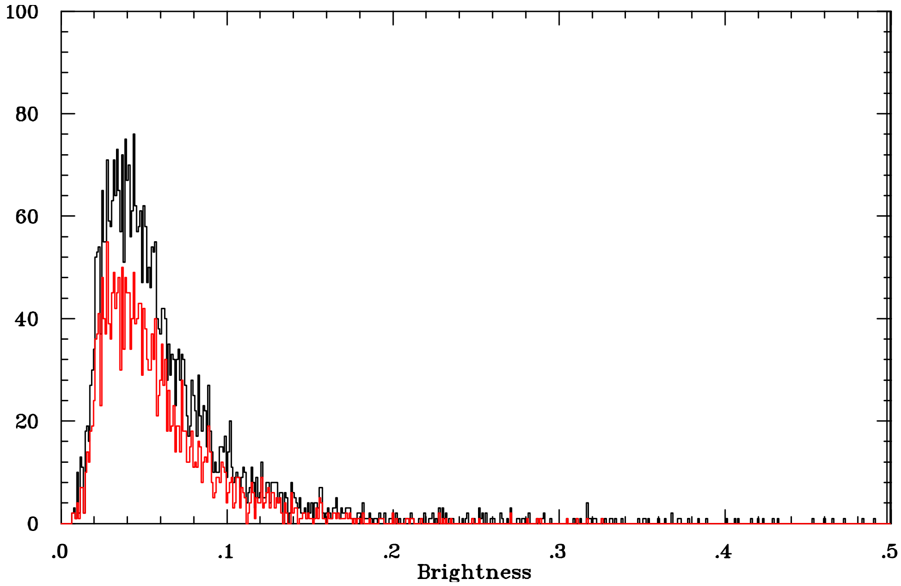

Figure 5.7: Histogram of the SRTM descending image brightness sampled along a kinematic GPS track with all data (Black) and with rejected points removed (Red). Note that there are 200 counts in the overflow bin (far right end of plot) that represent brightness values as great as 18.4. These large values are among the points that must be removed for the algorithm to work. The mean number of looks is 2.5.

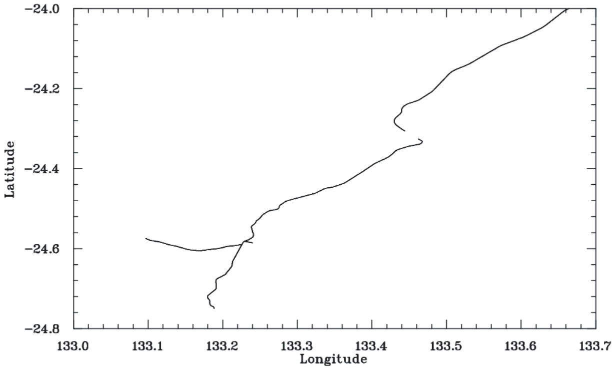

Figure 5.8: Kinematic GPS track used in Figure 5.9. There are 3862 points.

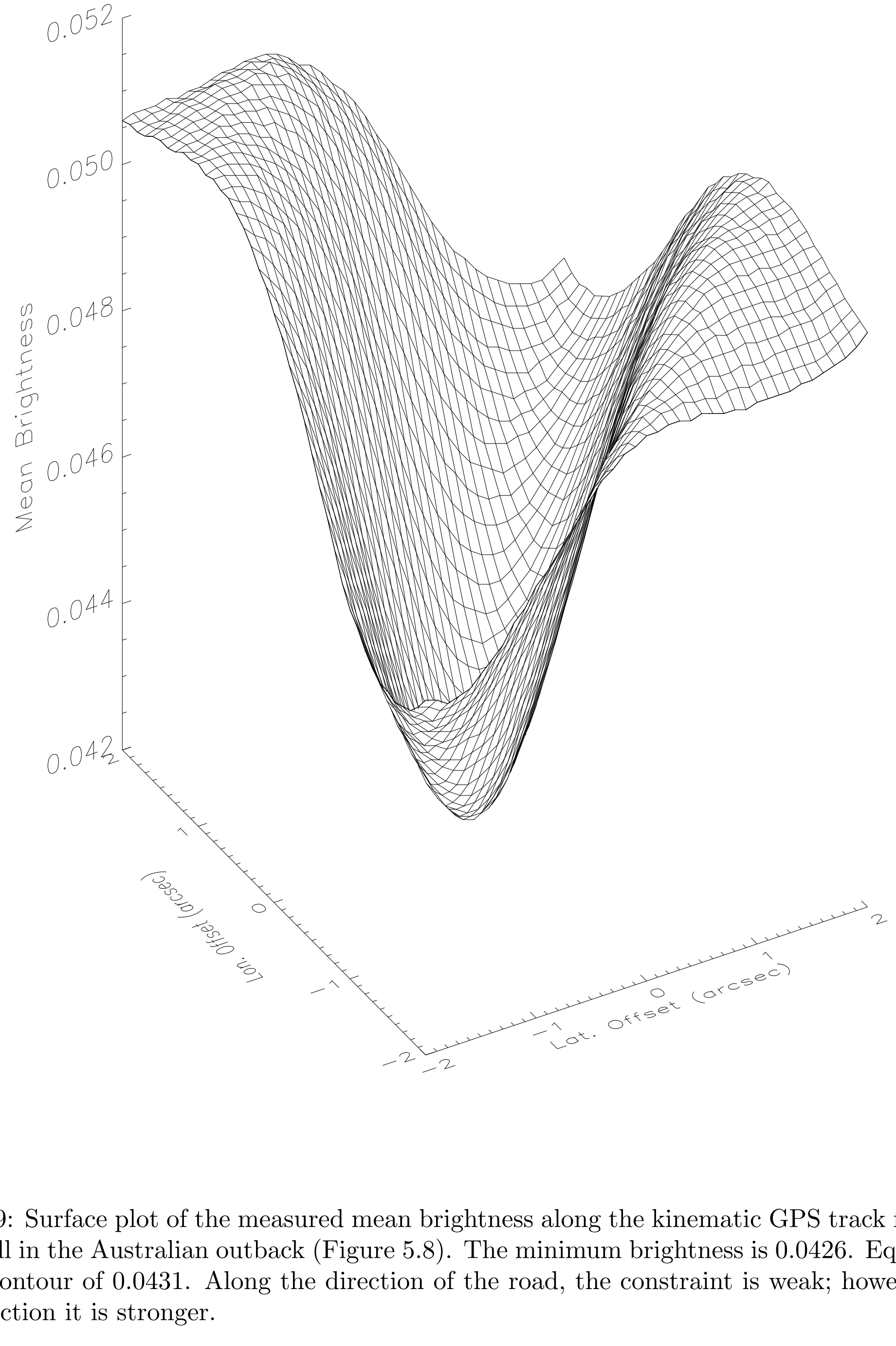

Figure 5.9: Surface plot of the measured mean brightness along the kinematic GPS track for a single SRTM cell in the Australian outback (Figure 5.8). The minimum brightness is 0.0426. Eq. 5.8 yields a one-σ contour of 0.0431. Along the direction of the road, the constraint is weak; however, in the cross direction it is stronger.

Continental Geolocation Validation

For each continent, the individual cells are combined into separate 10 by 10 degree super-cells in which mean geolocation errors are calculated from a weighted average of the aggregate cells. For instance, if a super cell contains N_c cells with latitude and longitude biases and uncertainties $(x_i, y_i) \pm (\delta x_i, \delta y_i)$ $(i = 1, 2, ..., N_c)$, then the weighted mean latitude bias for the super cell is defined by:

$$\bar{x} = \frac{1}{W} \sum_{i=1}^{N_c} w_i x_i, \tag{5.9}$$

where the weights are given by

$$w_i = \frac{1}{\delta x^2}, \tag{5.10}$$

and the total weight is

$$W = \sum_{i=1}^{N_c} w_i. \tag{5.11}$$

The uncertainty in the weighted mean bias is

$$\delta \bar{x} = \frac{\sigma_W}{\sqrt{N_{\text{eff}}}}, \tag{5.12}$$

where the weighted standard deviation is the defined from the weighted variance

$$\sigma_W^2 = \frac{N_c}{N_c - 1} \frac{1}{W} \sum_{i=1}^{N_c} w_i (x_i - \bar{x})^2, \tag{5.13}$$

and the effective number of measurements is

$$N_{\text{eff}} = \frac{1}{W} (\sum_{i=1}^{N_c} \frac{1}{\delta x})^2. \tag{5.14}$$

The longitude biases for the super cells are similarly defined with the y_i for each data set.

Because Eq. 5.7 and 5.8 over estimate the uncertainty in the position, the individual uncertainties $(\delta x, \delta y)$ have to be rescaled so that the uncertainty given by Eq. 5.12 is correct. This is done by defining two global scaling factors–one for both ascending and descending image data and one for height data–and then forcing the total chi-squared per degree-of-freedom for all super cells to be unity:

$$\chi^2/\nu = \frac{1}{N} \sum_{j=1}^{N_{\text{supercell}}} \sum_{i=1}^{N_c^j} \frac{(x_i^j - \bar{x}^j)^2}{(\delta x_i^j)^2} + \frac{(y_i^j - \bar{y}^j)^2}{(\delta y_i^j)^2} \equiv 1 \tag{5.15}$$

Here $j = (1, ..., N_{\text{supercell}})$ runs over the super cells and the various $i = (1, ..., N_c^j)$ label the cells within the j^{th} super cell. For image data, the number of degrees-of-freedom is twice that for height data, because both the ascending and descending data are combined. The resulting scale factors are both approximately 0.5.

Finally, the combined bias estimates are constructed by forming the weighted average of the ascending image, descending image, and height biases (in a manner analogous to Eqs 5.9–5.14). The complete results are show in Figures 5.10–5.33. The summary of the horizontal accuracy for each continent appears in Table 1.3. These values are derived from the weighted average of the black points, denoted by the red point, in the combined results (Figs. 5.13, 5.17, 5.21, 5.25, 5.29, and 5.33). The final results show that SRTM meets the geolocation accuracy requirements given in the first chapter.

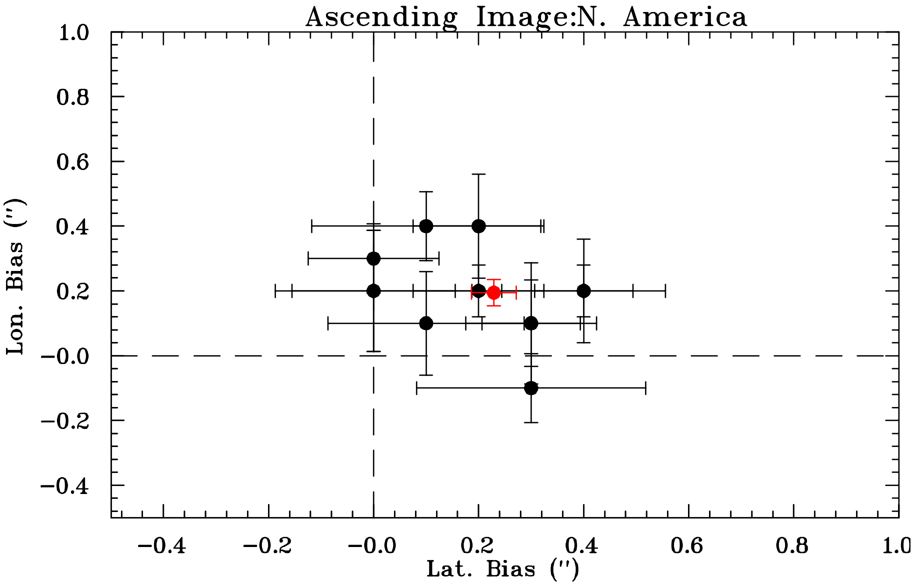

Figure 5.10: Best fit geolocation biases in ascending image data using 10° by 10° super-cells in North America.

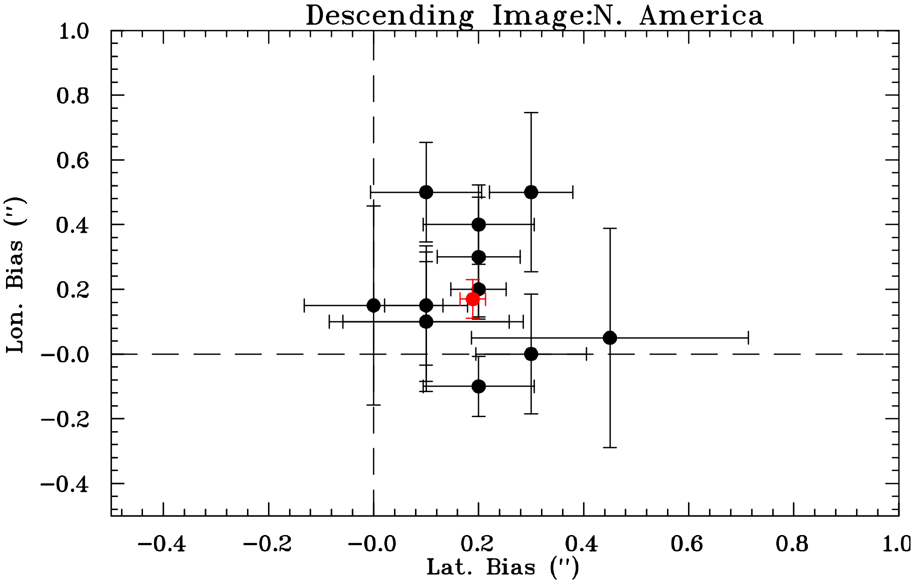

Figure 5.11: Best fit geolocation biases in descending image data using 10° by 10° super-cells in North America.

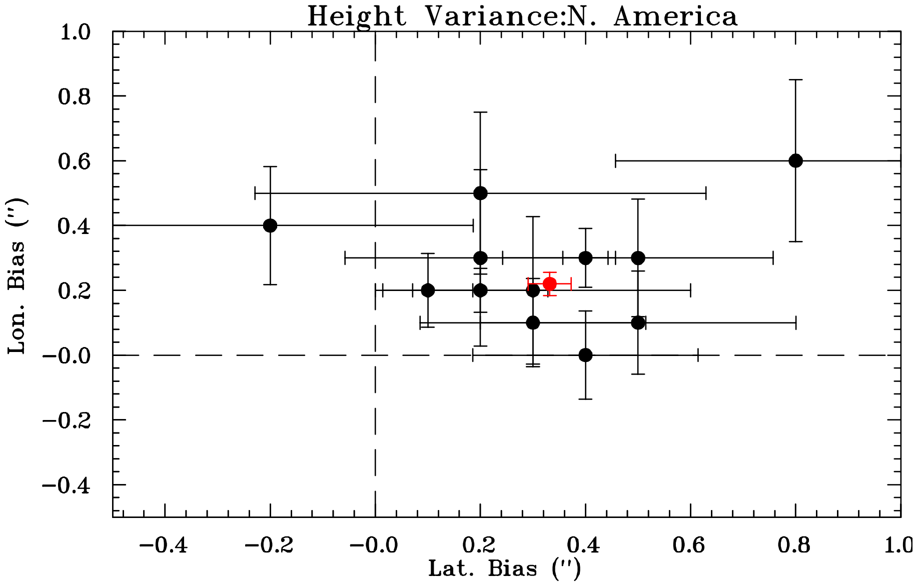

Figure 5.12: Best fit geolocation biases in DEM data using 10° by 10° super-cells in North America.

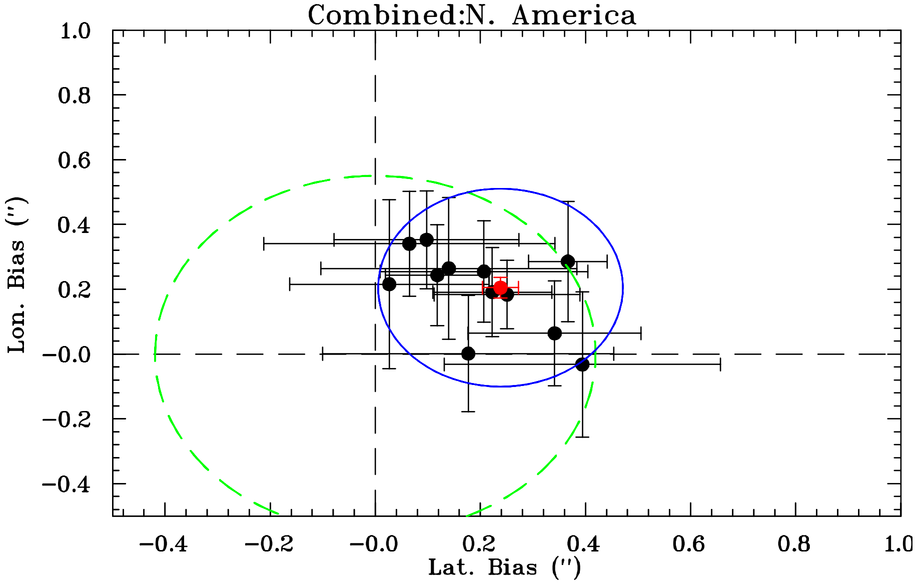

Figure 5.13: Best fit geolocation biases using combined height and image data for 10° by 10° super-cells in North America. The 90% absolute (relative) limits are represented by the green (blue) circles.

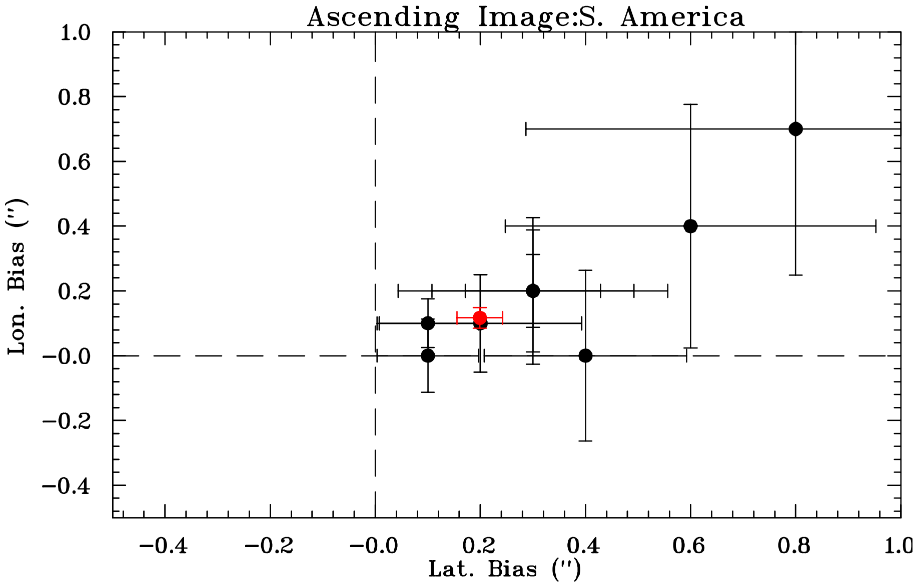

Figure 5.14: Best fit geolocation biases in ascending image data using 10° by 10° super-cells in South America.

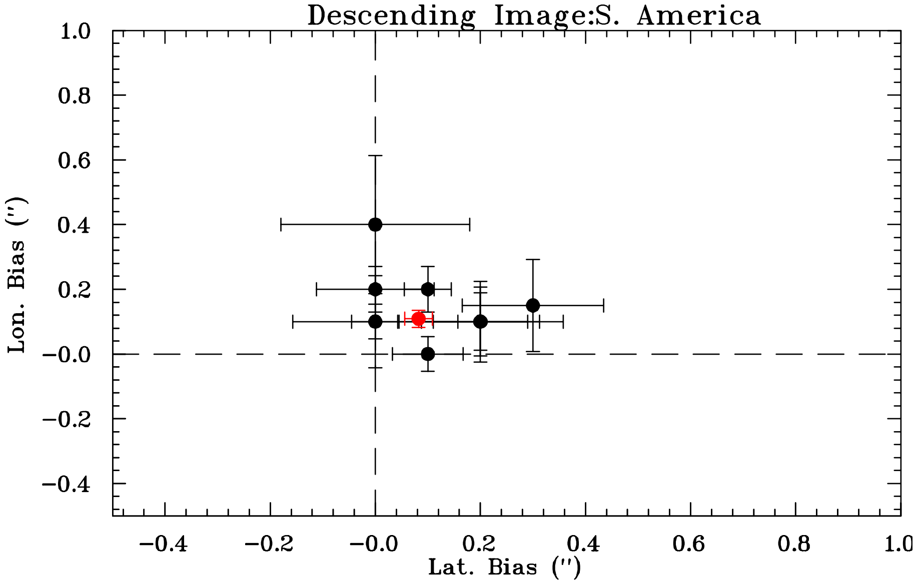

Figure 5.15: Best fit geolocation biases in descending image data using 10° by 10° super-cells in South America.

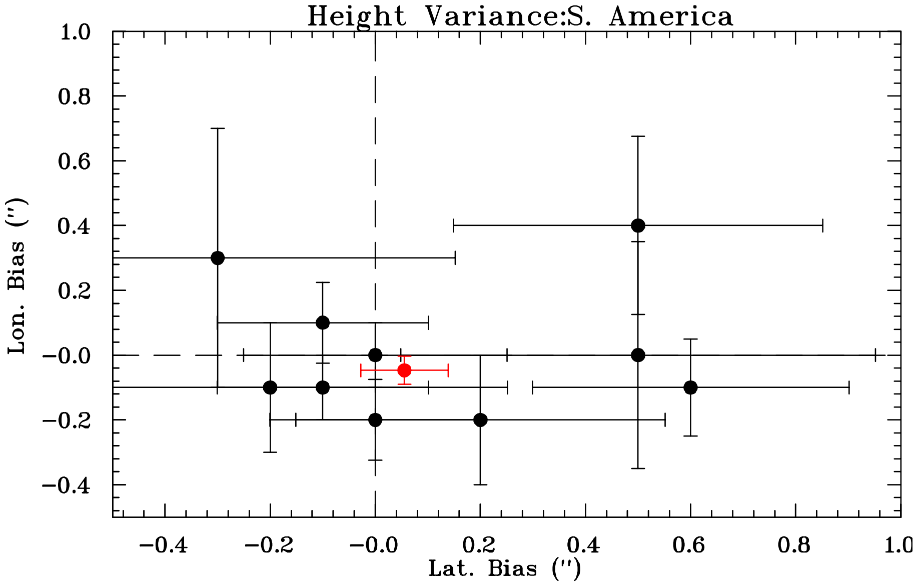

Figure 5.16: Best fit geolocation biases in DEM data using 10° by 10° super-cells in South America.

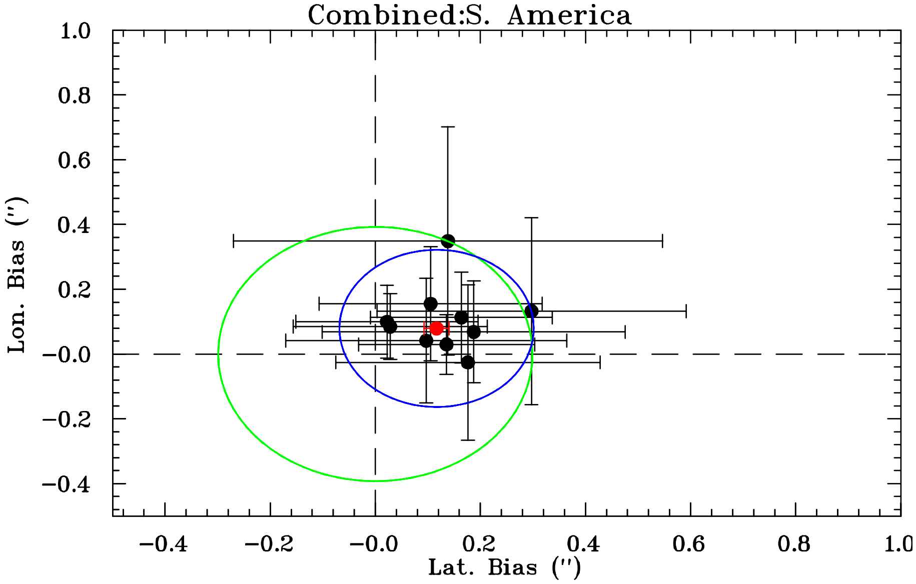

Figure 5.17: Best fit geolocation biases using combined height and image data for 10° by 10° super-cells in South America. The 90% absolute (relative) limits are represented by the green (blue) circles.

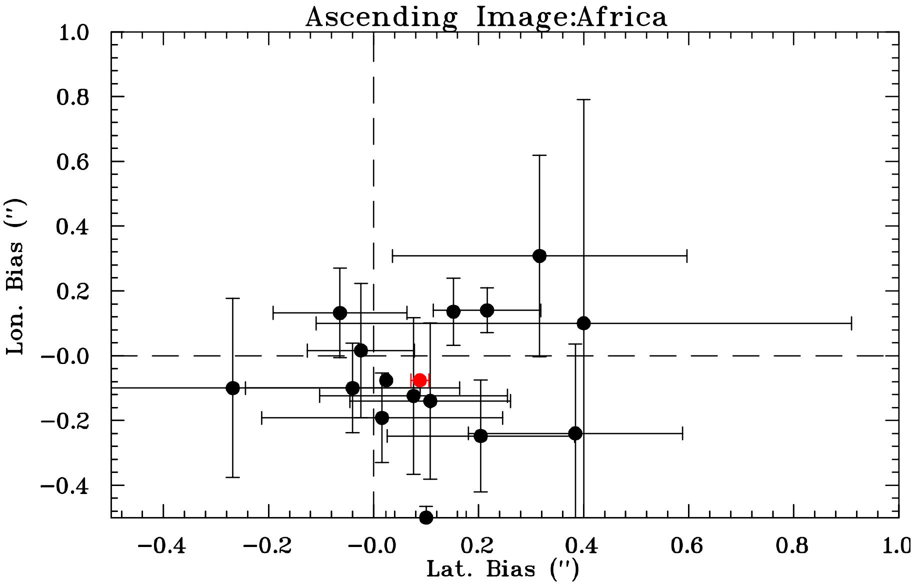

Figure 5.18: Best fit geolocation biases in ascending image data using 10° by 10° super-cells in Africa.

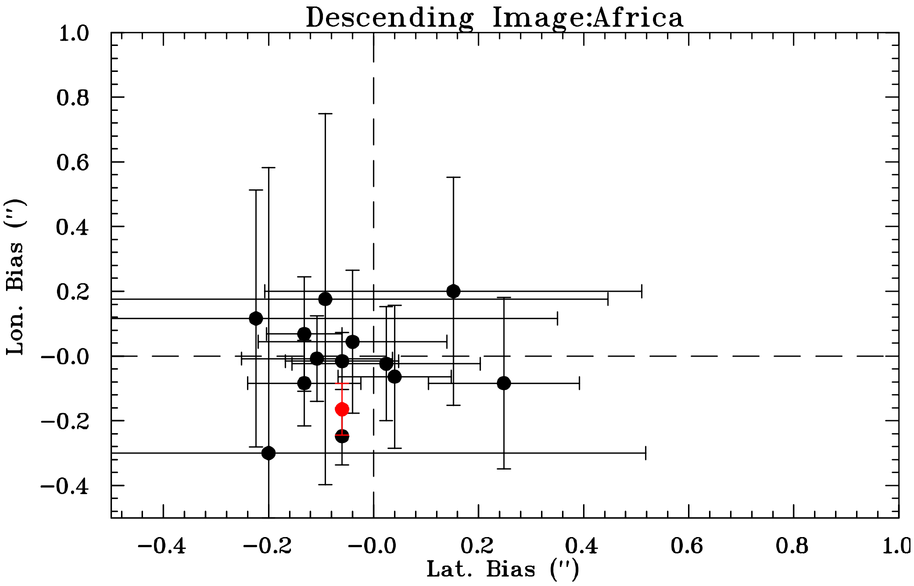

Figure 5.19: Best fit geolocation biases in descending image data using 10° by 10° super-cells in Africa.

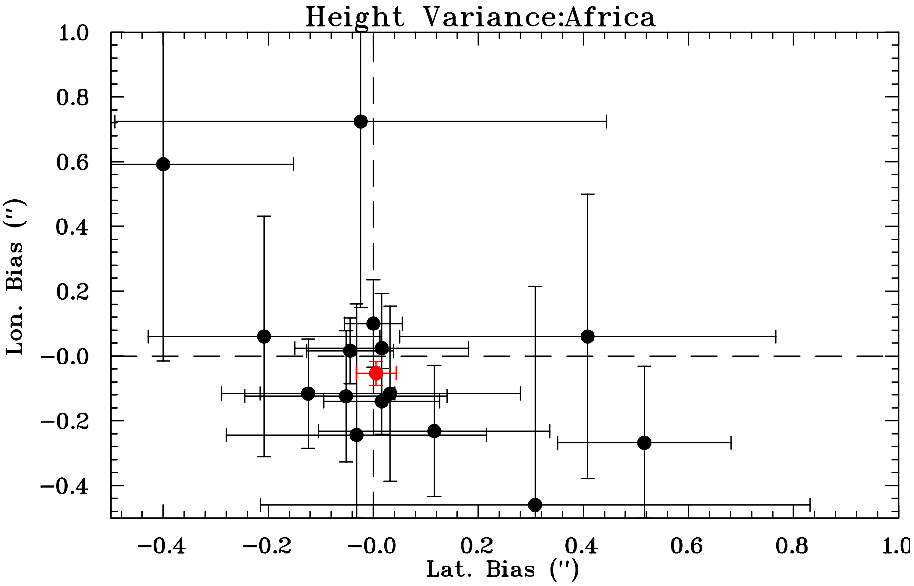

Figure 5.20: Best fit geolocation biases in DEM data using 10° by 10° super-cells in Africa.

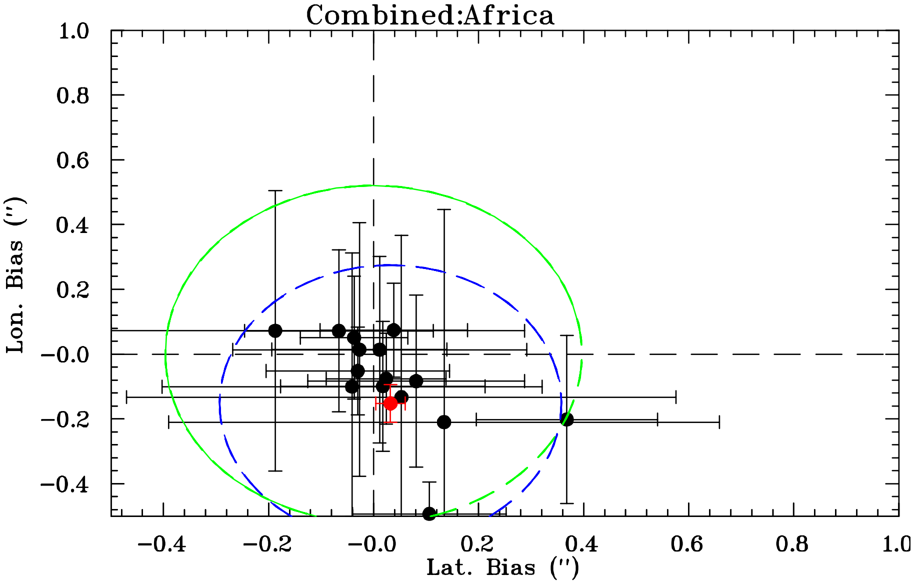

Figure 5.21: Best fit geolocation biases using combined height and image data for 10° by 10° super-cells in Africa. The 90% absolute (relative) limits are represented by the green (blue) circles.

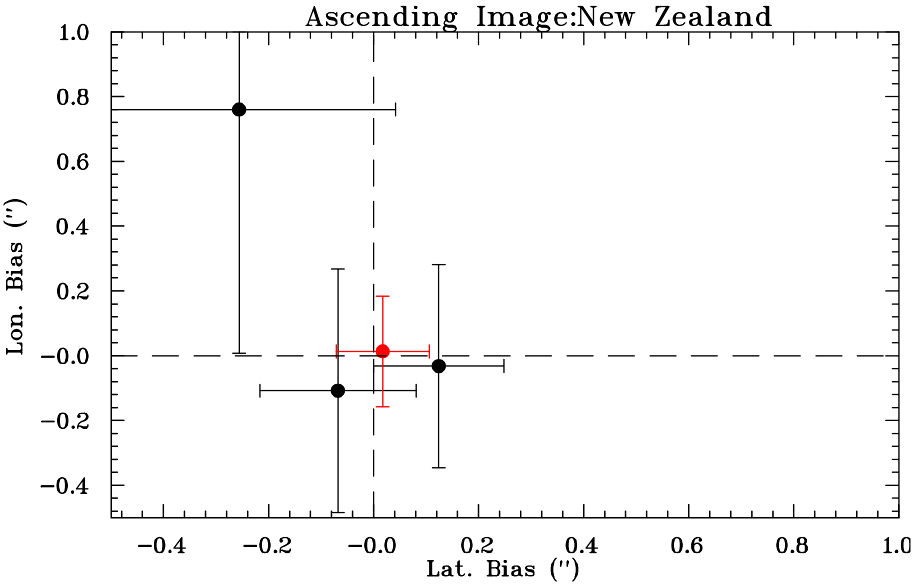

Figure 5.22: Best fit geolocation biases in ascending image data using 10° by 10° super-cells in New Zealand.

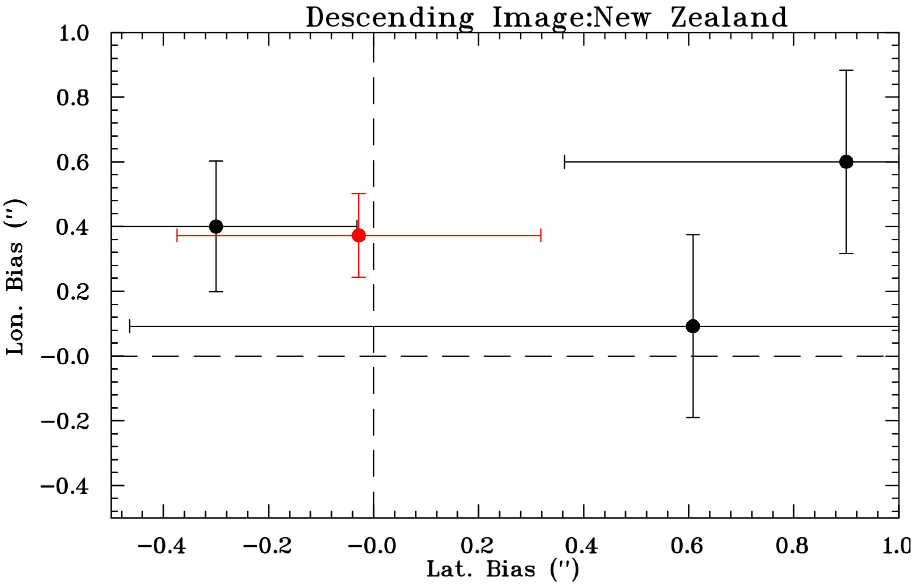

Figure 5.23: Best fit geolocation biases in descending image data using 10° by 10° super-cells in New Zealand.

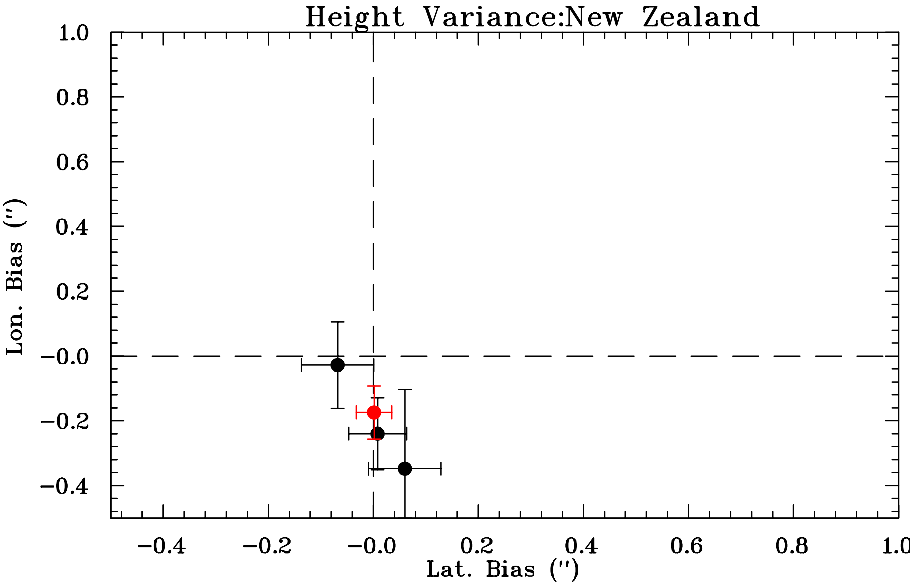

Figure 5.24: Best fit geolocation biases in DEM data using 10° by 10° super-cells in New Zealand.

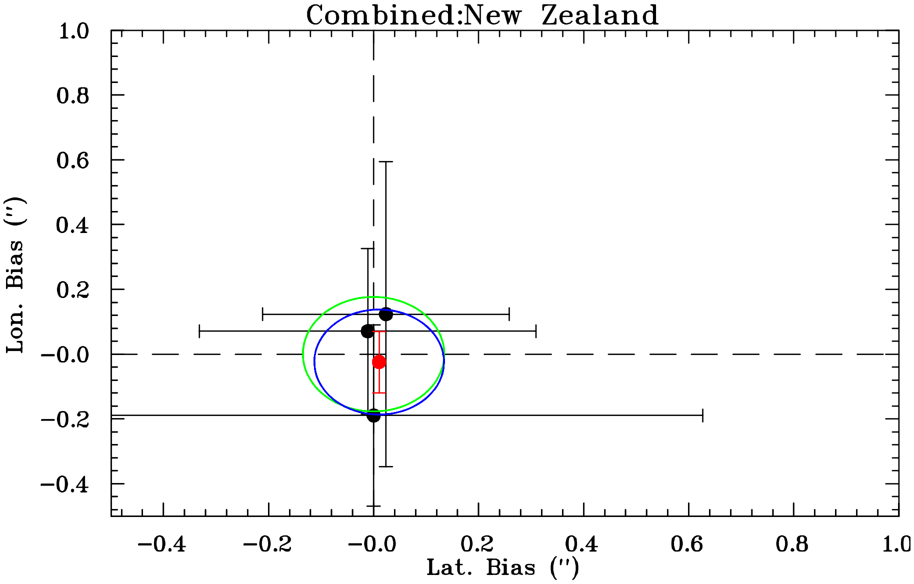

Figure 5.25: Best fit geolocation biases using combined height and image data for 10° by 10° super-cells in New Zealand. The 90% absolute (relative) limits are represented by the green (blue) circles.

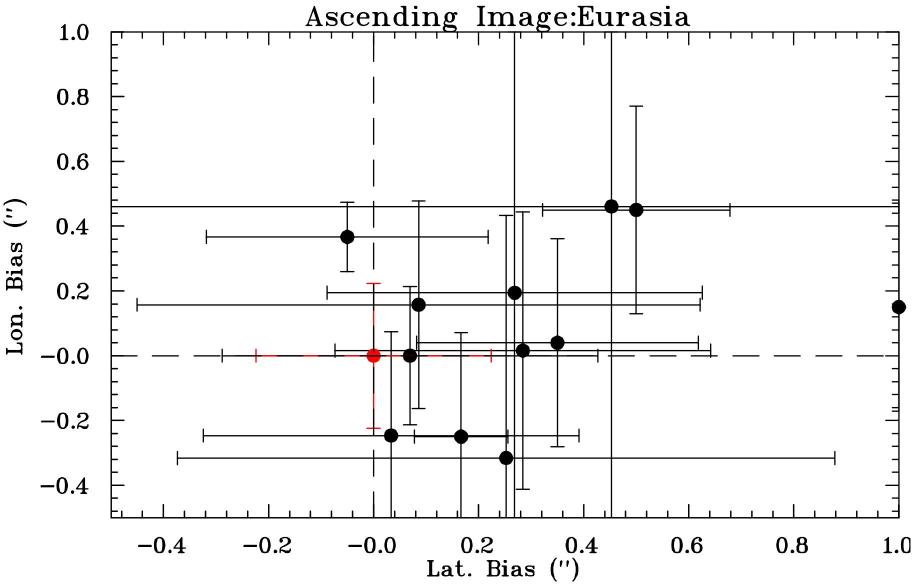

Figure 5.26: Best fit geolocation biases in ascending image data using 10° by 10° super-cells in Eurasia.

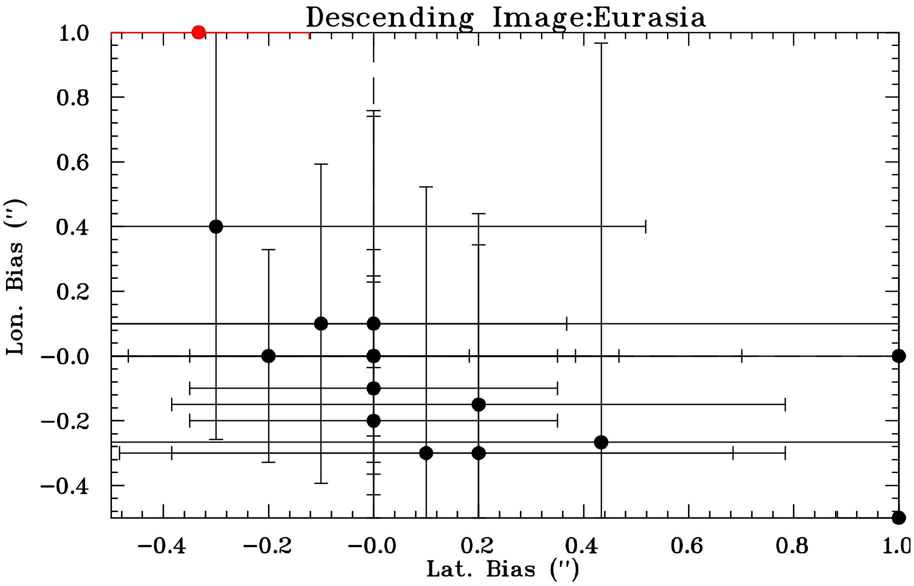

Figure 5.27: Best fit geolocation biases in descending image data using 10° by 10° super-cells in Eurasia.

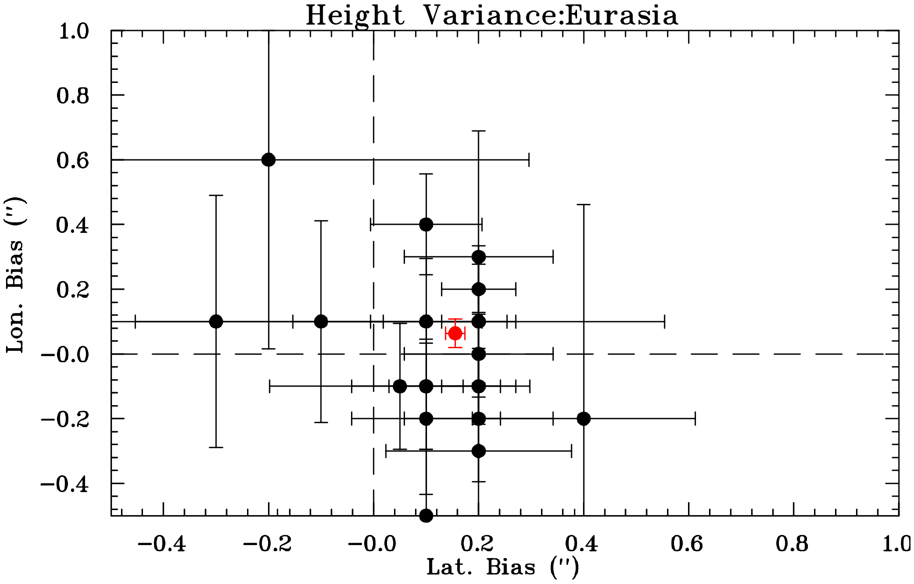

Figure 5.28: Best fit geolocation biases in DEM data using 10° by 10° super-cells in Eurasia.

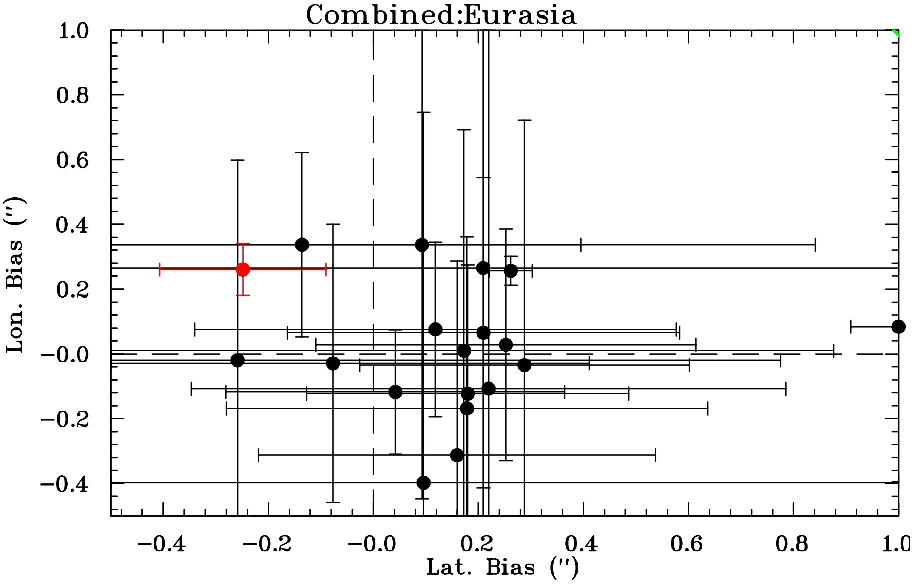

Figure 5.29: Best fit geolocation biases using combined height and image data for 10° by 10° super-cells in Eurasia. The 90% absolute (relative) limits are represented by the green (blue) circles.

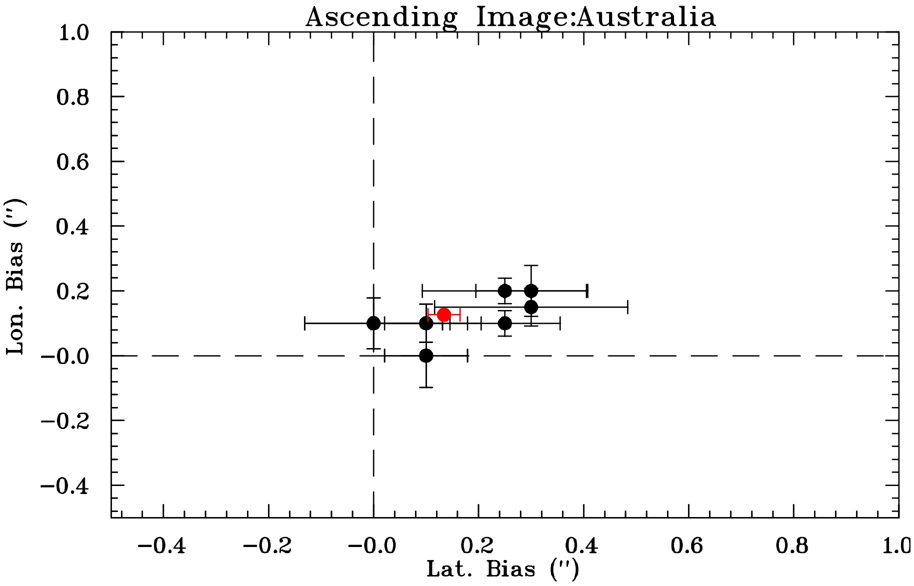

Figure 5.30: Best fit geolocation biases in ascending image data using 10° by 10° super-cells in Australia.

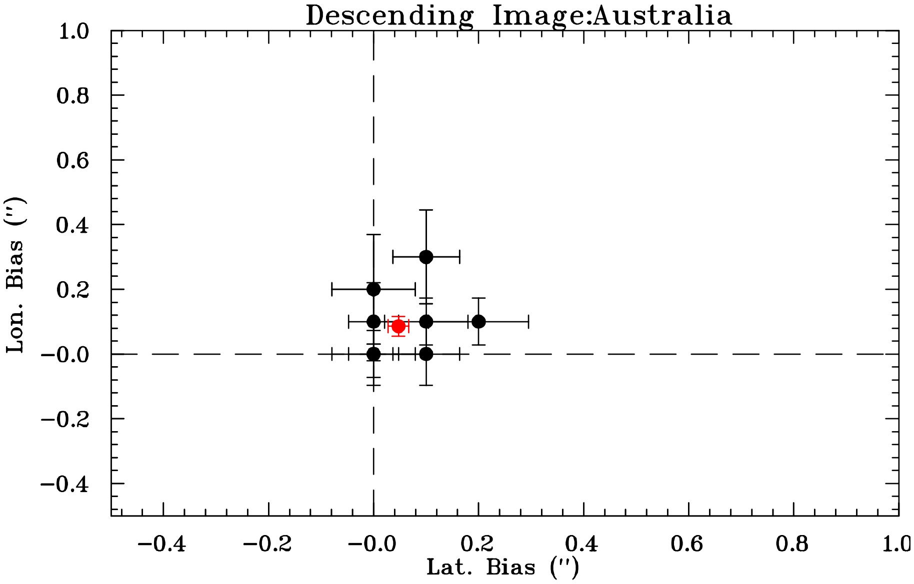

Figure 5.31: Best fit geolocation biases in descending image data using 10° by 10° super-cells in Australia.

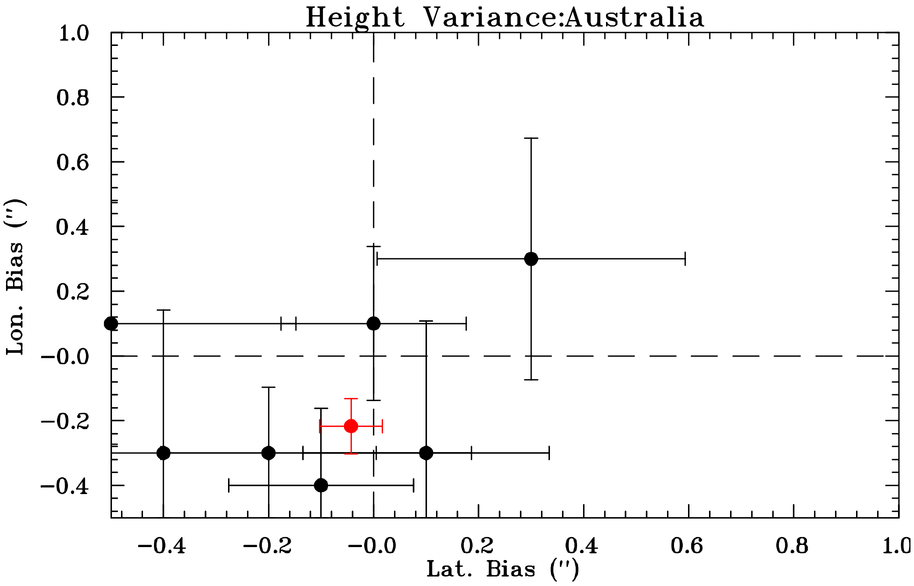

Figure 5.32: Best fit geolocation biases in DEM data using 10° by 10° super-cells in Australia.

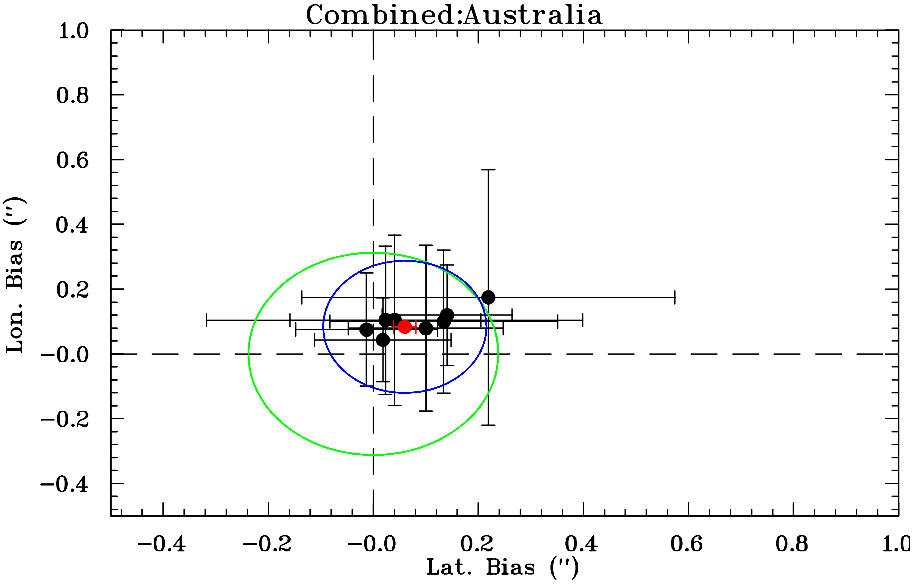

Figure 5.33: Best fit geolocation biases using combined height and image data for 10° by 10° super-cells in Australia. The 90% absolute (relative) limits are represented by the green (blue) circles.

Chapter 6

Comparison Against GeoSAR High Resolution DEM

6.1 Summary

The GeoSAR radar interferometer (http://southport.jpl.nasa.gov/html/projects/geosar/geosar.html) is an airborne X- and P-Band interferometer with an X-band 1 m to 3 m absolute height accuracy and a 0.5 m to 1.2 m relative height accuracy. The spatial height posting is 5 m. We have compared the SRTM height data collected over a portion of Santa Barbara County to a mosaic of GeoSAR data covering the same areas. The principal conclusions are below.

- Cross-correlation analysis between the SRTM and GeoSAR height data shows that the SRTM data are planimetrically correct to better than 1 0.00028° SRTM pixel.
- The SRTM DEM average height difference is 0.54 m. Over 90 % of the pixels have a difference of less than 6 m.
- Comparisons of the GeoSAR and SRTM data suggest that the SRTM data are posted at a finer spacing than the measurement spatial resolution. These results are consistent with those presented by Smith and Sandwell [2].

6.2 Discussion of GeoSAR and SRTM Data Used

One of the three sites used for GeoSAR calibration is located in Santa Barbara County. As part of the GeoSAR calibration activity, multiple data takes were collected at the site in 2001 and 2002. The site was instrumented with eight corner reflectors, and a photogrammetrically derived true ground surface DEM was provided which covers part of the data collection area.

The X-Band GeoSAR DEM that was used for this comparison was made by mosaicking the data from 6 data takes collected for GeoSAR calibration in mid-July 2002. GeoSAR is a dual sided imager, and data imaged from both sides of the aircraft were included in the mosaic. GeoSAR has two 160 MHz bandwidth data collection modes. Data from both of these high resolution data collection modes were used.

Valid Points	1111669
Maximum Difference (m)	40.16
Minimum Difference (m)	-68.94
Average Difference (m)	0.54
Standard Deviation (m)	3.32
Median Difference (m)	0.62

50 % of the SRTM-GeoSAR Height Differences are between -0.9 and 2.1 m
90 % of the SRTM-GeoSAR Height Differences are between -4.5 and 5.8 m

Table 6.1: Summary of height differences between SRTM and GeoSAR derived DEMs in Santa Barbara County, California

The DEM derived from each pass of GeoSAR data has a specified 1 sigma relative height accuracy of 1 m and an absolute height accuracy of 2.5 m averaged over the 10 km swath with 5 m postings. Since the DEM used for the comparison is a synthesis of multiple passes, the DEM is significantly more accurate than this in the areas covered by more than 1 data take. In addition, the statistical uncertainties have been reduced by averaging the GeoSAR data when the posting was increased from 5 m to 30 m for comparison with the SRTM data.

Figures 6.1 and 6.2 provide overview images of the 30 m GeoSAR data from Santa Barbara County. Much of the scene is covered by ocean, which is not suitable for comparison with the SRTM heights. Point Sal appears in the upper left corner of the images. The center of the images is dominated by the agricultural fields surrounding the Santa Ynez River near the town of Lompoc. North of the Santa Ynez River is San Antonio Creek and the vineyards of the Los Alamos valley. Point Arguello appears near the center of the bottom of the images. The scene shown is approximately 42 km by 36 km.

The SRTM 1° cell with a south west corner of 34° North and 121° West was downloaded from the USGS website. The only manipulations that were done to the data were to convert the data from integer to floating point and to remove the EGM96 geoid; thus, converting the data back to the reference WGS-84 ellipsoid to match the GeoSAR data. The GeoSAR data were reprojected to match the equiangular SRTM DEM.

6.3 GeoSAR/SRTM Comparison

The first comparison performed was to look for planimetric errors in the SRTM data. Cross correlations of the terrain were performed throughout the scene. This analysis revealed that the SRTM data was planimetrically correct to better than 1 SRTM pixel.

Next a pixel by pixel comparison of the height data was performed. Figure 6.3 shows a histogram of the pixel by pixel height differences between the SRTM and the GeoSAR heights. Table 6.1 provides the summary statistics of the pixel by pixel comparisons.

Images of the height differences reveal various interesting features of the SRTM height data. Figure 6.4 shows a section of the scene where there are buildings and planted lines of trees. Neither the GeoSAR X-Band data nor the SRTM C-Band data actually measure the true ground surface. In the areas with buildings, both DEMs show extremely similar heights. However, in the areas where

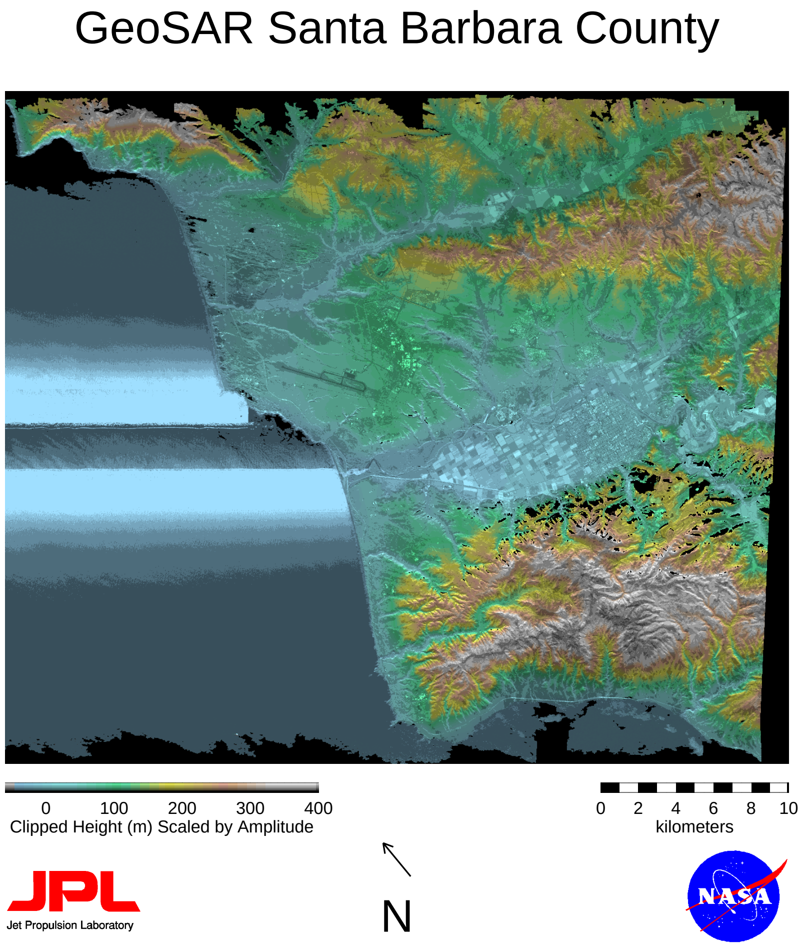

Figure 6.1: Overview image of GeoSAR data from Santa Barbara County, California. In this image, the radar backscatter overlays color which indicates the elevation. A single color wrap is used to show global elevation difference. Out of range height data is clipped to the plot end values.

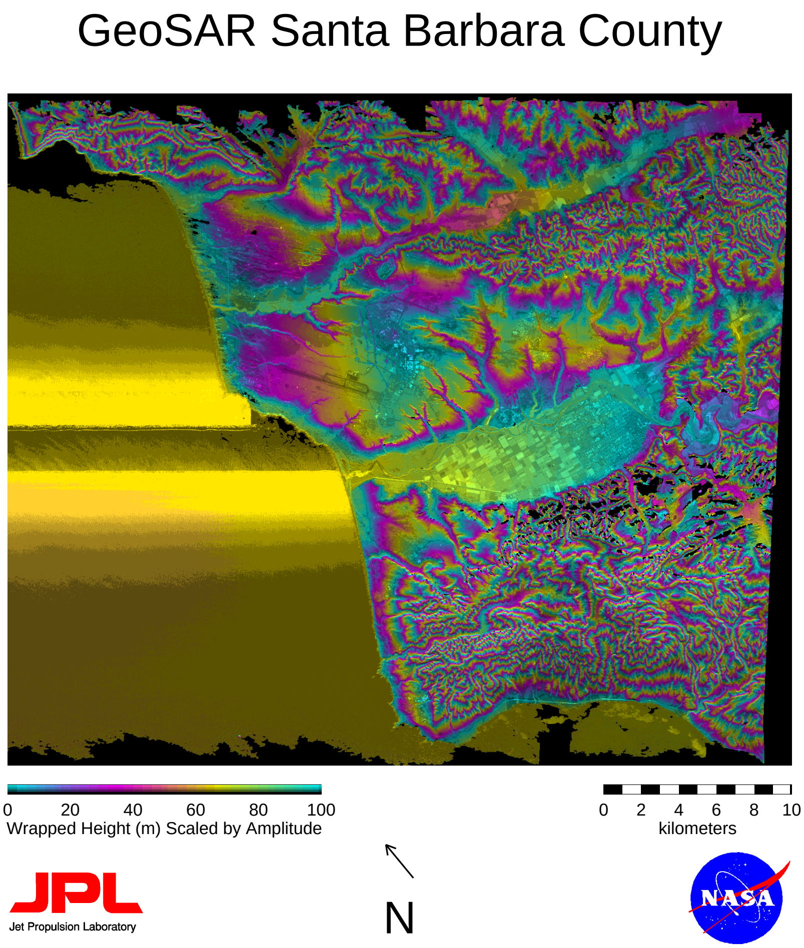

Figure 6.2: Overview image of GeoSAR data from Santa Barbara County, California. In this image, the radar backscatter overlays color which indicates the elevation. The colors repeat for every 100 m of elevation.

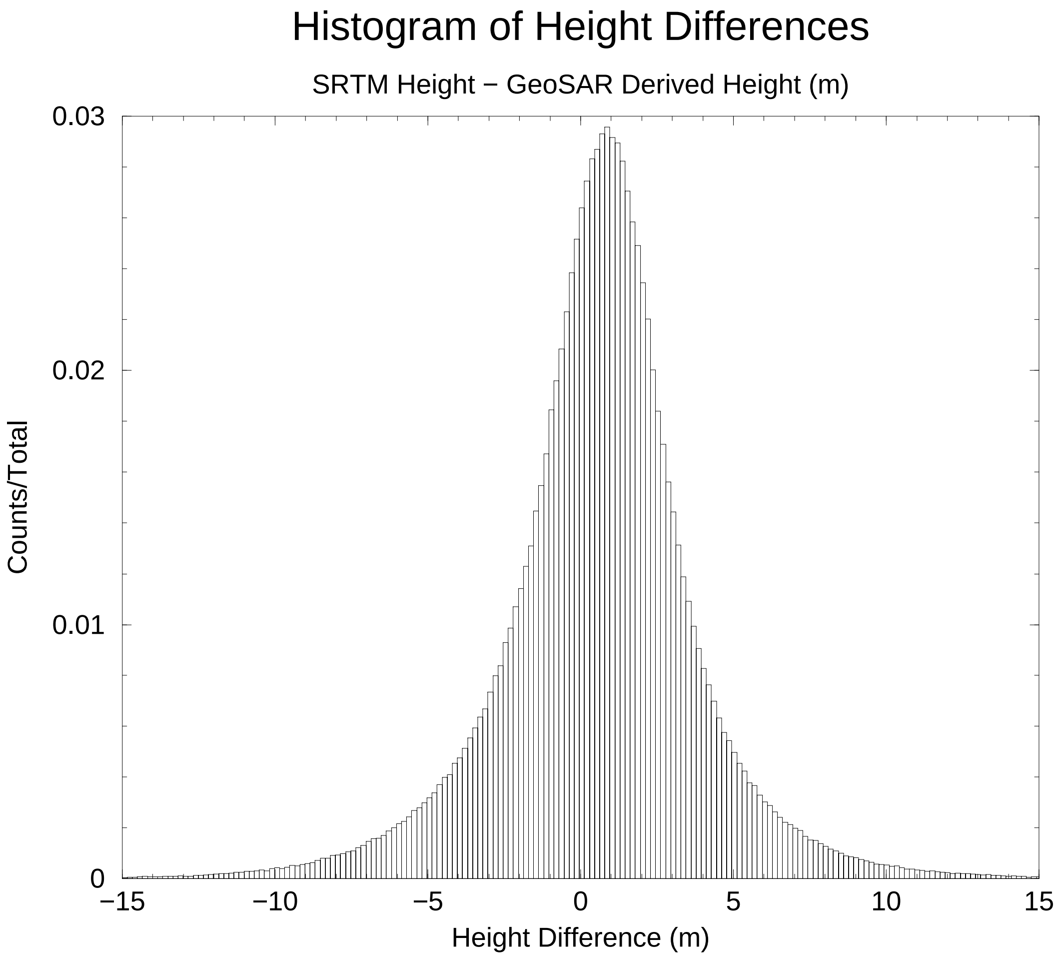

Figure 6.3: Histogram of pixel by pixel height differences between SRTM and GeoSAR derived DEMs in Santa Barbara County, California

there are trees, the heights differ significantly, up to 15 m, fundamentally because the regions with trees appear to be wider in the SRTM DEM.

The effects of vegetation are also shown in Figure 6.5 which shows a small section of the overall area compared. Figure 6.5 focuses on the area where the Santa Ynez River enters the Pacific Ocean south of Purisima Point. Both DEMs clearly show the ribbon of trees growing along the Santa Ynez river. However, the feature that jumps out in the comparison is the expected larger statistical height error of the SRTM data relative to the GeoSAR data. This is especially noticeable in the water at the extreme left of the image.

Figure 6.6 shows a section of the scene just north of Point Arguello where there is significant terrain. Looking at the height comparisons in this Figure it appears that the SRTM DEM does not have as high resolution as its planimetric posting. This is essentially the same conclusion we came to from viewing the lines of trees. This resolution issue is also brought out in Figure 6.7. The hill tops are sheared off and the valleys are not as deep in the SRTM data as in the GeoSAR data.

In order to probe the actual planimetric resolution of the SRTM data, we box car filtered the 30 m posted GeoSAR DEM data and then compared it on a point by point basis to the SRTM data. Figure 6.8 shows a histogram of the height differences with the GeoSAR DEMs with variable amounts of filtering. Of the cases tested, the standard deviation is the lowest when the GeoSAR data was smoothed using a 3x3 box car filter, giving the GeoSAR data an effective 45 m resolution, defining resolution as the separation such that the correlation between measurement errors drops by 0.5. If, instead of the half-power point definition of the resolution, one uses the first zero-crossing definition, the SRTM effective resolution would be 90 m. Figures 6.9, 6.10, 6.11, and 6.12 show the height differences for the whole mapped areas. The reduction in the standard deviation of the height differences can be seen by comparing the four images. In Figure 6.9, the height differences when compared with 30 m resolution GeoSAR data, lots of high frequency structure can be seen in the height difference map. In Figures 6.10 and 6.11 the high frequency structures are disappearing, and fewer pixels have large differences. In Figure 6.12,which displays the height differences when compared with 120 m resolution GeoSAR data,the image is starting to show small scale structures indicating that the GeoSAR data are now over smoothed.

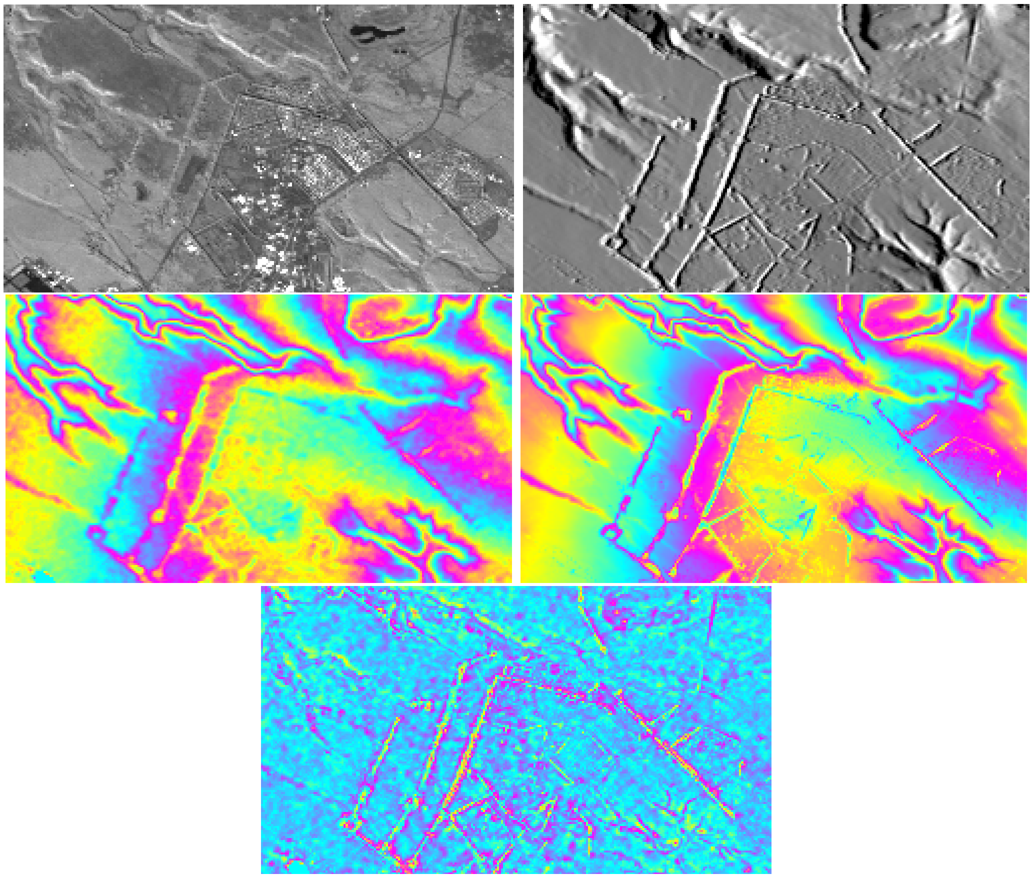

Figure 6.4: This figure consists of five views of the same small area of the scene. The area shown is approximately 7.5 km by 4.3 km. The upper left image is the X-Band GeoSAR backscatter amplitude image reduced to 30 m resolution and reprojected to match the SRTM data. The upper right image is a shaded relief of the GeoSAR DEM. The middle left image is the SRTM heights shown on a 40 m height wrap. The middle right image is the GeoSAR heights shown on a 40 m height wrap. The bottom is the SRTM-GeoSAR height difference shown on a 20 m height wrap.

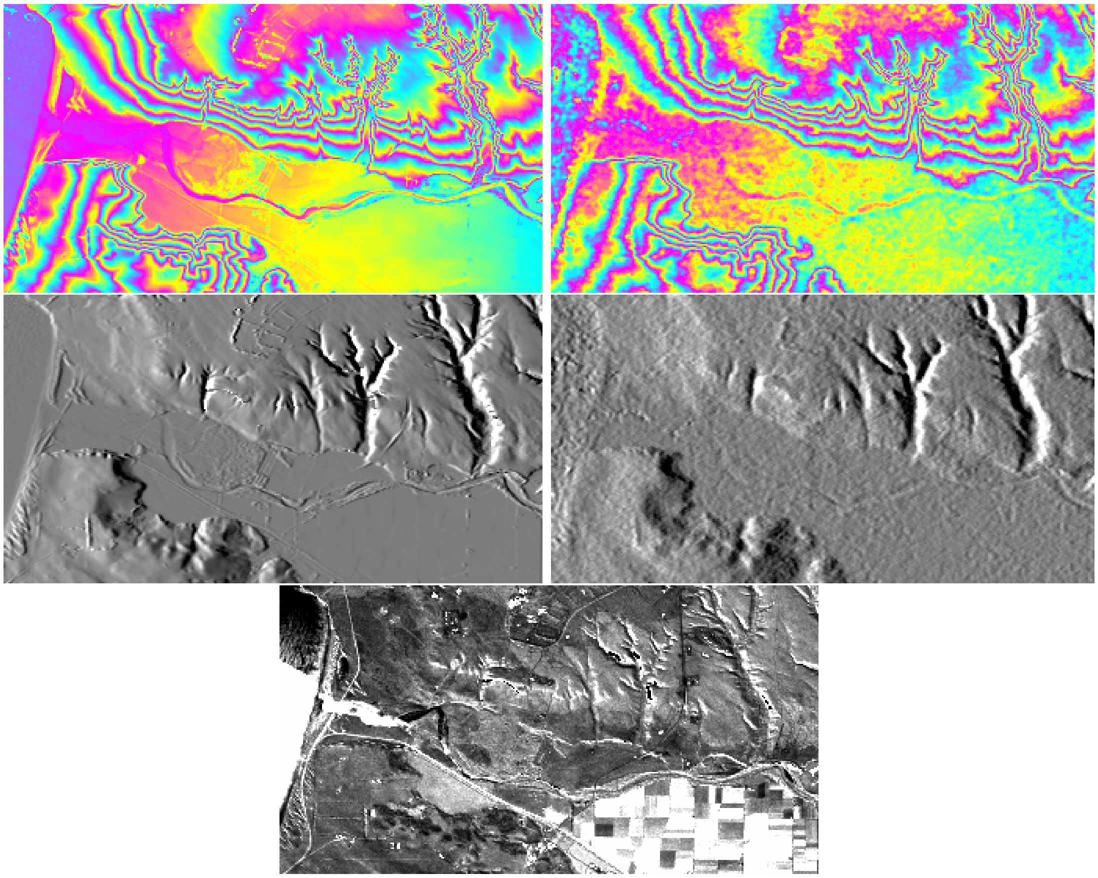

Figure 6.5: G

eoSAR heights, and he SRTM-GeoSAR height difference] This figure consists of five views of the same small area of the scene. The area shown is approximately 1.7 km by 0.9 km. The upper left image is the X-Band GeoSAR height map reduced to 30 m resolution and reprojected to match the SRTM data and shown with a 20 m height wrap. The upper right image is the SRTM height data shown the same way. The center left image is a shaded relief of the GeoSAR heights. The center right image is a shaded relief of the SRTM heights. The bottom image is the GeoSAR amplitude image.

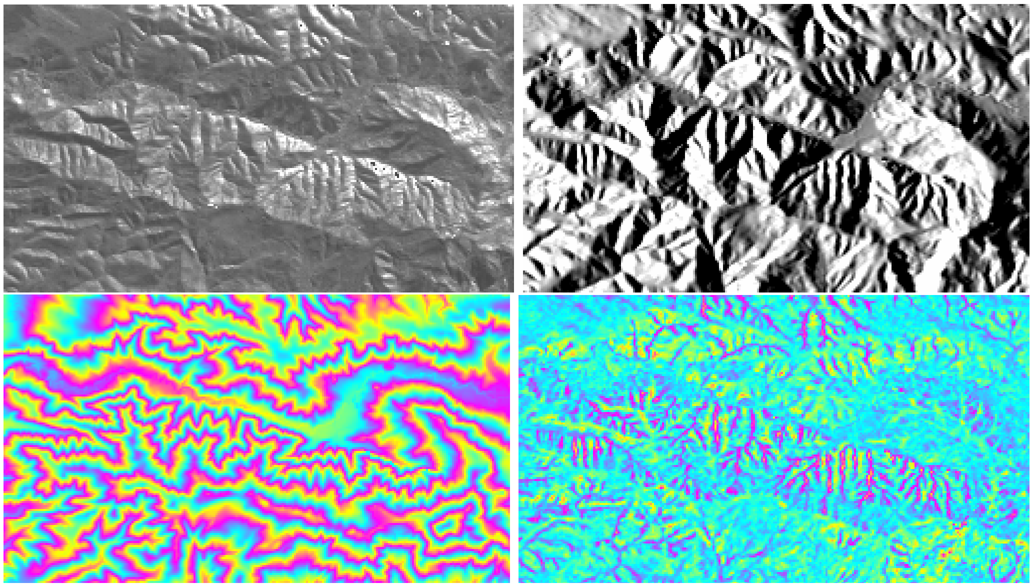

Figure 6.6: This figure consists of four views of the same small area of the scene. The area shown is approximately 7.5 km by 4.3 km. The upper left image is the X-Band GeoSAR backscatter amplitude image reduced to 30 m resolution and reprojected to match the SRTM data. The upper right image is a shaded relief of the GeoSAR DEM. The bottom left image is the GeoSAR heights shown on a 100 m height wrap. The bottom right image is the SRTM-GeoSAR height difference shown on a 35 m height wrap.

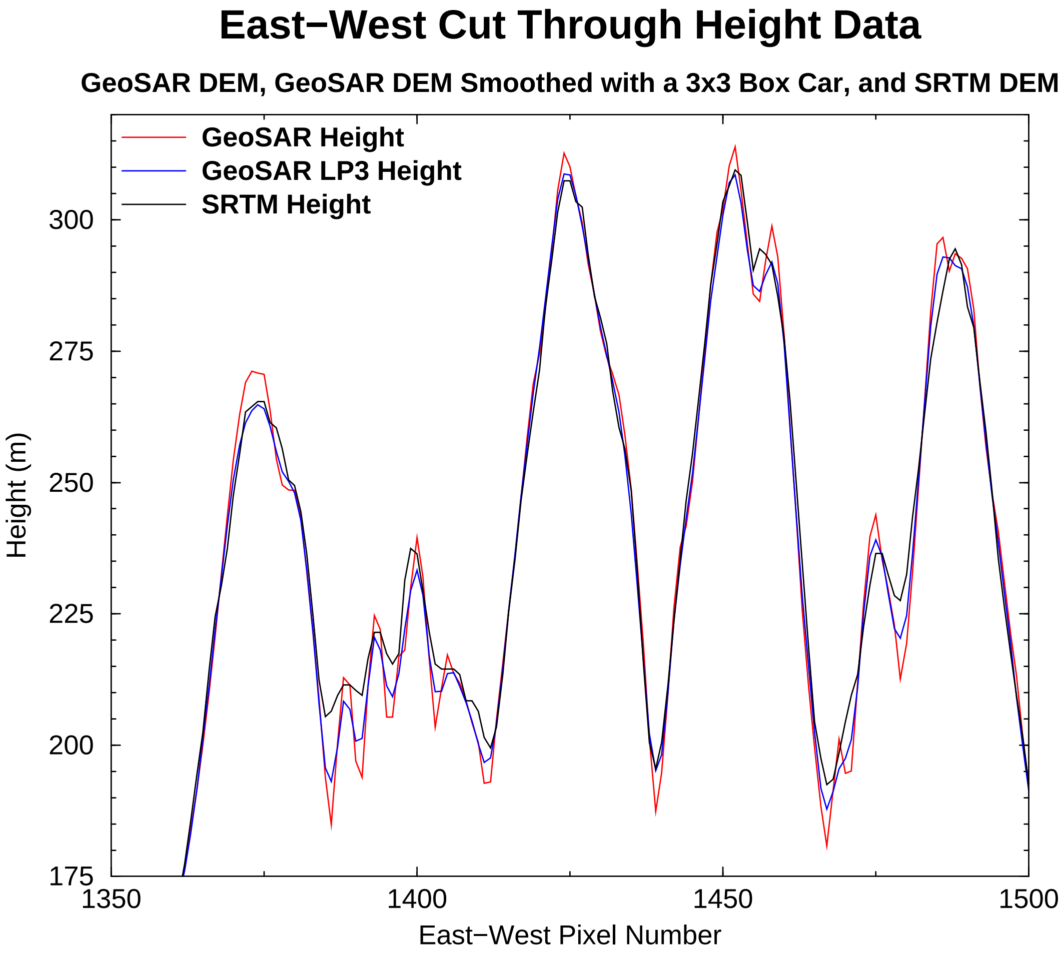

Figure 6.7: Line cuts through the SRTM and GeoSAR DEMs. The red line indicates the height in the GeoSAR 30 m DEM, the black line indicates the height in the SRTM 30 m data, and the blue curve is the cut through a version of the GeoSAR DEM that has been filtered with a 3x3 box car.

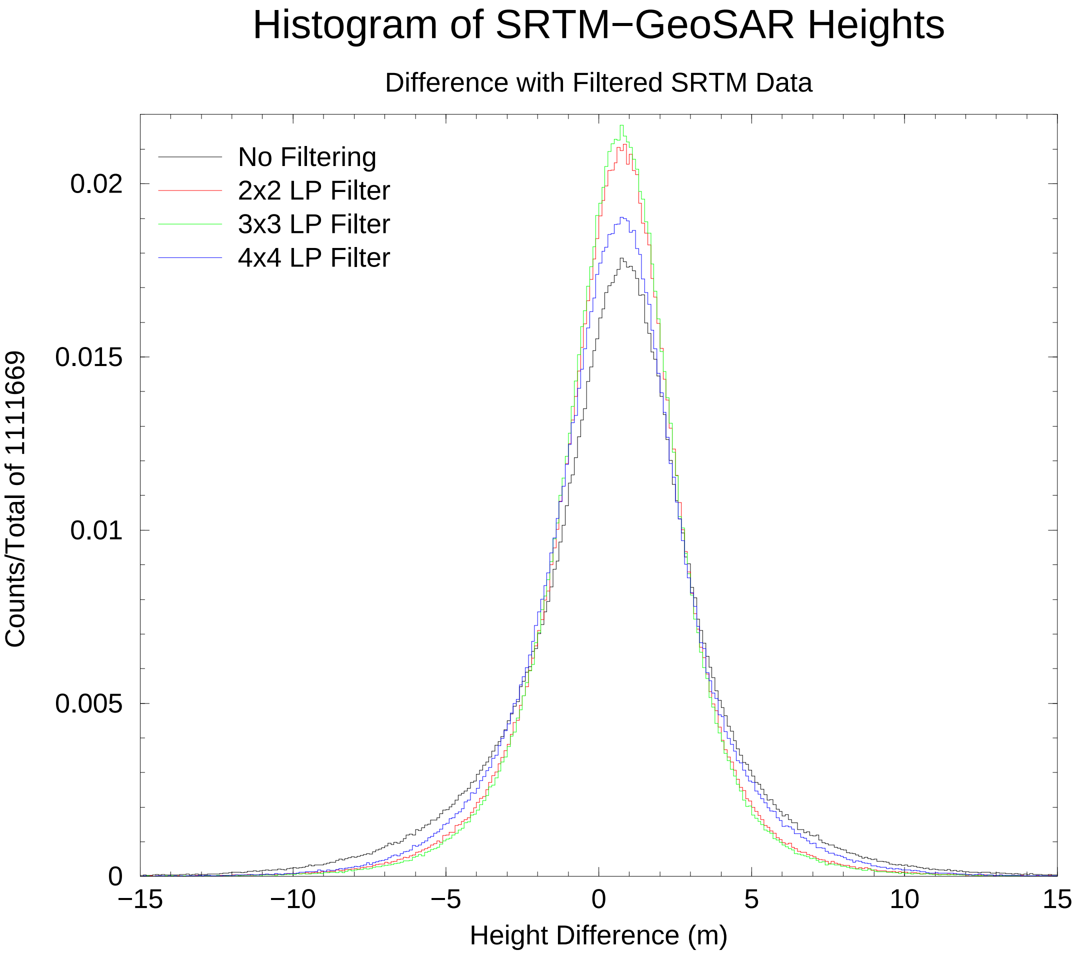

Figure 6.8: Histogram of pixel by pixel height differences between SRTM and GeoSAR derived DEMs in Santa Barbara County, California. Each curve represents the difference between the SRTM data and the GeoSAR data with a different amount of filtering applied to the GeoSAR data. For the red curve, a 2 pixel by 2 pixel low pass filter was applied to the GeoSAR data. A 3 pixel by 3 pixel filter was used for the green curve, and a 4 pixel by 4 pixel filter was used for the blue curve.

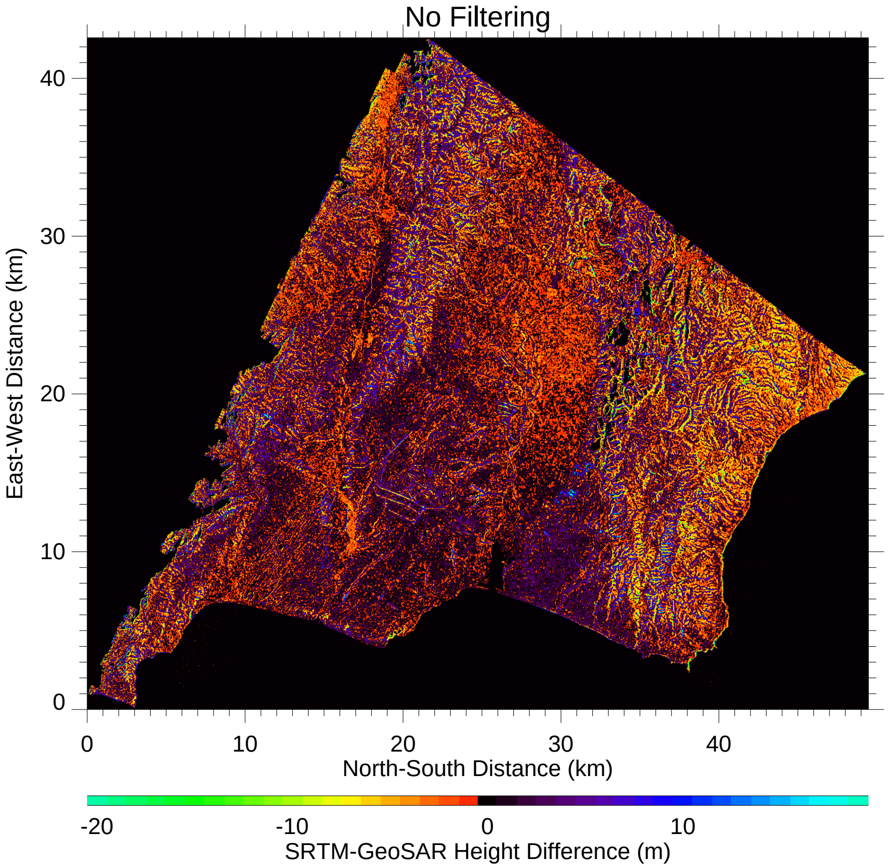

Figure 6.9: W
rapped height differences between the SRTM and GeoSAR derived DEMs in Santa Barbara County, California] Wrapped height differences between the SRTM and GeoSAR derived DEMs in Santa Barbara County, California. For example, yellow pixels correspond to the GeoSAR data being approximately 8 m higher than the SRTM data, and blue pixels correspond to the SRTM data being approximately 10 m higher than the GeoSAR data.

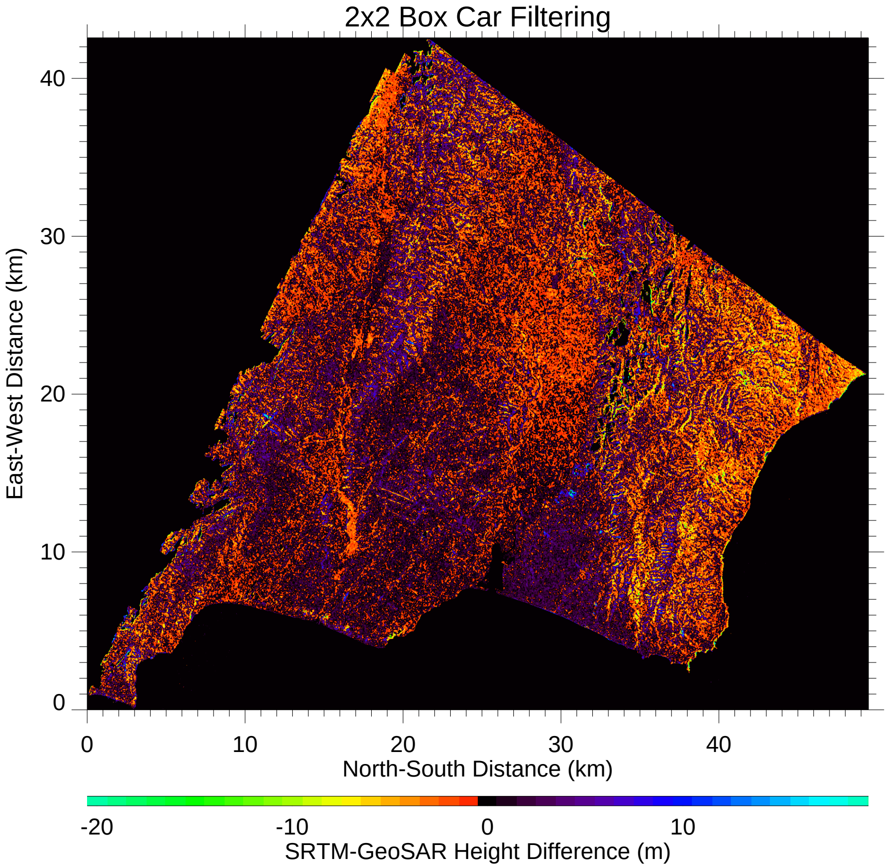

Figure 6.10: Wrapped height differences between the SRTM and GeoSAR derived DEMs in Santa Barbara County, California. For this comparison the GeoSAR data have been filtered using a 2x2 box car filter.

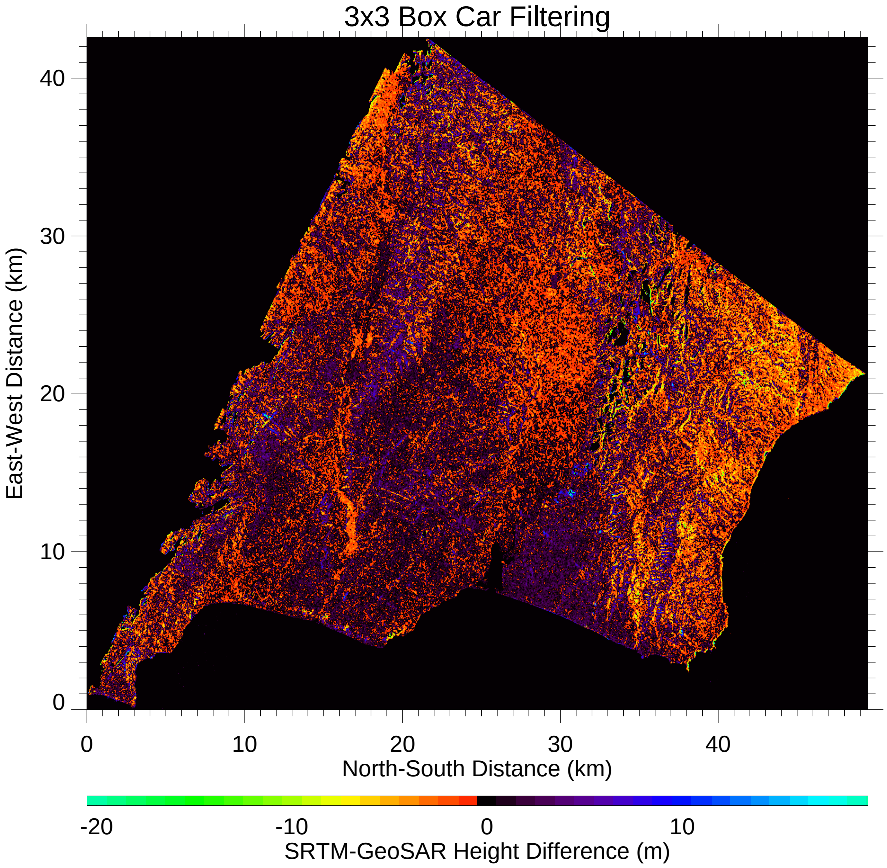

Figure 6.11: Wrapped height differences between the SRTM and GeoSAR derived DEMs in Santa Barbara County, California. For this comparison the GeoSAR data have been filtered using a 3x3 box car filter.

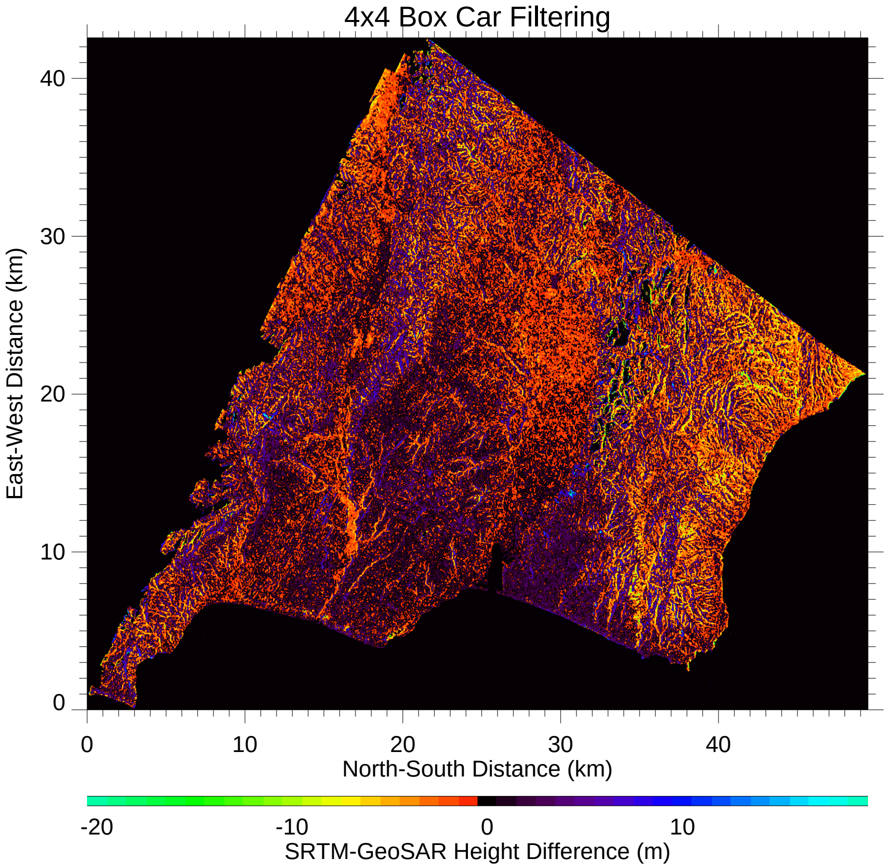

Figure 6.12: Wrapped height differences between the SRTM and GeoSAR derived DEMs in Santa Barbara County, California. For this comparison the GeoSAR data have been filtered using a 4x4 box car filter.

Acknowledgements

This work was conducted by the Jet Propulsion Laboratory, California Institute of Technology, under contract with the National Aeronautics and Space Administration (NASA). A data comparison of this magnitude is the work of many people across many continents, of whom we cannot acknowledge only a few since, in many cases, we do not know their names. In addition to these many field workers, we would like to give special thanks to AUSLIG, Anthony Milne (UNSW), Catherine Ticehurst (CSIRO), Alex Held (CSIRO), John Homer (U. Queensland) in Australia for their invaluable help in collecting ground truth data in adverse conditions. In Argentina, we would like to acknowledge the Instituto Geográfico Militar for their help in collecting Kinematic GPS data. In NIMA, now NGA, we would like to thank all the people who made the kinematic GPS data collections possible and provided us with ground truth data. In particular, we would like to thank Paul Salamanowicz, James Slater, and Barry Heady for their help and support. At Ohio State University, we would like to thank C.K. Shum and his team with their help regarding ocean tides. At JPL, we would like to thank Frank Webb (Kinematic GPS), Paul Rosen (SRTM Algorithm development), Yunjin Kim (SRTM project manager), Tom Farr and Mike Kobrick (Science), David Perz, Joanne Shimada, and Brian Swift (Operational Processing), Eric Gurrola, Brian Pollard, Ali Safaeinili, and Marc Simard, Jonathan Meager, Ziad Haddad (Ground Truth Experiments), and all the other talented engineers and scietists who made SRTM and this study possible. Finally, we would like to thank Paul Rosen (JPL) and James Slater (NGA) for a close reading of the report and their many helpful suggestions.

Bibliography

[1] J. van Zyl, “The shuttle radar topography mission (srtm): A breakthrough in remote sensing of topography,” *ACTA ASTRONAUTICA*, vol. 48, no. 5-12, pp. 559–565, 2001.

[2] B. Smith and D. Sandwell, “Accuracy and resolution of shuttle radar topography mission data,” *GEOPHYSICAL RESEARCH LETTERS*, vol. 30, May 2003.

[3] G. Sun, K. Ranson, V. Khairuk, and et al., “Validation of surface height from shuttle radar topography mission using shuttle laser altimeter,” *REMOTE SENSING OF ENVIRONMENT*, vol. 88, pp. 401–411, December 2003.

[4] C. Tierny, L. Kantha, and G. Born, “Shallow and deep water global ocean tides from altimetry and numerical modeling,” *J. Geophys. Res.*, vol. 105, pp. 11,259–11,277, May 2000.

[5] E. Rodríguez and J. M. Martin, “Theory and design of interferometric synthetic aperture radars,” *IEE Proc.-F*, vol. 139, no. 2, pp. 147–159, 1992.

[6] P. Rosen, S. Hensley, I. Joughin, F. Li, S. Madsen, E. Rodriguez, and R. Goldstein, “Synthetic aperture radar interferometry - invited paper,” *PROCEEDINGS OF THE IEEE*, vol. 88, no. 3, pp. 333–382, 2000.

[7] F. Gatelli, A. Monti-Guarnieri, F. Parizzi, P. Pasquali, C. Prati, and F. Rocca, “The wavenumber shift in SAR interferometry,” *IEEE Trans. Geosci. Remote Sensing*, vol. 32, no. 4, pp. 855–865, 1994.

[8] S. Hensley, “Origin of the low srtm height error estimates,” tech. rep., Jet Propulsion Laboratory, June 2002. JPL Technical Memorandum.

Appendix A

SRTM Error Characteristics

A.1 Introduction

The purpose of this appendix is to derive the error model for the SRTM measurements in terms of the quantities measured by the AODA and the interferometer, rather than derived quantities, such as the interferometric baseline. This will aid in conducting system trade-offs and in obtaining the calibration and verification error models which will allow for inversion of the instrument parameters.

Throughout this appendix, a geometric, rather than coordinate system dependent, approach will be presented. This will aid in the understanding of the geometric nature of the interferometric errors, as well as provide more compact formulas which are independent of conventions, such as the Euler angle orders. The presentation uses some concepts such as dyadic operators in order to obtain cleaner expressions for the sensitivities. A brief review of these techniques is presented in Appendix C, for those who are unfamiliar with them.

In the first section, we review the geometry of the measurement system and establish our conventions. The second section examines the effect of AODA measurement errors on the baseline and position of the inboard antenna phase center. The third section reviews the interferometric equations, while the fourth discusses the general geometric characteristics of the measurement errors. Finally, in the sixth section we derive the final formulas for the measurement error model.

A.2 Description of SRTM Geometry Measurements

In order to tie in the interferometric measurement to an Earth-fixed coordinate system (which will be assumed to be WGS84 henceforth), it is necessary to provide measurements in this coordinate system of three vectors: 1) the interferometric baseline vector, **B**, defined as the vector from the phase center of the inboard antenna to the phase center of the outboard antenna; 2) a vector, **P**, from the origin of the Earth-fixed coordinate system to the phase center of the inboard antenna; and, 3) the platform velocity vector, $\mathbf{V} = \dot{\mathbf{P}}$. An additional parameter, the time-tag τ, associates with each measurement a position in the along track direction.

The AODA subsystem provides these measurements using the geometry shown in Figure A.1. The measurements made by the current AODA baseline system are as follows:

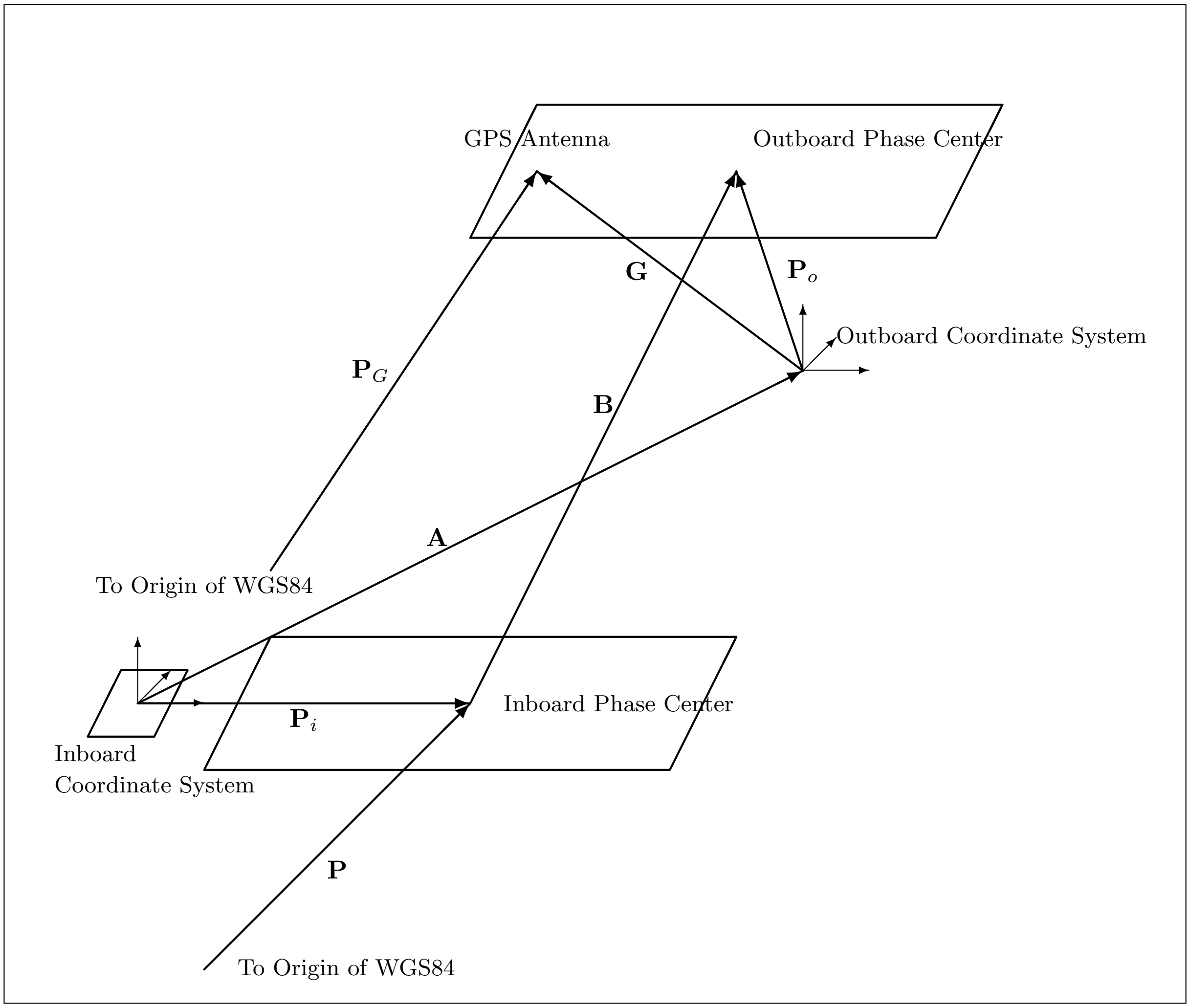

Figure A.1: SRTM Measurement Geometry

- $\mathbf{P}_G$ is a vector from the Earth-fixed frame to a GPS receiver located in the outboard antenna assembly, measured in an Earth-fixed coordinate system. (By convention, all vectors will be written in **bold** type).

- $\mathbf{G} = G\hat{\mathbf{g}}$ is a vector from the origin of the outboard coordinate system to the GPS receiver, measured relative to the outboard coordinate system. The measurement of its magnitude, G, will be made prior to launch. The unit vector $\hat{\mathbf{g}}$ (by convention, all unit vectors will be written as bold lower case letters with hats) is tied in to the outboard coordinate system, and will rotate when this coordinate system rotates.

  Measurements of the of rotation of the outboard coordinate system relative to the inboard coordinate system are performed by the AODA camera, located close to the origin of the inboard coordinate system. We will denote the rotation operator taking the outboard system into the inboard system by $\mathbf{M}_{\mathrm{OCS}}^{\mathrm{ICS}}$ and write it in terms of a rotation vector $\mathbf{\Omega}_o^i$ as

$$\mathbf{M}_{\mathrm{OCS}}^{\mathrm{ICS}} = \exp\left[\mathbf{\Omega}_o^i \times\right] \equiv \mathbf{1} + \mathbf{\Omega}_o^i \times + \frac{1}{2}\mathbf{\Omega}_o^i \times \left(\mathbf{\Omega}_o^i \times\right) + \ldots \tag{A.1}$$

  Any arbitrary rotation, $\mathbf{\Omega} = \Omega\ \hat{\omega}$ can be written in this way: Ω, gives the magnitude of the rotation angle, and $\hat{\omega}$, a unit vector perpendicular to the plane of rotation, gives the orientation. These two quantities define three independent parameters (a magnitude and two direction cosines) which are equivalent to the Euler angles. Specifying rotations in this way, however, is independent of coordinate system, Euler angle sequence, etc., and simplifies considerably subsequent analysis and the resulting measurement error formulas.

- $\mathbf{P}_o = P_o\hat{\mathbf{p}}_o$ is a vector from the origin of the outboard coordinate system to the phase center of the outboard antenna, measured relative to the outboard coordinate system. It is measured in a similar way to $\mathbf{G}$, and the same comments apply.

- $\mathbf{A} = A\hat{\mathbf{a}}$ is a vector from the origin of the inboard coordinate system to the origin of the outboard coordinate system. The unit vector $\hat{\mathbf{a}}$ is measured by the AODA camera located near the origin of the inboard coordinate system. The magnitude A will be either measured by a laser ranging system, or modeled.

  This vector is measured relative to the inboard coordinate system. The rotation operator which relates the inboard coordinate system to the Earth-fixed system will be denoted by $\mathbf{M}_{\mathrm{ICS}}^{\mathrm{WGS}}$, and the associated rotation vector by $\mathbf{\Omega}_i^w$. The rotation necessary to go from the inboard coordinate system to the Earth-fixed coordinate system is accomplished using the star trackers located close to the origin of the inboard coordinate system.

  Notice that to go from the outboard coordinate system to the Earth-fixed system, the rotation operator is given by

$$\mathbf{M}_{\mathrm{OCS}}^{\mathrm{WGS}} = \mathbf{M}_{\mathrm{ICS}}^{\mathrm{WGS}} \cdot \mathbf{M}_{\mathrm{OCS}}^{\mathrm{ICS}} \tag{A.2}$$

- $\mathbf{P}_i = P_i\hat{\mathbf{p}}_i$, a vector from the origin of the inboard coordinate system to the phase center of the inboard antenna. The magnitude P_i will be measured prior to launch, while the direction $\hat{\mathbf{p}}_i$ is tied to the orientation of the inboard coordinate system relative to the Earth-fixed coordinate system.

Given these measurements, the interferometric baseline and the position of the inboard antenna phase center are given by:

$$\mathbf{B} = \mathbf{A} - \mathbf{P}_i + \mathbf{P}_o \tag{A.3}$$

$$\mathbf{P} = \mathbf{P}_G - (\mathbf{G} + \mathbf{A} - \mathbf{P}_i) \tag{A.4}$$

The platform velocity vector $\mathbf{V}$ is measured using a mixture of an inertial navigation unit located near the origin of the inboard coordinate system and velocity estimates derived from the GPS measurements. It is thus a mixture of measurements taken using the inboard and Earth-fixed frames. To complicate matters even further, the velocity used for processing is not necessarily the instantaneous velocity, but rather the velocity of a reference track obtained by fitting the true displacement over a period of time. The major assumption made in this memo will be that errors in this reference velocity are independent from errors in the interferometric baseline. Notice that this assumption is not correct if the velocity is measured solely using inertial methods in the inboard platform: in that case an error in the inboard platform orientation translates into an error in the orientation of the velocity vector due to errors in the rotation operator $\mathbf{M}_{\mathrm{ICS}}^{\mathrm{WGS}}$.

In the previous paragraphs, we have presented the integrated AODA measurements, rather than the raw AODA measurements. A more detailed traceback to the raw measurements is obtained by examining the measurement of the vector $\mathbf{A}$ in detail. $\mathbf{A}$ is composed of a vector from the ICS to the baseline attitude determination camera, $\mathbf{C}$, a vector from the camera to the center of the outboard LED target array, $\mathbf{L}$, and a vector from the center of the outboard target array to the OCS, $\mathbf{O}$.

$$\mathbf{A} = \mathbf{C} + \mathbf{L} + \mathbf{O}$$

The vector $\mathbf{L}$ will probably be obtained by separate measurements of the vector direction $\hat{\mathbf{l}}$ by the baseline attitude determination camera, and a measurement of the magnitude of $\mathbf{L}$ obtained by the laser ranger. The laser ranger itself does not measure $|\mathbf{L}|$, but the distance from the laser ranger to the ranger target, which we denote by $\mathbf{D}$. In order to relate this to $\mathbf{L}$, we must introduce the lever arms from the camera to the ranger, $\mathbf{D}_C$, and the lever arm from the ranger target to the center of the LED array, $\mathbf{D}_L$, and write the range measurement as

$$|\mathbf{L}| = |\mathbf{D} + \mathbf{D}_C + \mathbf{D}_L|$$

In the following section, we will not examine in detail the error propagation at this finer level for two reasons: 1) the lever arms involved are small and static, and do not make a major contribution to the eror budget; 2) examination at the finer scale does not provide any additional understanding, but clutters up the presentation. If the error budget needs to be broken down at this finer level, one simply performs linear propagation of errors starting from the formulas derived in the following sections.

A.3 Propagation of Geometric Measurement Errors

In this section, we study how errors in the measured vectors $\mathbf{A}$, $\mathbf{G}$, $\mathbf{P}_o$, $\mathbf{P}_i$, and $\mathbf{P}_G$ propagate to errors in $\mathbf{B}$ and $\mathbf{P}$. It will be assumed that these quantities will be known well enough so that the calculation accurate to first order in the magnitude of the rotation angle errors will be sufficient. This assumption is justified by noting that the position errors introduced by including the effects of second order rotations are, in the worst case, of order $\delta P \leq \mathcal{O}(R_i \delta\theta^2)$, as we will see later on when discussing the interferometric equations. Assuming a range R_i of 400 km and an angular error of $\delta\theta = 11$ arcsec, the error in the position will be $\delta P \leq 1$ mm, and can be neglected.

This fact simplifies the analysis considerably since the error associated with a vector $\mathbf{v}$ by an error in the estimated rotation about its origin, is given by

$$\delta\mathbf{v} = \delta\Omega\, \hat{\omega} \times \mathbf{v} \tag{A.5}$$

where $\delta\Omega$ is the error in the rotation angle magnitude and $\hat{\omega}$ specifies the orientation of the rotation error. In particular, this greatly simplifies the consideration of the effects of the composition of transformations (e.g., the transformation from OCS to WGS coordinates). The first order error associated with two rotation errors is given by

$$\begin{aligned} \delta\mathbf{v} &= (\mathbf{1} + \delta\Omega_1\, \hat{\omega}_1 \times)(\mathbf{1} + \delta\Omega_2\, \hat{\omega}_2 \times)\mathbf{v} - \mathbf{v} \\ &\approx \delta\Omega_1\, \hat{\omega}_1 \times \mathbf{v} + \delta\Omega_2\, \hat{\omega}_2 \times \mathbf{v} \end{aligned} \tag{A.6}$$

i.e., first order rotation errors commute, and may therefore be considered independently.

We now consider the different sources of error:

1. **Errors due to Uncertainty in the ICS Attitude Relative to WGS:** From the discussion above, and using equations (A.3), (A.4), (A.5), we can write the effect due to an attitude error $\delta\Omega_i^w\, \hat{\omega}$ as

$$\delta\mathbf{B} = \delta\Omega_i^w\, \hat{\omega}_i^w \times \mathbf{B} \tag{A.7}$$

$$\delta\mathbf{P} = \delta\Omega_i^w\, \hat{\omega}_i^w \times (\mathbf{P} - \mathbf{P}_G) \tag{A.8}$$

   where we have used the fact that $\mathbf{P}_G$ is independent of the ICS.

2. **Errors due to Uncertainty in the OCS Attitude Relative to the ICS:** This measurement is made by the inboard imaging system. Noting that only $\mathbf{G}$ and $\mathbf{P}_o$ are affected, we can write

$$\delta\mathbf{B} = \delta\Omega_o^i\, \hat{\omega}_o^i \times \mathbf{P}_o \tag{A.9}$$

$$\delta\mathbf{P} = -\delta\Omega_o^i\, \hat{\omega}_o^i \times \mathbf{G} \tag{A.10}$$

3. **Errors in the Measurement of the Unit Vector from the ICS to the OCS:** The vector $\hat{\mathbf{a}} = \mathbf{A}/A$ is measured by the inboard imaging system, and is independent (to first order) of other attitude measurements. Assuming that the error is given by $\delta\Omega_a\ \hat{\omega}_a$, the associated errors will be

$$\delta\mathbf{B} = \delta\Omega_a\, \hat{\omega}_a \times \mathbf{A} \tag{A.11}$$

$$\delta\mathbf{P} = -\delta\Omega_a\, \hat{\omega}_a \times \mathbf{A} \tag{A.12}$$

4. **Errors in the Magnitude of A:** The magnitude of $\mathbf{A}$ will be estimated using a laser ranger (or possibly, merely modeled). The associated errors are given by

$$\delta\mathbf{B} = \delta A\, \hat{\mathbf{a}} \tag{A.13}$$

$$\delta\mathbf{P} = -\delta A\, \hat{\mathbf{a}} \tag{A.14}$$

5. **Errors in the Magnitude of G, $\mathbf{P}_i$, $\mathbf{P}_o$:** These quantities are measured in the ground and are expected to change very little under normal operations. This may change, however, if any of the panels in the antennas fail, shifting the phase centers. The associated errors are given by

$$\begin{aligned} \delta\mathbf{B} &= -\delta P_i\, \hat{\mathbf{p}}_i + \delta P_o\, \hat{\mathbf{p}}_o \qquad (A.15) \\ \delta\mathbf{P} &= -\delta G\, \hat{\mathbf{g}} + \delta P_i\, \hat{\mathbf{p}}_i \qquad (A.16) \end{aligned}$$

6. **Errors in the GPS Location:** These errors only affect the position, and are given by

$$\delta\mathbf{P} = \delta\mathbf{P}_G \qquad (A.17)$$

7. **Errors in the Time Tag:** These errors only affect the along-track component of the position, and are given by

$$\delta\mathbf{P} = \mathbf{V}\ \delta\tau \qquad (A.18)$$

It is often more intuitive or convenient to think of the baseline errors as being composed of errors in the baseline magnitude and direction. To obtain these from $\delta\mathbf{B}$, one uses the chain rule to obtain the intuitive result

$$\begin{aligned} \delta B &= \hat{\mathbf{b}} \cdot \delta\mathbf{B} \qquad (A.19) \\ \delta\hat{\mathbf{b}} &= \left(\mathbf{1} - \hat{\mathbf{b}}\hat{\mathbf{b}}\right) \cdot \frac{\delta\mathbf{B}}{B} \qquad (A.20) \end{aligned}$$

Equation (A.20) can be rewritten as a rotation, $\delta\hat{\mathbf{b}} = \delta\Omega_b\ \hat{\omega}_b \times \hat{\mathbf{b}}$, where the magnitude of the rotation and its direction are given by

$$\begin{aligned} \delta\Omega_b &= \frac{|\delta\mathbf{B}|}{B}\sqrt{1 - \left(\frac{\hat{\mathbf{b}} \cdot \delta\mathbf{B}}{|\delta\mathbf{B}|}\right)} \qquad (A.21) \\ \hat{\omega}_b &= \hat{\mathbf{b}} \times \frac{\delta\mathbf{B}}{|\delta\mathbf{B}|}\frac{1}{\sqrt{1 - \left(\frac{\hat{\mathbf{b}} \cdot \delta\mathbf{B}}{|\delta\mathbf{B}|}\right)}} \qquad (A.22) \end{aligned}$$

This list represents all the errors in the baseline and position vectors due to the measurements of the AODA subsystem. In the following sections, we shall see how they can be translated into geolocation errors.

A.4 Electrical Error Sources

In addition to geometric errors, the interferometric measurement suffers from two additional error sources: phase shifts and time delays. These two quantities are simply related for many configurations. However, there are configurations for which a phase shift measurement is independent of the corresponding time delay, and we will henceforth treat these two error sources independently.

Systematic Phase Shifts: One can associate a phase shift with each interferometric channel. However, since only phase difference measurements are important in interferometry, what really counts is the differential delay between interferometric pairs. In SRTM, there will be four interferometric pairs, corresponsing to each swath, and, consequently, four sources of measurement error, $\delta\Phi_i$ $1 \leq i \leq 4$. These errors are due to errors in estimating the interferometric phase from calibration tones, or due to the fact that a part of the transmit-receive chain is not included in the route of the calibration tone. Typically, one requires that the differential phase biases be known to a few degrees.

Random Phase Shifts: There exist random (uncorrelated from pixel to pixel) phase shifts in the interferometric phase due to thermal noise and speckle decorrelation. A lower (but fairly good) bound for this error is given by the Crámer-Rao bound for the standard deviation

$$\sigma_\Phi = \frac{1}{\sqrt{2N_L}} \frac{\sqrt{1-\gamma^2}}{\gamma} \tag{A.23}$$

where γ is the interferometric correlation between the two signal channels, and N_L is the number of looks.

Time Delays: A time delay will induce a range in the range location of the target, causing a geolocation error. More importantly, differential time delays introduce decorrelation and pahse shifts in the image because the pixels in the two images are misaligned. Typically, one requires that the relative shifts between the two images be less than a few wavelengths, in order to minimize signal loss due to decorrelation. The common time delay for SRTM induces a geolocation error, and must be less than about 1 m in order to meet the error budget. The loss of correlation due to misregistration has been treated elsewhere and will not be studied in detail here, since it depends on the processor range weighting, which has not been determined. As a worst case, the correlation is decreased by a multiplicative factor given by

$$\gamma' = \gamma \left[1 - B\delta T\right] \tag{A.24}$$

where δT is the differential channel delay, and B is the system range bandwidth. The typical requirement in order to obtain acceptable degradations of the correlation is that $B\delta T \leq 10^{-2}$.

A.5 The Interferometric Equations

The SRTM IFSAR system determines the position vector of a pixel given the following measurements (see Figure A.2): 1) $\mathbf{P}$, the position vector in an Earth fixed coordinate system to the phase center of the inboard antenna; 2) R_o and R_i, the distances to a resolution cell (in this memo, we neglect tropospheric delays) from the interferometric outboard and inboard antennas, respectively; 3) Φ, the interferometric phase difference; 4) $\mathbf{B}$, the interferometric baseline; 5) $\mathbf{V}$, the platform velocity; and, 6) k the effective wavenumber of the radiation in the medium. We define $\hat{\mathbf{n}}$ as a unit vector pointing from the reference point to the resolution cell. To define the direction in which the baseline vector points, we will use the convention $\mathbf{B} = \mathbf{R}_o - \mathbf{R}_i$.

These measurements, together with the following auxiliary equations

$$\begin{aligned} \Phi &= k(R_i - R_o) && \text{(A.25)} \\ 2\pi f_D &= 2k\hat{\mathbf{n}} \cdot \mathbf{V} && \text{(A.26)} \\ \hat{\mathbf{n}} \cdot \hat{\mathbf{n}} &= 1 && \text{(A.27)} \end{aligned}$$

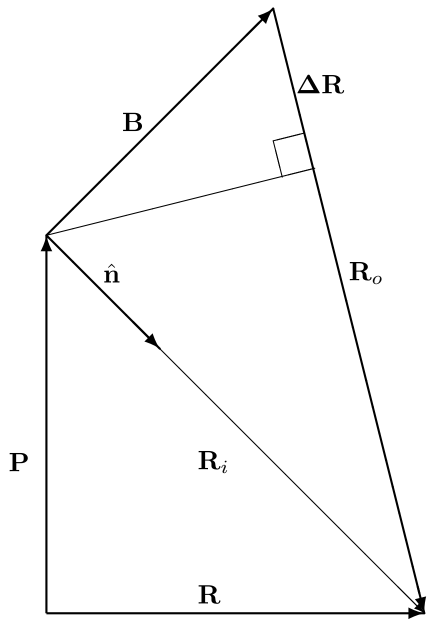

Figure A.2: IFSAR measurement geometry

must be used to determine the line of sight direction to the pixel, $\hat{\mathbf{n}}$. In the previous equations, k is the electromagnetic wavenumber, and f_D is the Doppler frequency. Given $\hat{\mathbf{n}}$ and r, the position vector to the resolution cell, $\mathbf{R}$, can be obtained by means of the equation

$$\mathbf{R} = \mathbf{P} + R_i \hat{\mathbf{n}} \tag{A.28}$$

The equation (A.25) may be solved for $\hat{\mathbf{n}} \cdot \hat{\mathbf{b}}$ to obtain

$$\hat{\mathbf{n}} \cdot \hat{\mathbf{b}} = \frac{-\Phi}{Bk}\left[1 - \frac{1}{2}\frac{B}{R_i}\frac{\Phi}{Bk}\right] - \frac{1}{2}\frac{B}{R_i} \tag{A.29}$$

For a 60 m baseline and a range of 400 km, the phasefront curvature term $B/R_i \sim 1.5 \times 10^{-4}$. From equation (A.28), it is clear that the position error due to errors in the look direction, $\delta\theta$, is of order $r\delta\theta$, and given the range assumed above, it is clear that one can only neglect effects for which $\delta\theta \leq 10^{-7}$. Thus, the phasefront curvature effects may not be neglected when using equation (A.29). However, as we show in Appendix A, these terms can be dropped when considering the contribution the make to the sensitivity analysis. Therefore, for the sake of the sensitivity analysis, we will approximate equation (A.29) by

$$\hat{\mathbf{n}} \cdot \hat{\mathbf{b}} \approx \frac{-\Phi}{Bk} \tag{A.30}$$

It can be shown that the effects of tropospheric propagation do not significantly change the form of these equations. We will use the simplified equations in our subsequent analysis since the use of the exact equations adds unnecessarily to the algebra without contributing to physical understanding, or, in any significant way, to the numerical accuracy of the error analysis.

The interferometric positioning equations can be given a geometric interpretation: equations (A.30) and (A.26) define two cones with axes in the $\hat{\mathbf{b}}$ and $\hat{\mathbf{v}}$ directions, respectively. A point in three dimensional space is defined as the locus of intersection of the two cones and the sphere of radius r. This locus is not uniquely defined: in general, the cones intersect along two straight lines starting at the origin, symmetric about the plane spanned by $\mathbf{B}$ and $\mathbf{V}$. The intersection with the range sphere occurs at two points. Discrimination between these two points is accomplished by specifying which side of the **B-V** plane the point occupies. Mathematically, this is reflected by the fact that equations (A.30) and (A.26) determine two components of $\hat{\mathbf{n}}$: the ones in the plane determined by the baseline and velocity vectors. The third component is specified (up to a sign) by requiring the look direction to be a unit vector.

A.6 Interferometric Error Model

From equation (A.28), $\delta\mathbf{R}$, the error in the interferometric measurement can be written as

$$\delta\mathbf{R} = \delta\mathbf{P} + \hat{\mathbf{n}}\delta R_i + R_i \delta\hat{\mathbf{n}} \tag{A.31}$$

Section A.3 has given a detailed accounting of the position error sources, $\delta\mathbf{P}$. The second type of errors are those that contribute to errors in the range, i.e., contributions to δR_i. These errors can be either due to system timing and delay errors, or to signal delays due to propagation through an inaccurately modeled medium. Typically, system timing errors are very small and will have a negligible contribution to topographic measurements. System delays, on the other hand, are due to a variety of sources (waveguide delays, active elements phase shifts), and must be carefully calibrated to account for their effects. However, once calibrated, these delays are typically stable for a well designed system (although temperature effects must be taken into account) and their contribution to the topographic measurement may be removed by calibration of the system delays and, possibly, by means of ground control points in the scene.

While the first two types of errors are typical of all position measurements by triangulation, the last type, contributions to $\delta\hat{\mathbf{n}}$, are specific to interferometric measurements and we will concentrate on them in this section. From the discussion in the previous section, four measurements are required in order to determine $\hat{n}$: 1) the interferometric phase difference, Φ; 2) the baseline vector, $\mathbf{B}$; 3) the velocity vector, $\mathbf{V}$; and, 4) the effective (in the medium) wavenumber k corresponding to the radar center frequency. The measurement of each of these quantities is potentially in error. In this section we derive an equation connecting the error induced on the position vector by the presence of measurement errors for these parameters.

It is clear that any errors in the baseline or velocity which do not affect equations (A.30) and (A.26) will not introduce positioning errors: i.e., the interferometer is insensitive to errors which are perpendicular to $\hat{\mathbf{n}}$. This implies that if the antenna baseline is orthogonal to the look direction, a dilation of the baseline will not introduce positioning errors (to the accuracy of the previous equations).

Characterization of the last error source can be made by noting, since $\hat{\mathbf{n}}$ is a unit vector, that

$$\delta\hat{\mathbf{n}} \cdot \hat{\mathbf{n}} = 0 \tag{A.32}$$

Hence, errors due to this term must lie in a plane perpendicular to the look direction. The error can be further characterized by specifying the error source: phase error, velocity error, or baseline error. We have assumed that the measurement of interferometric phase and platform velocities are independent. Differentiating equations (A.30) and (A.26) one obtains, respectively

$$\begin{aligned} \frac{\partial\hat{\mathbf{n}}}{\partial\mathbf{V}} \cdot \mathbf{B} &= 0 && \text{(A.33)} \\ \frac{\partial\hat{\mathbf{n}}}{\partial\mathbf{B}} \cdot \mathbf{V} &= 0 && \text{(A.34)} \end{aligned}$$

Together with equation (A.32), the first equation implies that an error due to velocity errors must be simultaneously perpendicular to the look and the baseline directions. This condition is only satisfied if the position error lies along the axis defined by the vector $\hat{\mathbf{n}} \times \mathbf{B}$. Similarly, an error in the baseline will induce a position error which lies on the axis defined by the vector $\hat{\mathbf{n}} \times \mathbf{V}$.

Using this reasoning, it is simple to obtain simple geometric expressions for the error in the look direction for the cases mentioned above. We illustrate the procedure assuming that there is no velocity error, and obtain the dual equation by analogy. We define an orthonormal triad by choosing $\hat{\mathbf{v}}$, $\hat{\beta} \equiv (\mathbf{1} - \hat{\mathbf{v}}\hat{\mathbf{v}}) \cdot \hat{\mathbf{b}} / |(\mathbf{1} - \hat{\mathbf{v}}\hat{\mathbf{v}}) \cdot \hat{\mathbf{b}}|$, and $\hat{\gamma} \equiv \hat{\mathbf{v}} \times \hat{\beta}$, use $\delta\hat{\mathbf{n}} \cdot \hat{\mathbf{v}} = -\hat{\mathbf{n}} \cdot \delta\hat{\mathbf{v}} = 0$ (from our assumption), and $\delta\hat{\mathbf{n}} \cdot \hat{\mathbf{n}} = 0$, to obtain the equation

$$\delta\hat{\mathbf{n}} = \delta\hat{\mathbf{n}} \cdot \hat{\beta} \frac{\hat{\mathbf{n}} \times \hat{\mathbf{v}}}{\hat{\mathbf{n}} \cdot \hat{\gamma}}$$

which, after some massaging, gives us our final results

$$\delta\hat{\mathbf{n}} = -\frac{\delta\left(\Phi/kB\right) + \hat{\mathbf{n}} \cdot \delta\hat{\mathbf{b}}}{|(\mathbf{1} - \hat{\mathbf{v}}\hat{\mathbf{v}}) \cdot \hat{\mathbf{b}}|} \frac{\hat{\mathbf{n}} \times \hat{\mathbf{v}}}{\hat{\mathbf{b}} \cdot (\hat{\mathbf{n}} \times \hat{\mathbf{v}})} \tag{A.35}$$

where we have use $\delta\hat{\mathbf{n}} \cdot \hat{\mathbf{b}} = -\delta\left(\Phi/kB\right) - \hat{\mathbf{n}} \cdot \delta\hat{\mathbf{b}}$, which follows from equation (A.30). This equation is suitable for characterizing errors due to baseline magnitude, orientation, and phase, since these errors are independent of velocity. As expected, the error vector lies along the vector $\hat{\mathbf{n}} \times \hat{\mathbf{v}}$. This implies that no along-track errors are produced by these error source. In terms of the **sch**-coordinate system, all errors are in the **c-h** plane.

An analogous derivation for the case where there are only velocity dependent errors obtains

$$\delta\hat{\mathbf{n}} = -\frac{\hat{\mathbf{n}} \cdot \delta\hat{\mathbf{v}}}{\left|\left(\mathbf{1} - \hat{\mathbf{b}}\hat{\mathbf{b}}\right) \cdot \hat{\mathbf{v}}\right|} \frac{\hat{\mathbf{n}} \times \hat{\mathbf{b}}}{\hat{\mathbf{v}} \cdot \left(\hat{\mathbf{n}} \times \hat{\mathbf{b}}\right)} \tag{A.36}$$

where we used the fact that the Doppler frequency is held constant during processing, together with $\delta\hat{\mathbf{n}} \cdot \hat{\mathbf{v}} + \hat{\mathbf{n}} \cdot \delta\hat{\mathbf{v}} = 0$, which follows from applying the chain rule to equation (A.26). As expected, these errors are perpendicular to the baseline and look directions, so that they lie nearly in the along-track direction, for the SRTM geometry.

In general, the geometric characteristics of errors in $\hat{\mathbf{n}}$ due to errors in the wavenumber, k, or, equivalently, in the speed of light or wavelength, are not as apparent from the previous equations as those for velocity and baseline errors since k is present in both equations (A.26) and (A.30). From the condition $\hat{\mathbf{n}} \cdot \delta\hat{\mathbf{n}} = 0$, one obtains

$$\delta\hat{\mathbf{n}} = \frac{1}{\hat{\mathbf{b}} \cdot \left(\hat{\mathbf{n}} \times \hat{\mathbf{v}}\right)} \left[\left(\hat{\mathbf{n}} \times \hat{\mathbf{v}}\right) \delta\hat{\mathbf{n}} \cdot \hat{\beta} - \left(\hat{\mathbf{n}} \times \hat{\beta}\right) \delta\hat{\mathbf{n}} \cdot \hat{\mathbf{v}}\right] \tag{A.37}$$

Differentiating (A.26) and (A.30), one obtains the pair of equations

$$\begin{aligned} \delta\hat{\mathbf{n}} \cdot \hat{\mathbf{v}} &= -\hat{\mathbf{n}} \cdot \hat{\mathbf{v}} \frac{\delta k}{k} && \text{(A.38)} \\ \delta\hat{\mathbf{n}} \cdot \hat{\beta} &= -\frac{1}{\hat{\beta} \cdot \hat{\mathbf{b}}} \left[\hat{\mathbf{n}} \cdot \hat{\mathbf{b}} - \left(\hat{\mathbf{b}} \cdot \hat{\mathbf{v}}\right)\right] \frac{\delta k}{k} && \text{(A.39)} \end{aligned}$$

Replacing (A.38) and (A.39) intp (A.37), and using the definition of $\hat{\beta}$, one obtains the final answer for the wavenumber induced error

$$\delta\hat{\mathbf{n}} = \frac{1}{\hat{\mathbf{b}} \cdot \left(\hat{\mathbf{n}} \times \hat{\mathbf{v}}\right)} \frac{1}{\left|\left(\mathbf{1} - \hat{\mathbf{v}}\hat{\mathbf{v}}\right) \cdot \hat{\mathbf{b}}\right|} \left[\left(\hat{\mathbf{n}} \cdot \hat{\mathbf{b}}\right) \hat{\mathbf{n}} \times \hat{\mathbf{v}} - \left(\hat{\mathbf{n}} \cdot \hat{\mathbf{v}}\right) \hat{\mathbf{n}} \times \hat{\mathbf{b}}\right] \frac{\delta k}{k} \tag{A.40}$$

A.7 Application to SRTM Errors

In principle, equations (A.31), (A.35), and (A.36), together with the equations in Section A.3 provide a complete description of all SRTM errors. In this section, we examine a few of the more important terms in greater detail.

1. **Errors due to Uncertainty in the ICS Attitude Relative to WGS:** From equations (A.7), (A.35), and (A.28) it follows that the error in position due to errors in the look direction will be

$$\delta\mathbf{R} = -R_i \delta\Omega_i^w \frac{\hat{\mathbf{n}} \cdot \left(\hat{\omega}_i^w \times \hat{\mathbf{b}}\right)}{\left|\left(\mathbf{1} - \hat{\mathbf{v}}\hat{\mathbf{v}}\right) \cdot \hat{\mathbf{b}}\right|} \frac{\hat{\mathbf{n}} \times \hat{\mathbf{v}}}{\hat{\mathbf{b}} \cdot \left(\hat{\mathbf{n}} \times \hat{\mathbf{v}}\right)} \tag{A.41}$$

Notice that in this case, there is an additional position error, also, as given in equation (A.8): it is typically much smaller than the error due to the baseline rotation.

We examine three axes of rotation separately:

(a) **Roll Errors:** The roll axis is defined by the velocity vector: $\hat{\omega}_i^w = \hat{\mathbf{v}}$. Replacing into equation (A.41), we obtain

$$\delta \mathbf{R} = -R_i \delta\Omega_i^w \, \frac{\hat{\mathbf{n}} \times \hat{\mathbf{v}}}{|(\mathbf{1} - \hat{\mathbf{v}}\hat{\mathbf{v}}) \cdot \hat{\mathbf{b}}|} \tag{A.42}$$

Since both $\hat{\mathbf{n}}$ and $\hat{\mathbf{b}}$ are nearly perpendicular to the velocity vector, we see that the effect of a roll error is to tilt the entire scene about the reference phase center. This is one of the dominating SRTM errors.

(b) **Yaw Errors:** We define the yaw axis as being perpendicular to bot the velocity and baseline directions: $\hat{\omega}_i^w = \hat{\mathbf{v}} \times \hat{\mathbf{b}} / |\hat{\mathbf{v}} \times \hat{\mathbf{b}}|$. Replacing into equation (A.41), we obtain

$$\delta \mathbf{R} = -R_i \delta\Omega_i^w \, \frac{\hat{\mathbf{n}} \cdot (\mathbf{1} - \hat{\mathbf{b}}\hat{\mathbf{b}}) \cdot \hat{\mathbf{v}}}{|(\mathbf{1} - \hat{\mathbf{v}}\hat{\mathbf{v}}) \cdot \hat{\mathbf{b}}|^2} \frac{\hat{\mathbf{n}} \times \hat{\mathbf{v}}}{\hat{\mathbf{b}} \cdot (\hat{\mathbf{n}} \times \hat{\mathbf{v}})} \tag{A.43}$$

We notice that the magnitude of this expression is dependent on $\hat{\mathbf{n}} \cdot \hat{\mathbf{v}}$ and $\hat{\mathbf{v}} \cdot \hat{\mathbf{b}}$. In Appendix B, we show that, if the data is processed to $f_D = 0$, $\hat{\mathbf{n}} \cdot \hat{\mathbf{v}} \leq 4.4 \times 10^{-2}$, and $\hat{\mathbf{v}} \cdot \hat{\mathbf{b}} \ll \hat{\mathbf{n}} \cdot \hat{\mathbf{v}}$ in general. This implies that the errors associated with pitch are more than an order of magnitude smaller than thos associated with roll.

(c) **Pitch Errors:** Defining the pitch axis as being orthogonal to roll and yaw (they form the orthonormal triad roll-pitch-yaw), we obtain

$$\delta \mathbf{R} = -R_i \delta\Omega_i^w \; \hat{\mathbf{v}} \cdot \hat{\mathbf{b}} \frac{\hat{\mathbf{n}} \times \hat{\mathbf{v}}}{|(\mathbf{1} - \hat{\mathbf{v}}\hat{\mathbf{v}}) \cdot \hat{\mathbf{b}}|^2} \tag{A.44}$$

which, since it depends on $\hat{\mathbf{v}} \cdot \hat{\mathbf{b}}$, we conclude to be even smaller than the yaw error.

2. **Errors Due to Baseline Dilations Only:** From equation (A.35), we obtain the expression for the position error

$$\delta \mathbf{R} = R_i \frac{\delta B}{B} \frac{\hat{\mathbf{n}} \cdot \hat{\mathbf{b}}}{|(\mathbf{1} - \hat{\mathbf{v}}\hat{\mathbf{v}}) \cdot \hat{\mathbf{b}}|} \frac{\hat{\mathbf{n}} \times \hat{\mathbf{v}}}{\hat{\mathbf{b}} \cdot (\hat{\mathbf{n}} \times \hat{\mathbf{v}})} \tag{A.45}$$

Notice that this equation predicts (to first order in $\delta B/B$), that there will be no error when $\hat{\mathbf{n}} \cdot \hat{\mathbf{b}}$, which lies at the center of the swath, for SRTM. The error grows like $R_i \sin\phi \delta B/B$, where ϕ is the angle away from the nominal antenna boresight.

3. **Phase Errors:** From equation (A.35), we obtain the expression for the position error

$$\delta \mathbf{R} = R_i \frac{\delta \Phi}{kB} \frac{1}{|(\mathbf{1} - \hat{\mathbf{v}}\hat{\mathbf{v}}) \cdot \hat{\mathbf{b}}|} \frac{\hat{\mathbf{n}} \times \hat{\mathbf{v}}}{\hat{\mathbf{b}} \cdot (\hat{\mathbf{n}} \times \hat{\mathbf{v}})} \tag{A.46}$$

Since the velocity, baseline, and look direction are close to being perpendicular, the main variation in the magnitude of the location error due to phase is due to the increase in R_i with angle.

4. **Errors in the Measurement of the Unit Vector from the ICS to the OCS:** Since **A** is not parallel to **B**, the total position error due to the look direction (other position errors are much smaller) involves both a dilation and a rotation. The magnitude of the dilation is given by (see equation (A.19)

$$\frac{\delta B}{B} = \frac{A}{B} \delta\Omega_a \, \hat{\mathbf{b}} \cdot (\hat{\omega}_a \times \mathbf{a}) \tag{A.47}$$

The change in $\hat{\mathbf{b}}$ will be given by

$$\delta\hat{\mathbf{b}} = \delta\Omega_a \, \frac{A}{B} \, (\mathbf{1} - \hat{\mathbf{b}}\hat{\mathbf{b}}) \cdot (\hat{\omega}_a \times \mathbf{a}) \tag{A.48}$$

These equations can now be replaced in the equations derived above for dilation and rotation errors. Notice that due to the large lever arm, an error in this attitude measurement does not necessarily induce a small dilation error. A similar discussion also holds for the errors in the OCS attitude relative to the ICS, but in this case the lever arm, P_o is much smaller.

A.8 From Vectors to Height Errors

In the previous sections, we derived the total position error. Often, we are more concerned in determining the error in height relative to the local tangent plane. In this section, we derive the height errors and also introduce a coordinate system which has become conventional when dealing with interferometric geometry.

The convention at JPL has been to use the **s** (along-track) **c** (cross-track) **h** (height) coordinate system when reporting heights. This system is defined by projecting onto a sphere, whose radius is determined by the WGS84 ellipsoid radius of curvature at a **peg point**, whose equator is determined by the IFSAR displacement. In this coordinate system, **s** measures distance along the equator (i.e., longitude from the peg point times the radius of curvature), **c** measures distance from the equator (i.e., latitude measured from the equator times the radius of curvature), and **h** measures the displacement normal to the reference sphere. This system is mathematically simple, although it suffers from convergenge of the meridians: iso-s lines are only approximately parallel.

If we place our coordinate system at the center of the approximating sphere, we will have that a unit vector in the radial direction is given by (see Figure A.3)

$$\hat{\mathbf{h}} = \frac{\mathbf{R}}{|\mathbf{R}|} = \frac{\hat{\mathbf{h}_P} + (R_i/P)\,\hat{\mathbf{n}}}{\sqrt{1 + 2\,(R_i/P)\,\hat{\mathbf{h}}_P \cdot \hat{\mathbf{n}} + (R_i/P)^2}} \tag{A.49}$$

where we have used equation (A.28), and introduce $\mathbf{h}_P$, the height unit vector at the platform, which points radially away from the center of the sphere.

Since $\delta\hat{\mathbf{n}} \cdot \hat{\mathbf{n}} = 0$, for all error sources affecting the look direction, one will have that

$$\delta\hat{\mathbf{n}} \cdot \hat{\mathbf{h}} = \frac{\hat{\mathbf{h}}_P \cdot \delta\hat{\mathbf{n}}}{\sqrt{1 + 2(R_i/P)\hat{\mathbf{h}}_P \cdot \hat{\mathbf{n}} + (R_i/P)^2}} \tag{A.50}$$

One can now proceed to obtain expression for the height error by replacing $\delta\hat{\mathbf{n}}$ by the appropriate expression from the previous sections. We illustrate the results for the velocity independent look

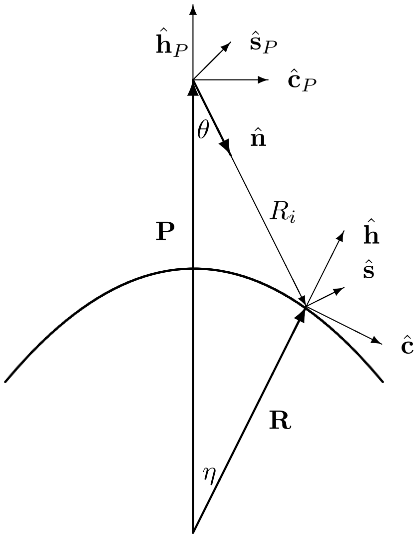

Figure A.3: Local Coordinate Systems

errors. Replacing (A.35) into (A.50), one obtains

$$\delta h = -R_i \frac{\delta\left(\Phi/kB\right) + \hat{\mathbf{n}} \cdot \delta\hat{\mathbf{b}}}{|(\mathbf{1} - \hat{\mathbf{v}}\hat{\mathbf{v}}) \cdot \hat{\mathbf{b}}|} \frac{1}{\hat{\mathbf{b}} \cdot (\hat{\mathbf{n}} \times \hat{\mathbf{v}})} \frac{\hat{\mathbf{h}}_P \cdot (\hat{\mathbf{n}} \times \hat{\mathbf{v}})}{\sqrt{1 + 2\left(R_i/P\right)\hat{\mathbf{h}}_P \cdot \hat{\mathbf{n}} + \left(R_i/P\right)^2}} \tag{A.51}$$

Introducing the local **sch** coordinate system defined at the platform by $\hat{\mathbf{h}}_P$, $\hat{\mathbf{s}}_P = (\mathbf{1} - \hat{\mathbf{h}}_P\hat{\mathbf{h}}_P) \cdot \hat{\mathbf{v}}/|(\mathbf{1} - \hat{\mathbf{h}}_P\hat{\mathbf{h}}_P) \cdot \hat{\mathbf{v}}|$ and $\hat{\mathbf{c}}_P = \hat{\mathbf{s}}_P \times \hat{\mathbf{h}}_P$, and introducing the look angle θ defined by $\sin\theta = \hat{\mathbf{n}} \cdot \hat{\mathbf{c}}_P$, the previous expression can be written as

$$\delta h = -R_i(\theta) \frac{\delta\left(\Phi/kB\right) + \hat{\mathbf{n}} \cdot \delta\hat{\mathbf{b}}}{|(\mathbf{1} - \hat{\mathbf{v}}\hat{\mathbf{v}}) \cdot \hat{\mathbf{b}}|} \frac{1}{\hat{\mathbf{b}} \cdot (\hat{\mathbf{n}} \times \hat{\mathbf{v}})} \frac{\cos\nu\sin\theta}{\sqrt{1 - 2\left(R_i(\theta)/P\right)\cos\theta + \left(R_i(\theta)/P\right)^2}} \tag{A.52}$$

where we have introduced ν, the angle between $\hat{\mathbf{s}}_P$ and $\hat{\mathbf{v}}$.

From Figure A.3, one has that $R_i^2 = R^2 + P^2 - 2RP\cos\eta$, where η is the sphere's interior angle. Using the law of sines, $\sin\eta = (R_i/R)\sin\theta$ and one can approximate $\cos\eta \approx 1 - 1/2(R_i/R)^2\sin^2\theta$cv , where we have neglected terms of order $\mathcal{O}(R_i/R)^4$, to obtain

$$R_i(\theta) = \frac{H}{\cos\theta} \frac{1}{\sqrt{1 - (H/R)\tan^2\theta}} \tag{A.53}$$

We have reduced almost all terms in equation (A.35) to terms which depend on the look angle alone. One could continue to reduce this equation to angle variables only by writing the baseline, look, and velocity directions in terms of angles measured in the platform **sch** coordinate system. A full decomposition of the errors in this coordinate system is presented in Appendix D. Here, for illustrative purposes, we deal with the case when $\hat{\mathbf{b}}$ and $\hat{\mathbf{n}}$ are in a plane perpendicular to $\hat{\mathbf{v}}$. We introduce α, the angle between the baseline vector and the $\hat{\mathbf{c}}_P$ direction, and after a bit of manipulation show that $|(\mathbf{1} - \hat{\mathbf{v}}\hat{\mathbf{v}}) \cdot \hat{\mathbf{b}}| = 1$ and

$$\hat{\mathbf{b}} \cdot (\hat{\mathbf{n}} \times \hat{\mathbf{v}}) = \cos(\theta - \alpha) \tag{A.54}$$

Putting all the components together, equation (A.35) becomes

$$\delta h = -R_i(\theta) \frac{\delta(\Phi/kB) + \hat{\mathbf{n}} \cdot \delta\hat{\mathbf{b}}}{\cos(\theta - \alpha)} \frac{\cos\nu \sin\theta}{\sqrt{1 - 2(R_i(\theta)/P)\cos\theta + (R_i(\theta)/P)^2}} \tag{A.55}$$

In this section, we showed how to obtain the height errors from the total position error. The geolocation errors can be obtained by subtracting the height error from the total error. These errors will have components along both the **c** and **s** directions. However, in order to determine how much the error is in each of these directions, we must take into account the fact that we are now working in a curved coordinate system and the unit vectors depend on the position of the point on the reference sphere. We treat this subject in the next section.

A.9 Geolocation Errors

Neglecting Phasefront Curvature Terms

Taking the variation of equation (A.29), we obtain

$$\delta(\hat{\mathbf{n}} \cdot \hat{\mathbf{b}}) = -\delta\left(\frac{\Phi}{kB}\right)\left[1 - \frac{1}{2}\frac{B}{R_i}\left(\frac{\Phi}{kB}\right)\right] - \frac{1}{2}\delta\left(\frac{B}{R_i}\right)\left(1 - \frac{\Phi}{kB}\right) \tag{A.56}$$

To first order, we have that $\delta\theta \sim \delta\left(\frac{\Phi}{kB}\right) \sim 11\text{arcsec} \sim 5 \times 10^{-5}$. Assuming $B = 60$ m and $R_i = 400$ km, then $B/R_i \sim 1.5 \times 10^{-4}$. Finally, using $\Phi/kB \sim \sin\theta$, we have that the contribution of the second term in the first square bracket is of order

$$\delta\left(\frac{\Phi}{kB}\right)\frac{B}{R_i} \leq 10^{-8} \tag{A.57}$$

and can therefore be neglected.

on the other hand,

$$\delta\left(\frac{B}{R_i}\right) = \frac{\delta B}{R_i} - \frac{B}{R_i}\frac{\delta R_i}{R_i} \tag{A.58}$$

Assuming $\delta B \leq 10^{-2}$ m and $\delta R_i \leq 1$ m, we see that the contribution of equation (A.58) to $\delta\theta \leq 10^{-7}$, and can again be neglected.

Zero Doppler Geometry

If $f_D = 0$, one must have that

$$\hat{\mathbf{n}} \cdot (\mathbf{V} - \mathbf{V}_E) = 0 \tag{A.59}$$

where $\mathbf{V}_E$ is the Earth's velocity at the point being imaged. Introduce the orthonormal triad $\hat{\mathbf{r}}$, $\hat{\mathbf{v}}$, and $\hat{\mathbf{p}} \equiv \hat{\mathbf{r}} \times \hat{\mathbf{v}}$, where $\hat{\mathbf{r}}$ is the unit vector which points from the center of the Earth to the platform. For a fixed look angle θ_0, one has that

$$\hat{\mathbf{r}} \cdot \hat{\mathbf{n}} = \cos\theta_0 \tag{A.60}$$

We now assume that the platform height is small enough so that one can assume that $\hat{\mathbf{r}} \cdot \mathbf{V}_E = 0$; i.e., the radial direction at the platform and the observation point are approximately the same. Using this, together with equation (A.59), results in the equation

$$(1 - \epsilon \sin\alpha)\, \hat{\mathbf{n}} \cdot \hat{\mathbf{v}} = \epsilon \hat{\mathbf{n}} \cdot \mathbf{p} \cos\alpha \tag{A.61}$$

where we have defined $\epsilon = V_E/V$ and the orbit inclination angle α is defined by $\hat{\mathbf{v}}_E \cdot \hat{\mathbf{v}} = \sin\alpha$. Using $\hat{\mathbf{n}} \cdot \hat{\mathbf{n}} = 1$, together with equations (A.60) and (A.61), we obtain

$$\hat{\mathbf{n}} \cdot \hat{\mathbf{v}} = \frac{\epsilon \cos\alpha \sin\theta_0}{\sqrt{1 - 2\epsilon \sin\alpha + \epsilon^2}} \tag{A.62}$$

which obeys $\hat{\mathbf{n}} \cdot \hat{\mathbf{v}} \to 0$ as $\epsilon \to 0$ (stationary earth), and $\hat{\mathbf{n}} \cdot \hat{\mathbf{v}} \to 0$ as $\alpha \to \pi/2$ (equatorial orbit), as expected.

At the equator, the magnitude of the Earth's tangential velocity is approximately $V_E \sim 4.6 \times 10^{-1}$ km/sec. Assuming that the platfor velocity is $V = 7$ km/sec and taking $\alpha = 24°$ and $theta_0 = 45°$, one obtains $\hat{\mathbf{n}} \cdot \hat{\mathbf{v}} \sim 4.4 \times 10^{-2}$, corresponding to a steering angle of about 2.5°.

Assuming that for the zero-Doppler geometry, $\hat{\mathbf{b}}$ lies in the $\hat{\mathbf{r}}$–$\hat{\mathbf{n}}$ plane, one obtains

$$\hat{\mathbf{v}} \cdot \hat{\mathbf{b}} = \frac{\hat{\mathbf{v}} \cdot \hat{\mathbf{n}} \hat{\mathbf{b}} \cdot \hat{\mathbf{n}}}{\sin\theta_0} \tag{A.63}$$

which vanishes for $\hat{\mathbf{b}} \cdot \hat{\mathbf{n}} = 0$. i.e., at the center of the swath.

Some Vector/Rotation Fun(damentals)

What is a Dyad and Why Should I Care?

In the same way that a function is a machine which given a number (or a series of numbers) will spit out a number, a dyad is a machine which will spit out a vector when given a vector input. A dyad is represented by a pair of vectors standing next to each other (or a sum of such pairs), and it operates on vectors, either on the right or the left, by taking a dot product, as follows ($\hat{\mathbf{a}}\hat{\mathbf{b}}$ is the dyad, and $\mathbf{C}$ is an arbitrary vector)

$$\left(\hat{\mathbf{a}}\hat{\mathbf{b}}\right) \cdot \mathbf{C} = \hat{\mathbf{a}} \left(\hat{\mathbf{b}} \cdot \mathbf{C}\right) \tag{A.64}$$

$$\mathbf{C} \cdot \left(\hat{\mathbf{a}}\hat{\mathbf{b}}\right) = (\mathbf{C} \cdot \hat{\mathbf{a}})\, \hat{\mathbf{b}} \tag{A.65}$$

Many people are used to thinking that matrices are the natural way of representing operators which take vectors into vectors. However, thinking in terms of matrices has the disadvantage that the matrix will change if the coordinate system changes, obscuring the geometrical meaning of the operation.

A dyadic pair (which is a special case of second rank tensors) has a clear geometric meaning, independent of coordinate systems: it finds the projection of the operand on one of the dyad vectors, and multiplies the remaining vector by the result. A specially useful dyad which appears repeatedly in the text is the projector dyad, which takes the form $(\mathbf{1} - \hat{\mathbf{x}}\hat{\mathbf{x}})$, where $\hat{x}$ is a unit vector. When acting on an arbitrary vector $\mathbf{y}$, a projector will return the component of $\mathbf{y}$ which lies in the plane perpendicular to $\hat{\mathbf{x}}$ (see Figure A.4). To see this, notice that

$$\begin{aligned} \hat{\mathbf{x}} \cdot ((\mathbf{1} - \hat{\mathbf{x}}\hat{\mathbf{x}}) \cdot \mathbf{y}) &= \hat{\mathbf{x}} \cdot [\mathbf{y} - (\hat{\mathbf{x}} \cdot \mathbf{y})\,\hat{\mathbf{x}}] && \text{(A.66)} \\ &= \hat{\mathbf{x}} \cdot \mathbf{y} - \hat{\mathbf{x}} \cdot \mathbf{y} = 0 && \text{(A.67)} \end{aligned}$$

This can also be seen from the fact that the projection operator can be written as

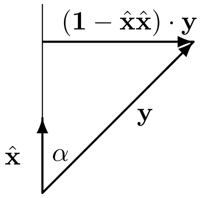

Figure A.4: Action of the Projection Operator

$$(\mathbf{1} - \hat{\mathbf{x}}\hat{\mathbf{x}}) \cdot \mathbf{y} = \hat{\mathbf{x}} \times (\mathbf{y} \times \hat{\mathbf{x}}) \tag{A.68}$$

It can easily be checked that a projector has the same effect whether acting to the right or the left, and applying a projector twice is the same as applying once: once you have projected out the orthogonal component, the projector acts as an identity.

Another expression which makes a frequent appearance has the generic form $|\,(\mathbf{1} - \hat{\mathbf{x}}\hat{\mathbf{x}}) \cdot \mathbf{y}| = |\mathbf{y}|\sqrt{1 - (\mathbf{y} \cdot \hat{\mathbf{x}})^2} = |\mathbf{y}| \sin\alpha$ where α is the angle between $\mathbf{y}$ and $\hat{\mathbf{x}}$, as shown in Figure A.4

Rotations as Cross Products

Suppose that we want to rotate a vector $\mathbf{A}$ an infinitesimal amount, $\delta\Omega$ about the axis defined by the unit vector $\hat{\mathbf{z}}$ (see Figure A.5). If we pick the coordinate system such that $\hat{\mathbf{z}}$ defines the third axis, the effect of the rotation on the components of $\mathbf{A}$ can be written as

$$\begin{aligned} \begin{pmatrix} A'_x \\ A'_y \\ A'_z \end{pmatrix} &= \begin{pmatrix} \cos\delta\Omega & \sin\delta\Omega & 0 \\ -\sin\delta\Omega & \cos\delta\Omega & 0 \\ 0 & 0 & 1 \end{pmatrix} \begin{pmatrix} A_x \\ A_y \\ A_z \end{pmatrix} && \text{(A.69)} \\ &\approx \begin{pmatrix} 1 & \delta\Omega & 0 \\ -\delta\Omega & 1 & 0 \\ 0 & 0 & 1 \end{pmatrix} \begin{pmatrix} A_x \\ A_y \\ A_z \end{pmatrix} && \text{(A.70)} \end{aligned}$$

which can be written more conveniently in the geometric notation

$$\delta\mathbf{A} = \mathbf{A}' - \mathbf{A} = \delta\Omega\,\hat{\mathbf{z}} \times \mathbf{A} \tag{A.71}$$

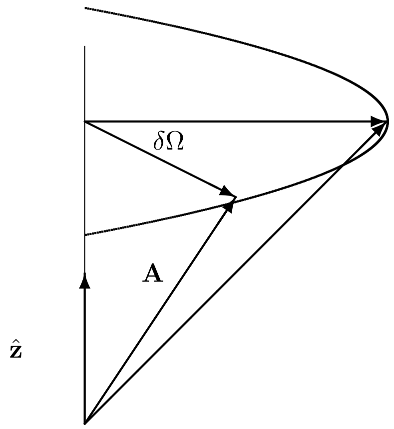

Figure A.5: Rotation about the axis $\hat{\mathbf{z}}$

which is an equation which has been made use of repeatedly in the text.

If we are interested in a finite rotation Ω about $\hat{\mathbf{z}}$, we should think of dividing Ω into N component rotations of magnitude Ω/N, and letting $N \rightarrow \infty$. Using our previous result for infinitesimal rotations, we obtain

$$\mathbf{A}' = \lim N \rightarrow \infty \left(1 + \frac{\Omega}{N}\,\hat{\mathbf{z}}\times\right)^N \mathbf{A} \tag{A.72}$$

Now we use the well known result

$$\lim N \rightarrow \infty \left(1 + \frac{x}{N}\right)^N = e^x \tag{A.73}$$

to write

$$\begin{aligned} \mathbf{A}' &= \exp\left[\Omega\,\hat{\mathbf{z}}\times\right]\mathbf{A} && \text{(A.74)} \\ &\equiv \mathbf{A} + \Omega\,\hat{\mathbf{z}} \times \mathbf{A} + \frac{1}{2}\Omega\,\hat{\mathbf{z}} \times (\Omega\,\hat{\mathbf{z}} \times \mathbf{A}) + \ldots && \text{(A.75)} \end{aligned}$$

where the exponential of an operator is understood as an infinite series, as presented in equation (A.1). This method for presenting rotations allows one to describe the rotation by its geometrical characteristics (axis and magnitude), rather than by its specific representation in any coordinate system. (Note for those with some mathematical curiosity: the description of rotations in terms of anticommuting cross-products is intrinsically tied to the frequent use of quaternion algebra to represents rotations, as is commonly done throughout JPL. It is also intrinsically related to the infinitesimal generators of the rotation group, $\mathbf{O}(3)$.)